Producing highly complicated materials. Nature does it better

Luca Bindi, Massimo Nespolo, Sergey Krivovichev, Gervais Chapuis, Cristian Biagioni

▶ **To cite this version:**

Luca Bindi, Massimo Nespolo, Sergey Krivovichev, Gervais Chapuis, Cristian Biagioni. Producing highly complicated materials. Nature does it better. Reports on Progress in Physics, 2020, 83 (10), pp.106501. ⟨10.1088/1361-6633/abaa3a⟩. ⟨hal-02933187⟩

HAL Id: hal-02933187

https://hal.univ-lorraine.fr/hal-02933187v1

Submitted on 8 Sep 2020

HAL is a multi-disciplinary open access archive for the deposit and dissemination of scientific research documents, whether they are published or not. The documents may come from teaching and research institutions in France or abroad, or from public or private research centers.

L'archive ouverte pluridisciplinaire **HAL**, est destinée au dépôt et à la diffusion de documents scientifiques de niveau recherche, publiés ou non, émanant des établissements d'enseignement et de recherche français ou étrangers, des laboratoires publics ou privés.

HAL Authorization

Producing highly complicated materials. Nature does it better

Luca Bindi[1,*], Massimo Nespolo[2], Sergey V. Krivovichev[3,4], Gervais Chapuis[5], Cristian Biagioni[6]

[1] Dipartimento di Scienze della Terra, Università degli Studi di Firenze, via La Pira 4, I-50121 Firenze, Italy

[2]Université de Lorraine, CNRS, CRM2, Nancy, France

[3] Department of Crystallography, St. Petersburg State University, University Emb. 7/9, St. Petersburg, 199034, Russian Federation

[4]Nanomaterials Research Center, Kola Science Center, Russian Academy of Sciences, Fersmana str. 14, Apatity, Murmansk region, 184209, Russian Federation

[5] Institut de Physique, École Polytechnique Fédérale de Lausanne, CH-1015 Lausanne, Switzerland

[6] Dipartimento di Scienze della Terra, Università di Pisa, Via Santa Maria 53, I-56126 Pisa, Italy

*Email: luca.bindi@unifi.it

Abstract

Through the years, mineralogical studies have produced a tremendous amount of data on the atomic arrangement and mineral properties. Quite often, structural analysis has led to elucidate the role played by minor components, giving interesting insights into the physico-chemical conditions of minerals and allowing the description of unpredictable structures that represented a body of knowledge critical for assessing their technological potentialities. Using such a rich database, containing many basic acquisitions, further steps became appropriate and possible, into the directions of more advanced knowledge frontiers. Some of these frontiers assume the name of modularity, complexity, aperiodicity, and matter organization at not conventional levels, and will be discussed in this review.

Contents

1. Nature: A treasure-trove for structural complexity
2. Modularity of crystal structures
2.1 Introduction
2.2 Symbolic representation of modular structures
2.3 Modular structures whose archetype are phyllosilicates
2.3.1 Layer modular structures
2.3.2 Modular structures with empty interlayer region
2.3.3 Modular structures with cations in the interlayer region
2.3.4 Modular structures with an O sheet in the interlayer region
2.3.5 Rod modular structures
2.4 Polyarchetypal modular structures. The example of pyroxenoids
3. Information-based analysis of structural complexity of minerals
3.1 Introduction
3.2 Structural complexity measures
3.3 Applications: general overview
3.4 Most complex mineral structures
3.5 Information-density analysis
3.6 Chemical complexity
4. Structural complexity, disorder phenomena and the rise of ionic properties
4.1 Introduction
4.2 NASICON
4.3 $NaSbO_3$, brizziite
4.4 Ag- and Cu-bearing sulfosalts
4.4.1 Pearceite, polybasite and fettelite
4.4.2 Argyrodite-canfieldite series
5. Structural complexity in sulfosalts and the role of minor constituents
5.1 Introduction
5.2 Boxwork structures
5.3 Other zinkenite-related complex sulfosalts
5.4 Information-based complexity in sulfosalts
5.5 Role of minor constituents
6. Aperiodic minerals
6.1 Introduction
6.2 Short theoretical presentation
6.3 Natrite, Na_2CO_3
6.4 Calaverite $Au_{1-x}Ag_xTe_2$
6.5 Melilite $(Ca,Na)_2(Mg,Fe^{2+},Al)[(Al,Si)SiO_7]$
6.6 Natural Quasicrystals
6.7 The puzzle of “labradorite”
6.8 When “disorder” turns out in aperiodicity
7. Conclusions and perspectives
Acknowledgements
References

1. Nature: A treasure-trove for structural complexity

The study of the materials formed by Nature, i.e. the minerals, has been always the basis for the greatest breakthroughs in chemistry and solid state physics, including the discovery of new elements and chemical compounds, the construction of the periodic table of the elements and the deciphering of the properties of polarized light (Lima-de-Faria 1990). The observations of the mineral morphologies (crystal faces) led to elaborate theories of the structure of solid matter, which were experimentally confirmed in the first decades of the 20th century with the studies on the interaction between X-rays and crystals. The increasingly detailed definition of the physical properties (hardness, tenacity, luminescence, radioactivity, magnetism, electrical and optical properties, etc.) and the compositional and structural characteristics of minerals, as well as the search for natural or synthetic materials with specific mechanical, electrical, magnetic and thermal properties, led to the birth of "materials science" in the middle of the 20th century. The development of materials science was considered as a true technological revolution, a response to precise demands related to economy and industry, and which today is increasingly being used to give answers related to human health and protection of the bio-geosphere.

There are about 90 natural chemical elements, which combine to form the *ca.* 5500 known terrestrial and extra-terrestrial mineral species, distinct by chemical composition and/or crystal structure. Minerals represent, in the words of the great Bulgarian mineralogist Ivan Kostov (1913-2004), "*...milestones of the history of the Earth and of the Cosmos*", as well as a valuable source of information for research on nanotechnologies and innovative materials. They are the product of natural terrestrial and extra-terrestrial laboratories in which laboratory "tests" have been carried out for *ca.* 4.8 billion years on thermodynamic systems characterized by wide ranges of chemical-physical parameters and evolutionary processes (temperature, pressure, activity and mobility of chemical components, electromagnetic radiation, compositional, thermal and baric gradients, gravitational field, etc.).

Beside the use of natural compounds as technologically-important materials (Ferraris and Merlino 2005; Depmeier 2009), mineral structures with their inherent complexity have also represented a treasure trove for new discoveries in crystallography. For example, in the field of aperiodic crystallography, the mineral calaverite ($Au_{1-x}Ag_xTe_2$, with $0 \leq x \leq 0.33$) has been the ideal case to begin to shed light on incommensurability in crystals (Goldschmidt et al 1931). Later, mineralogy played an important role with numerous examples of mineral structures exhibiting modularities (Ferraris et al. 2008), fast ion conducting properties (Kuhs and Heger 1979), non-commensurate (misfit) layer structures (Makovicky and Hyde 1981), currently known under the name of composite structures, and in providing the first example of a (billion years old) natural quasicrystal (Bindi et al. 2009c), which settled any doubt that could remain on the long-term stability of quasicrystals.

In this review we will focus on different aspects of the complexity of mineral structures, including a quantitative definition of crystal-structure complexity (Krivovichev 2013a).

2. Modularity of crystal structures

2.1 Introduction

A crystal structure is composed of a very large number of atoms (neutral or ionized) bonded to constitute a three-dimensional, triperiodic network of atoms and of bonds, which can be represented by a graph, where atoms are vertices and bonds are edges. In molecular crystals, the network of bonds can be decomposed into small sub-units (molecules) characterized by stronger bonds (intramolecular bonds), connected by weaker bonds (intermolecular bonds). Moreover, the transition from a state of matter to another (solid to

liquid, liquid to gas etc.) preserves the molecular entity: ice, water and water vapour are all characterized by the same molecular component, the H_2O molecule, but differ in the way the molecules interact and are arranged one with respect to the other.

Inorganic crystals – here we mean really inorganic crystals, not including crystals of metal-organic compounds that, for some inexplicable reason, are today considered in the "inorganic" realm – are mainly non-molecular: they differ from molecular crystals in that bringing them to fusion (or sublimation) does not preserve structural unit common to the states of matter, i.e., a molecule. The largest majority of minerals are non-molecular. Fusion of halite, sphalerite, pyrite, "biotite", pyrope... (you name it!) does not produce a liquid with intra- and intermolecular bonds.

Nevertheless, the structure of inorganic crystals, including minerals, can too be decomposed into elementary building blocks of variable size. Such a decomposition is often – but not always – an interpretation of the crystal structures, rather than a physical reality. The most typical example is the smallest and universally known building block: the coordination polyhedron. An octahedron of $NaCl_6^{5-}$ or a tetrahedron of ZnS_4^{4-} do not correspond to chemical units comparable to a molecule: yet, the polyhedral interpretation of inorganic and mineral crystals is the basis of crystal chemistry since its dawn (Pauling 1929; Wells 1975).

Bigger and more complex building blocks occur in modular structures, which are built by juxtaposing one or more types of modules. The modules are three-dimensional but have less than triperiodic components (i.e., they are periodic only along one or two directions, or even non periodic at all, in the case of finite components) that can ideally be described as cuts from a structurally and chemically homogeneous parent structure: the *archetype*. This archetype does not necessarily correspond to a real structure. The most well-known example is certainly that of structures that can be described as based on stacking of layers of equal spheres. The most compact layer, in which each sphere is in contact with six other spheres, has hexagonal symmetry. By stacking identical layers on the top of each other, one gets infinitely many stacking variants, which have maximal compactness if the spheres on adjacent layers are in contact too. This is realized when a sphere of a layer is located on the top of a triangular cavity of the preceding layer. If the position of the spheres on a layer is indicated as A, the two types of triangular cavities in the same layer as B and C (Fig. 1), the stacking variants corresponds to sequences (periodic or non-periodic) of the three letters A, B and C with the same letter never occurring in two successive positions. The archetype is a structure with periodicity of one layer: its stacking sequence is therefore AA and it is not a structure with maximal compactness. It does nevertheless occur in structures with covalent bonds, where the overlap of orbitals determines the relative position of the layers. From this triperiodic archetype, one ideally cuts out a diperiodic layer, whose repetition produces many possible stacking variants. The stacking of layers results in interlayer cavities with different geometry and size, which are then partially occupied by other types of atoms (normally, but not always, less electronegative than the atoms represented by the spheres), leading to a large variability of derivative structures (for a detailed analysis, see Umayahara and Nespolo 2018).

A wide range of modular structures is known in the literature. The most complete account of modular structures in minerals can be found in Ferraris et al. (2008). The algebraic description of modular structures requires the theory of groupoids (small categories in which every morphism is invertible) and is outside the purpose of this review. Interested readers are

referred to the order-disorder (OD) theory (Dornberger-Schiff and Grell-Niemann 1961), which is the theory of a subclass of modular structures built of diperiodic layers, although generalisations to rods and blocks have been proposed (Dornberger-Schiff 1964; Belokoneva 2005). A generalisation has been recently introduced by Nespolo et al. (2020).

2.2 Symbolic representation of modular structures

Modular structures can be classified as *monoarchetypal* and *polyarchetypal*, depending on whether the modules can be viewed as obtained from a single archetype or from at least two different archetypes. The chemical composition of the modules of monoarchetypal modular structures is identical, but the juxtaposition of modules may create or annihilate coordination sites at the interface between two modules. As a consequence, the chemical composition of a series of monoarchetypal structures is not necessarily constant; when it is, then the modular structures are simply polytypes. On the other hand, the chemical composition of a series polyarchetypal structures (polysomes) is by definition variable and depends on the ratio between the number of different archetypes building the structure.

In the case of monoarchetypal modular structures, like those based on sphere packings, it is always possible to adjust two modules one next to the other in such a way to form chemical bonds between atoms exposed on the adjacent surfaces of two modules. Depending on the number of possible relative orientations and positions, the number of possible modular structures may increase significantly. If the coordination site at the interface is not affected by the relative arrangement of the modules, then all the monoarchetypal modular structures based on the same type of module are polytypes[1].

Let us indicate the archetype as **A** and a module extracted from it as **M**. Juxtaposing modules **M** in a way to obtain back the archetype **A** can be represented as ${}^{a}\mathbf{M}_{na}{}^{b}\mathbf{M}_{nb}\,{}^{c}\mathbf{M}_{nc}$, where nj (j, = *a, b, c*) indicates that number of modules **M** needed to span the unit cell of **A** along the axis j of the coordinate system. Clearly, to get back the archetype, all the modules are arranged with the same topology one with respect to the preceding (and following) one. This notation applies to non-periodic modules; if the module is monoperiodic (rod or chain) then the repetition along only two axes has to be specified, e.g., ${}^{a}\mathbf{M}_{na}{}^{b}\mathbf{M}_{nb}$ if the module is periodic along *c.* Similarly, if the module is diperiodic (sheet or layer), then the repetition along only one axis has to be specified, e.g., ${}^{c}\mathbf{M}_{nc}$ if the module is periodic along *a* and *b.* For example, the archetype of the structures based on sphere packing is simply $\mathbf{A} = {}^{c}\mathrm{A}_1$, simplified to $\mathbf{A} = {}^{c}\mathrm{A}$ because $nc = 1$, or even $\mathbf{A} = \mathrm{A}$ if it is understood that the only direction lacking periodicity is taken as axis *c* of the coordinate system.

Different modular structures sharing the same archetype can be obtained if the modules **M** are differently oriented and/or positioned with respect to their orientation and position in the archetype. We can differentiate them by an index in parentheses. Monoarchetypal modular structures can then be represented as $\mathbf{M}(1)_{n1}\mathbf{M}(2)_{n2}....\mathbf{M}(\mathrm{m})_{nm}$, where nj is the number of modules **M**(j) that occur continuously in the structure. In this example we suppose a layer structure, so that only one direction of missing periodicity exists. For a rod structure, a 2×2

[1]According to the official definition (Guinier et al. 1984), polytypes are obtained by "stacking layers of (nearly) identical structure and composition" so that the resulting triperiodic structures "differ only in their stacking sequence". The building modules are clearly requested to be layers, although "a more general definition of polytypism that includes 'rod' and 'block' polytypes may become necessary in the future". Here we adopt this larger definition of polytypism.

matrix is in general necessary, to take into account the sequence along the two directions of missing periodicity. For a structure built by non-periodic modules, a 3×3 matrix would be required. In this section, we fix our attention, for the sake of simplicity, on modular structures built by diperiodic modules (sheets or layers) so that a row matrix of symbols is sufficient to describe it; generalization to structures built by mono-periodic or non-periodic structures simply requires adding one or two dimensions to the symbol matrix.

For the sake of simplicity and without loss of generality, let us go back to the case of packing of equal spheres. The three most common polytypes, the hexagonal close packing (*hcp*) or 2*H*, the cubic close packing (*ccp*) or 3*C*, and the double hexagonal or 4*H*, correspond to the sequences AB, ABC and ABAC, respectively. Accordingly:

- 2*H*: **M**(1) = A, **M**(2) = B;
- 3*C*: **M**(1) = A, **M**(2) = B, **M**(3) = C;
- 4*H*: **M**(1) = **M**(3) = A, **M**(2) = B, **M**(4) = C.

The same orientation and position can occur in different places in a single period, as in the example 4*H* above. A somewhat more complex example is that of covellite, CuS, for which the sequence of sulfur atoms is ACAABA (copper occupies some of the cavities formed by stacking of layer of sulfur; Umayahara and Nespolo 2018), or, by a shift of the origin, AACAAB[2], so that its symbolic representation is $\mathbf{M}(1)_2\mathbf{M}(2)\mathbf{M}(1)_2\mathbf{M}(3)$, where **M**(1) = A, **M**(2) = C, **M**(3) = B.

The structure of the interface between two modules also plays a role not only in the classification of modular structures, but also for its stability. Extracting modules from an archetype and rearranging them in order to obtain a new, different structure opens the possibility of a modification of the inter-module coordination. Let us indicate as **I**(i/j) the intermodule region between modules i and j: the modular structure can then be represented as:

$$[\mathbf{M}(1)\mathbf{I}(1/1)_{n1\text{-}1}]\mathbf{M}(1)\mathbf{I}(1/2)[\mathbf{M}(2)\mathbf{I}(2/2)_{n2\text{-}1}]\mathbf{M}(2)\mathbf{I}(2/3)\ldots.\ \mathbf{I}(\text{m-}1/\text{m})\mathbf{M}(\text{m})_{nm}\mathbf{I}(\text{m}/1). \quad (1)$$

Let us again analyse a few examples of structures based on the stacking of spheres. The interlayer region between two layers with different position (A and B, B and C, C and A), contains two types of tetrahedral sites, with the triangular basis parallel to the layer and the fourth, apical corner oriented along the stacking direction (the sites are noted T^+ and T^- depending on whether the apical tetrahedron points along the positive or negative sense of the axis corresponding to the stacking direction) and an octahedral site whose opposite triangular faces are in the layers (noted O) (Fig. 2). The interlayer region between two layers with the same position (A and A, B and B, C and C), contains two types of trigonal pyramidal sites, that we will indicate as P_1 and P_2, respectively (Fig. 3).

- Nickeline, NiAs: 2*H* stacking with the octahedral cavities occupied: COBO. **M**(1) = C, **M**(2) = B, **I**(1/2) = **I**(2/1) = O.

[2] The sequence of layers does not impose a choice of the origin, which is instead restricted once the space-group type of the crystal structure is specified.

- Sphalerite, ZnS: 3*C* stacking with the T^+ cavities occupied: $AT^+BT^+CT^+$. **M**(1) = A, **M**(2) = B, **M**(3) = C, **I**(1/2) = **I**(2/3) = **I**(3/1) = T^+.
- Molybdenite, MoS_2: BP_1BCP_1C. **M**(1) = **M**(2) = B, **M**(3) = **M**(4) = C, **I**(1/1) = **I**(2/2) = P_1, **I**(1/2) = **I**(2/1) = ‖ (where ‖ indicates empty interlayer).

When the intermodular region is constant, all the **I**(i/j) can be simply replaced by **I**, as in the examples of nickeline and sphalerite.

The range of modular structures that can be obtained from a single archetype is actually wider than what is suggested by the examples above. Identical modules obtained from the same archetype can be differently oriented with respect to the orientation in the archetype, and this modifies, sometimes profoundly, the interface.

A number of modular structures composed of two (possibly more) types of modules are also known. They are called *polyarchetypal* because each type of module corresponds to a different archetype. A polyarchetypal modular structure can occur if the interface between the two types of modules is compatible with the formation of chemical bonds. This requirement limits the possibilities of polyarchetypal crystal structures; putting two modules one next to the other does not necessarily results in a configuration compatible with the formation of chemical bonds. Polyarchetypal modular structures are known as *polysomatic structures* (Thompson 1978). The symbolic representation in Eq. (1) applies to polyarchetypal modular structures too; the only difference with respect to the case of monoarchetypal modular structures is that the modules **M**(j) are obtained from two or more different archetypes.

The scope of this brief survey being necessarily limited, we have chosen to analyse in details mono- and diarchetypal modular structures where the building blocks are di-, mono- or non-periodic modules ideally obtained from the TOT layer of phyllosilicates.

2.3 Modular structures whose archetype are phyllosilicates

Phyllosilicates are layer minerals built by stacking layers of different structure and composition. Depending on the type of layers, several phyllosilicate archetypes exist.

Phyllosilicate layers are composed of two types of sheets:

1.corner-sharing tetrahedra (T hereafter) centred around a small cation (mainly silicon, partially substituted by aluminium, iron, titanium); the corners are occupied by oxygen atoms (Fig. 4a);

2. sheets of edge-sharing octahedra (O hereafter) centred around various cations (aluminium, magnesium, iron, manganese, titanium, lithium); the O sheet alone occurs in hydroxide minerals like brucite, $Mg(OH)_2$, in which all the octahedra are occupied (Fig. 4b), and gibbsite, $Al(OH)_3$, in which one third of the octahedra are vacant (Fig. 4c).

In the T sheet, all the tetrahedra have the same orientation with respect to the direction of stacking. Three of the four vertices define the basis of the tetrahedra and the anions on these vertices, called the basal oxygen atoms O_b, define a geometric plane. The fourth corner, occupied by the apical oxygen atoms, connects the T sheet with the O sheet, by replacing the corresponding OH group. In the so-called *Pauling model* the T sheets have hexagonal symmetry. In the real structure, because of the difference in the lateral dimensions of the T and O sheets, tetrahedra rotate around [001] by an amount that depends mainly on the chemical composition but also external conditions like temperature and pressure, so that the

symmetry of the T sheet is reduced to ditrigonal. The model that takes into account this rotation is known as the *trigonal model* (Nespolo et al. 1999).

In the O sheet, the OH groups can be replaced not only by the apical oxygen atoms of the T sheet, also by fluorine, chlorine, oxygen atoms not belonging to the T sheet, or, much more rarely, by sulfur. In the real structure of minerals, these sheets are deformed with respect to their ideal configuration: tetrahedra are actually disphenoids, octahedra are actually trigonal antiprisms (eigensymmetry $\bar{3}m$) or metaprisms (eigensymmetry 32) or even polyhedra with lower symmetry. However, for the sake of simplicity, we retain their idealized description. Readers interested in the real structure of the phyllosilicate layers can find abundant details in Ferraris and Ivaldi (2002).

Depending on how the sheets are arranged in the layers, several archetypes are realized.

1. Layer built by one T sheet and one O sheet (TO layer). Depending on whether the nature of the O sheet, the layer is brucitic, like in the serpentine mineral, or gibbsitic, like in the kaolinite mineral.

2. Layer built by one O sheet sandwiched between two T sheets (TOT layer). Depending on the nature of the O sheet and of the interlayer region, a number of minerals are realized: talc (brucitic TOT without interlayer cations), pyrophyllite (gibbsitic TOT without interlayer cations), micas (with interlayer cations), montmorillonites (smectites) and illites (with the interlayer region only partially filled with cations).

3. A TOT layer alternating with an O sheet, like in the chlorite minerals.

Depending on the distribution of cations occupying the O sheets, phyllosilicates are classified into different families, with a more or less fine classification depending on the purpose of investigation. Here we are interested in the modular structure of these minerals, which does not significantly change with the nature of the cations. Therefore, we can simplify the classification to three archetypes, differing by the type of layer (TO, TOT and TOT:O), each characterised by a period of one layer along the stacking direction. In the following we deal specifically with the TOT archetype, which provides a large number of modular structures occurring in nature.

In the TOT layer, the two T sheets are actually staggered one with respect to the other by about $a/3$ in the projection on the (001) plane (Fig. 5a). As a consequence, most of the symmetry operations of the O sheet are not extended to symmetry operations of the whole layer. Only the inversion, one of the two-fold rotations and one of the mirror reflections are (Fig. 5b). Therefore, the interlayer region has trigonal symmetry (ideally hexagonal) whereas the layer symmetry has only monoclinic symmetry. Stacking two TOT layers one on top of the other can be realized in three orientations (six, in the Pauling model) that correspond to the same configuration of the interlayer region but not of the layer. This leads to three (ideally six) different mutual orientations of the same pair of layers, i.e., three (ideally six) modular structures with the period of two layers, which are simply polytypes. The same situation occurs for *each* pair of layers so that with the increase in the period the number of possible polytypes increases significantly. Furthermore, the interlayer region may be empty or host cations and small molecules, which increases the number of modular structures. Finally, a different module, namely a rod, can be extracted from the same archetype, leading to a large number of modular structures which differ for the relative position of these rods along *two* directions and for the nature of the intermodular region.

335

336 **2.3.1 Layer modular structures**

337 Modular structures where the module is a TOT layer can be represented by Eq. (1) in
338 which all the modules **M** have the same chemical composition and structure but differ for
339 their relative orientation and/or position. These can be identified as follows.

340 • The TOT layer has monoclinic symmetry. The relative orientation of two TOT layers
341 can be specified by the orientation of the unique symmetry direction in each of the two
342 layers. Although in principle infinitely many relative orientations are possible, the
343 ditrigonal (ideally hexagonal) symmetry of the plane of basal oxygen atoms actually
344 restricts these orientations of multiples of 60°, which correspond to orientations under
345 which the coordination sites in the interlayer region is unchanged.

346 • Mapping of one layer onto the adjacent one can be obtained by a twofold rotation about
347 a direction in the interlayer region, followed by a shift along the same or another
348 direction again in the interlayer region. In the following, we will differentiate modular
349 structures based on the stacking of TOT layers in "zero-shift" and "non-zero-shift",
350 depending on whether the shift component of this mapping is absent or present. The
351 zero-shift configuration preserves the coordination sites in the interlayer region,
352 whereas the non-zero-shift modifies it.

353 In each TOT modular structure, the interlayer region is essentially the same between
354 each pair of layers and can be empty or contain cations, small molecules or more complex
355 components, like the O sheet one finds in chlorites. The archetype is simply **A** = **M**, in which
356 the unit cell contains a single layer; two adjacent layers, in successive unit cells, are in parallel
357 orientation and have zero-shift relative position.

358

359 **2.3.2 Modular structures with empty interlayer region**

360 The simplest modular structures obtained by stacking TOT layers are those in which the
361 interlayer region is empty. Stacking the layers with parallel orientation and with the same shift
362 results in a one-layer period. For zero-shift the result would be the archetype, which however
363 is not realized in nature. The 1*A* (one-layer period, triclinic) polytype has a non-zero shift
364 between the TOT layers in two successive unit cells. Fig. 6a and 6b show, respectively, the
365 structure of talc and of pyrophyllite, which differ by the content of the O sheet (Mg filling all
366 the octahedral cavities vs. Al filling two third of them, respectively). The lower T sheet has
367 been removed for the sake of clarity. Fig. 7a and 7b show a different section of the same
368 structure, with two adjacent T sheets belonging to two successive TOT layers, from which the
369 O sheets have been removed. The ditrigonal cavities (ideally hexagonal) have parallel
370 orientation but are shifted by about $a/3$ for talc ($0.2968a$, Fig. 7a) and about 1/10 along the
371 [120] direction for pyrophyllite (Fig. 7b). Both talc and pyrophyllite occur also in a different
372 polytype, 2*M* (two-layer period, monoclinic), where again adjacent layers show non-zero
373 shift. The majority of polytypes are however disordered, i.e., without a periodicity along the
374 stacking direction. This is the result of the weak van der Waals bonds between successive
375 layers, which are not interlocked by the presence of cations or small molecules.

2.3.3 Modular structures with cations in the interlayer region

The presence of cations in the interlayer region is characteristic of micas. Depending on whether the cations are mono- or divalent, micas are classified in *true micas* and *brittle micas*. These cations lock successive TOT layers in zero-shift configuration, but the relative rotations of $n\times60°$ (n integer) result in a large number of polytypes. The strong ionic bonds between the cations and the basal oxygen atoms of the tetrahedra belonging to two adjacent TOT layers are considered responsible for the occurrence of periodic polytypes with variable, sometimes very large, periodicities (Nespolo and Ďurovič 2002).

In the Pauling model, the six $n\times60°$ orientations all correspond to the same configuration of the interlayer region. In the trigonal model, this sixfold degeneration is partly resolved. Even ($2n\times60°$) orientations result in a staggered configuration of the basal oxygen atoms (Fig. 8a, phlogopite-1*M*: Redhammer and Roth 2002), whereas odd [$(2n+1)\times60°$] orientation in an eclipsed orientation (Fig. 8b, phlogopite-2*O*: Ferraris et al. 2001; and Fig. 8c, lepidolite-$2M_2$: Guggenheim 1981). This difference is considered one of the reasons for the higher occurrence frequencies of polytypes showing even orientations. Furthermore, minerals with inhomogeneous occupation of the octahedral sites, in particular those where one of the three independent sites is empty, result in a tilting of the tetrahedra which makes the plane of the basal oxygen atoms no longer flat but corrugated, and this further destabilizes odd-rotation configurations (Fig. 9).

Partial occupation of the interlayer region occurs in some clay minerals like illite (K-poor muscovite) and montmorillonite (showing incomplete occupation of the interlayer region by cations like Na^+ and Ca^{2+}). The configuration of the interlayer region in illite is essentially the same as in muscovite, whereas that in montmorillonite, characterized by a lower occupancy in the interlayer region, is closer to that of pyrophyllite.

2.3.4 Modular structures with an O sheet in the interlayer region

The alternate sequence of TOT layers and O sheets is typical of chlorite. The presence of an O sheet in the interlayer region leads to hydrogen bonds between the hydroxyl groups on the surface of this sheet and the basal oxygen plane of the TOT sheets next to it. This network of hydrogen bonds results in a non-zero-shift of successive TOT layers. Fig. 10 shows the 1*M* polytype of chlorite (Zanazzi et al. 2007): successive TOT layers are equally oriented but shifted by $0.42a$.

Hydrogen bonds are stronger than van der Waals bonds, but definitely weaker than ionic bonds. This partly explains the scarcity of periodic polytypes in chlorite with respect to micas.

2.3.5 Rod modular structures

The TOT layer can be imagined as built by three separate sheets (two T sheets and an O sheet) that are attached one on the top of the other. The apical oxygen atoms of the T sheets replace two thirds of the hydroxyl groups of the O sheets. The remaining OH groups allow to differentiate the octahedral sites. The primitive unit cell contains three octahedral sites: one has the OH groups in *trans* configuration, the two others in *cis* configuration (Fig. 11).

The TOT layer can be cut in rods with different widths, which can the assembled together to produce a wide range of minerals. The juxtaposition of two rods implies a

positional, but no rotational, degree of freedom, contrary to the case of layers, which are diperiodic. The result depends on several factors.

- The width of the rod, which is measured by the number of full octahedra it contains; a rod *n*-octahedra width is indicated as R_n. Fig. 12 shows rods R_5 and R_8. Clearly, moving along *a*, the boundaries of a rod pass either through the oxygen atoms / hydroxyl groups (defining full octahedra) or cations (cutting through the octahedra). The former are taken as measure of the width of the rod.
- The occupation of the regions between pairs of rods, along the two directions of missing periodicity.
- The bonding scheme between pairs of rods.

Because the modules are monoperiodic, Eq. (1) has to be generalized to a 2×2 matrix form. The T and O sheet in the TOT layer become there the T and O chain of the TOT (R_n) rod. The TOT phyllosilicate archetype can be written as

$$\begin{matrix} R_n \\ \square \end{matrix}$$

where □ represents the empty region between successive layers. The first line represents the layer itself; indeed, a layer can be interpreted as an infinite juxtaposition of rods *n*-octahedra width for any value of *n*. The second line shows the interlayer region is empty. Modular structures built by the juxtaposition of rods can be represented by extending the above notation, which however cannot account for the bonding scheme between pairs of rods, which is realized in two ways:

1. the OH-O_b scheme, obtained by replacing an hydroxyl group of the O chain by the basal oxygen atom of a neighbouring T chain;
2. the O_b-O_b scheme, obtained by sharing the basal oxygen atom of two neighbouring T chains.

The following analysis is a schematic version of the publication of Nespolo and Bouznari (2017). Rod modular structures with the OH-O_b scheme are shown in Figs. 13-15. Fig. 13 shows the structure of amphiboles, which can be interpreted as composed by R_5 rods, periodic along the *c* axis of the mineral, displaced one with respect to the other along the *a* axis. Exactly the same topology occurs in jimthompsonite, which is built by rods R_8 instead of R_5 (Fig. 14). The structure of the two minerals can be represented as

$$\begin{matrix} R_n & X\square X \\ X\square X & R_n \end{matrix}$$

where □ represents empty space, X is a cation, and $n = 5$ or 8 respectively. Depending on cations occupying the O chain and the nature of the X cation amphiboles are classified in a number of different minerals. In some of these, the empty space ⟧ is sometimes occupied by a monovalent cation, mainly sodium. A similar variation has not been found in jimthompsonite.

Intermediate structures do exist as well. Fig. 15 shows the structure of chesterite, which can be schematically represented as

$$\begin{matrix} R_5 & X\square X \\ X\square X & R_8 \end{matrix}$$

i.e., by an alternation of amphibole-like modules and jimthompsonite-like modules.

Rod modular structures with the O_b-O_b scheme are shown in Fig. 16-18. The sequence of R_5 and of R_8 rods is found in palygorskite and sepiolite respectively, where water molecules occur instead of the X cations of amphiboles (Figs. 16 and 17). It can be symbolically represented as

$$\begin{matrix} R_n & H_2O \\ H_2O & R_n \end{matrix} .$$

A further modular structure is known as well, kalifersite, which shows an alternation of R_3 and R_6 modules, i.e.,

$$\begin{matrix} R_3 & \square \\ \square & R_6 \end{matrix}$$

(Fig. 18).

The symbolic representation adopted here has the advantage of being synthetic and illustrative but does not have the ambition to express the difference in the relative position of the modules. Our purpose here is to point out and emphasize the tight structural relations between minerals that were only partially recognized in the past (Thompson 1978). For a full structural information, one needs a more detailed description; interested readers are referred to Nespolo et al. (2018).

2.4 Polyarchetypal modular structures. The example of pyroxenoids

Polyarchetypal modular structures are built by the juxtaposition of modules taken from two or more archetypes. A large number of examples can be found in Ferraris et al. (2008). Our aim is to illustrate the general principle in the simplest possible way. For that, we restrict our treatment to one of the two series of pyroxenoids, diarchetypal minerals whose modules, although different, can again be obtained from the TOT layer of phyllosilicates (Angel and Burham 1991).

Pyroxenoids are metamorphic minerals with variable chemistry and occurrence. They are classified on the basis of two parameters (Takéuchi 1997).

1. The period along the direction of the T chain, which is of three or more tetrahedra. Wollastonite, whose T chain has a period of three tetrahedra, is one archetype. The second archetype is not a pyroxenoid but a pyroxene, whose T chain has a period of two tetrahedra.
2. The width of the O chain, sandwiched between two T chains, measured roughly perpendicularly to the direction of the T chains, variable between two and three cation sites. These sites have only approximate octahedral geometry, but in the following we will treat them as octahedral for the sake of simplicity.

Fig. 19a shows the structure of the first archetype, wollastonite, $CaSiO_3$, along the *b* axis. The O chain has a width of three octahedra. Fig. 19b shows the same structure along [101]*, with the cation sites in a ball-and-stick representation instead than polyhedral. The period of the tetrahedral chain is three tetrahedra. The structure of wollastonite can therefore be described as obtained by juxtaposition of TOT rods composed of tetrahedral chains with period of three tetrahedra and octahedral chains three-octahedra wide. These rods can be represented as $R^T{}_O = R^3{}_3$, where ^{T} indicates the number of tetrahedra defining the period of the T chain and $_O$ the number of octahedra defining the width of the O chain.

Fig. 20a and 20b show the structure of the other archetype, a pyroxene, $(M2M1)SiO_3$ (M2 = Ca, Mg, Fe^{2+}, Na, Li, M1 = Mg, Fe^{2+}, Al^{3+}, Fe^{3+}) along [001] and along [101] respectively. The larger site (white polyhedron in Fig. 20a, usually indicated as M2 in the literature) does not have an octahedral geometry but in this treatment we approximate it to an octahedron. The rods building the structure of pyroxenes can therefore be represented as $R^T{}_O = R^2{}_2$.

Fig. 21 shows the structure of rhodonite group minerals (Shchipalkina et al. 2019), $CaMn_4Si_5O_5$, seen along [100]*. This structure is composed by a regular alternation of wollastonite-like slabs and pyroxene-like slabs. The slabs are cut from the rods and are therefore non-periodic. We can represent it as $S^3{}_3S^2{}_2$, where $S^T{}_O$ stands for "slab" O octahedra thick obtained from the chain $R^T{}_O$.

Fig. 22 shows the structure of pyroxmangite, $MnSiO_3$, along [100]*, which is composed by a regular alternation of one wollastonite-like slabs and two pyroxene-like slabs. It can be represented as $S^3{}_3(S^2{}_2)_2$.

Fig. 23 shows the structure of ferrosilite-III, $FeSiO_3$, along [110]*, which is composed by a regular alternation of one wollastonite-like slabs and three pyroxene-like slabs. It can be represented as $S^3{}_3(S^2{}_2)_3$.

These five minerals can be seen as representative of a potentially large family of diarchetypal modular structures, whose general member is $S^3{}_3(S^2{}_2)_n$. Members known so far correspond to $n = 0$ (wollastonite, first archetype), $n = 1$ (rhodonite), $n = 2$ (pyroxmangite), $n = 3$ (ferrosilite-III) and $n = \infty$ (pyroxene, second archetype). The period of the T chains is $2n+3$ tetrahedra; for the pyroxene archetype, $n = \infty$ indicates the absence of wollastonite-like slabs so that the period corresponds to the thickness of a $S^2{}_2$ slab, i.e. two tetrahedra.

3. Information-based analysis of structural complexity of minerals

3.1. Introduction

The problem of quantifying the complexity of natural and artificial structures is of high importance for modern science that deals with more and more complex systems in the course of its development. Crystals are considered as intuitively simple systems (Bennet 1990), due to the periodic character of their structures, and their complexity was the subject of thought for crystallographers at the very beginning of the development of X-ray diffraction analysis. In particular, Pauling (1929) suggested the parsimony rule that states that '…the number of different types of constituents in a crystal tends to be small'. The topic of structural complexity of crystals reappeared in scientific literature many times (see Krivovichev (2013a, 2016b, 2017) for historical remarks), but only recently the universal measures were suggested based upon the Shannon information theory (Krivovichev 2012a, b, 2013a, b, 2014, 2016a). Below we formulate the basic principles of this method by considering an *n*-dimensional crystal structure in order to cover both classical crystals and those that can be described using superspace approach.

3.2. Structural complexity measures

The complexity of a crystal structure can be estimated as the amount of Shannon information per atom (represented by a point), ${}^{str}I_G$, and per unit cell, ${}^{str}I_{G,total}$, calculated according to the following equations:

$$ {}^{str}I_G = -\sum_{i=1}^{k} p_i \log_2 p_i \quad \text{(bits/atom)} \qquad (1), $$

$$ {}^{str}I_{G,total} = -v\, I_G = -v \sum_{i=1}^{k} p_i \log_2 p_i \quad \text{(bits/cell)} \qquad (2), $$

where k is the number of different crystallographic orbits in the structure and p_i is the random-choice probability for an atom from the ith crystallographic orbit, that is:

$$ p_i = m_i / v \qquad (3), $$

where m_i is the number of points of the crystallographic orbit in the reduced unit cell[3], and v is the total number of atoms in the reduced unit cell.

The Shannon information measures are applicable to any crystalline structure that can be characterized by a finite amount of atoms located in a finite amount of space with defined equivalence relation among atomic sites (including trivial symmetry). The two measures of structural complexity, ${}^{str}I_G$ and ${}^{str}I_{G,total}$, reflect upon the two important properties of complexity, size and symmetry of a system. While the parameter ${}^{str}I_G$ is sensitive to symmetry, the parameter ${}^{str}I_{G,total}$ is sensitive to both symmetry and the number of translationally independent sites, i.e. the size of a system.

The equations (1-3) do not take into account the complexity of bonding network in the crystal structure, which can be accounted for by introducing additional measures (e.g., by including bonds into consideration (see (Krivovichev 2013a) for more details).

The equations (1-3) may be used to calculate *information density*, ρ_{inf}, of a crystal structure as the amount of Shannon information per volumetric unit, e.g. per cubic Ångström:

$$ \rho_{inf} = {}^{str}I_{G,total} / V_{red} \qquad (4), $$

where V_{red} is the volume of the reduced unit cell. The information density is the parameter that can be strictly applied to one unit cell only and not to the whole crystal, since the periodicity condition of a crystal structure would result in the redundant character of all information except for the one contained in a single reduced unit cell.

3.3. Applications: general overview

Krivovichev (2013a, 2014) calculated information-based structural complexity parameters for all known inorganic and mineral structures and classified them according to their ${}^{str}I_{G,total}$ parameter value into five groups (bits/cell): very simple (0-50), simple (50-100), intermediately complex (100-500), complex (500-1000), and very complex (> 1000 bits/cell). The procedure of the information-based measures of structural complexity calculation in

[3] A reduced cell is a primitive (minimal volume) cell satisfying two restrictions on the basis vectors **a**, **b**, **c**: 1) of all lattice vectors, none is shorter than **a**; of those not directed along **a**, none is shorter than **b**; of those not lying in the **ab** plane, none is shorter than **c**; 2) The three angles between basis vectors are either all acute (type I) or all non-acute (type II).

incorporated into the TOPOS Pro program package (Blatov et al., 2014), which is freely available for download.

For minerals, Krivovichev (2013a) provided the following average values of information-based structural complexity measures: $< {}^{str}I_G > = 3.23(2)$ bits/atom and $< {}^{str}I_{G,total} > = 228(6)$ bits/cell. However, these calculations were based upon partial structural information, since for many crystal structures of hydrated minerals, the positions of H atoms have not been determined in the original structural studies. For hydrated Ca borates, Pankova et al. (2018) used the procedure of H-corrections by introducing surrogate H sites into the structure data, and this procedure was recently performed for all mineral species known to date (unpublished). The new average complexity parameters for minerals are: $< {}^{str}I_G > = 3.48(2)$ bits/atom and $< {}^{str}I_{G,total} > = 303(6)$ bits/cell. The increase in the average values is due not only to the inclusion of H atoms into calculations, but also owing to the fact that more and more complex minerals are discovered in nature due to the applications of novel experimental techniques, including high-sensitive area detectors, the use of synchrotron radiation and the advances in electron diffraction methods.

3.4. Most complex mineral structures

Table 1 provides the list of five most complex mineral structures known in April 2020.

Ewingite, $Mg_8Ca_8[(UO_2)_{24}(CO_3)_{30}O_4(OH)_{12}(H_2O)_8](H_2O)_{130}$, is the Earth's most complex mineral reported so far with the estimated complexity of 23477.507 bits/cell. The mineral was found as golden-yellow crystals formed on a damp wall of the old Plavno mine of the Jáchymov ore district, western Bohemia, Czech Republic (Olds et al. 2017), where crystallized from low-temperature uranyl-bearing aqueous solutions. Its crystal structure contains a 54-nuclear (24U + 30C) uranyl carbonate cluster $[(UO_2)_{24}(CO_3)_{30}O_4(OH)_{12}(H_2O)_8]^{32-}$ shown in Fig. 24a. Its skeletal representation (Fig. 24b), where each node corresponds either to U (yellow) or to C (grey) center emphasizes the presence of four U_3 triangles (with the U-U distances shorter than 4 Å) that correspond to the trimers of three $((UO_2)O_5)$ pentagonal bipyramids sharing the same equatorial O atom. Two other building units are the $[(UO_2)(CO_3)_3]$ and $[(UO_2)(CO_3)_2(H_2O)_2]$ hexagonal bipyramids. The visual complexity of the cluster architecture can further be reduced by leaving only U atoms and the addition of the U-U links corresponding to the U-U distances in between 4 and 6.2 Å (Fig. 24c). The resulting graph can be considered as consisting of four U_3 trimers (U-U < 4 Å) and six U_4 dihedra of two edge-sharing U_3 triangles (U-U = 4.0-6.2 Å). The centers of the trimers and the dihedra (denoted by red and blue circles in Fig. 24c) form tetrahedron and octahedron, respectively, with six tetrahedral edges in correspondence to six octahedral vertices (Fig. 24d). Such a relation between the tetrahedral and octahedral graphs is known in graph theory as an edge-to-vertex duality. The octahedral graph can be obtained from the tetrahedral graph K_4 by associating a vertex with each edge of the K_4 graph and connecting two vertices with an edge if the corresponding edges of K_4 have a vertex in common (Gross and Yellen 2006). Therefore, the topology of the uranyl carbonate cluster in ewingite, in addition to its extreme complexity, has the interesting property of being self-edge-to-vertex dual.

Morrisonite, $Ca_{11}[As^{3+}V^{4+}{}_2V^{5+}{}_{10}As^{5+}{}_6O_{51}]_2 \cdot 78H_2O$, has 13558.354 bits of Shannon information per unit cell and, after ewingite, is the second most complex mineral known so far. The vanarsite-group minerals (Kampf et al. 2016, 2020) contain unique and previously unknown type of the V-As POM cluster with the composition $[As^{3+}V_{12}As^{5+}{}_6O_{51}]$. The cluster consists of twelve (VO_6) octahedra forming wheel- or corona-shaped unit centered by As^{3+} cation in a trigonal-pyramidal coordination (due to the stereoactivity of a lone-electron pair) and surrounded by six $(As^{5+}O_4)$ tetrahedra (Fig. 25). The vanarsite-group minerals form from low-temperature aqueous solutions with V and As derived from the oxidation of primary unoxidized phases.

Ilmajokite, $Na_{11}KBaCe_2Ti_{12}Si_{37.5}O_{94}(OH)_{31}\cdot 29H_2O$, is the third most complex mineral, which was first reported from the hydrothermal vein in Karnasurt Mountain, Lovozero, Kola Peninsula, Russia (Bussen et al. 1972). The mineral easily dehydrates in air, which prevented its structure solution for more than forty-five years. Recently, Zolotarev et al. (2020) were finally able to solve the crystal structure and described it as a multilevel hierarchical framework structure (Fig. 26). The crystal structure is based upon a 3D titanosilicate framework consisting of trigonal prismatic titanosilicate (TPTS) clusters centered by Ce^{3+} in [9]-coordination. There are two symmetry-independent clusters within the unit cell (Fig. 27). In each cluster, three $[Ti_2O_{10}]$ dimers of edge-sharing TiO_6 octahedra in parallel orientation form a trigonal prism centered by Ce^{3+} cations. The triple-dimer titanate structure is surrounded by SiO_4 tetrahedra to form a TPTS cluster. Four adjacent TPTS clusters are linked into four-membered rings within the (010) plane and linked into ribbons parallel to $[\acute{1}01]$. The ribbons are organized into layers parallel to (010) and modulated with a modulation wavelength of 32.91 Å and an amplitude of 13.89 Å. The layers are further linked into a the titanosilicate framework via additional SiO_4 tetrahedra. The Na^+, K^+, Ba^{2+} and H_2O groups occur in the framework cavities and have different occupancies and coordination environments. As it was mentioned above, the crystal structure of ilmajokite possesses a multilevel hierarchical structure (Fig. 28). The first (lowest) level consists of atoms that are grouped into coordination polyhedra (second level). The TiO_6 octahedra are linked to form dimers (third level). The dimers together with SiO_4 tetrahedra and centering Ce^{3+} cations comprise TPTS clusters (fourth level). The clusters are linked to form four-membered rings (fifth level), which are further interlinked to form ribbons (sixth level). The ribbons are united into a three-dimensional octahedral-tetrahedral framework (seventh level), which, together with alkali metal, Ba^{2+} cations and H_2O molecules complete the structure organization (eighth level). The hierarchical complexity is reflected in the high amount of Shannon information, 11990.129 bits per unit cell after H-correction.

Paulingite-(Ca) (Lengauer et al. 1997) and fantappieite (Cámara et al. 2010) are two aluminosilicates based upon frameworks consisting of corner-sharing TO_4 tetrahedra (T = Al, Si). Both frameworks can be considered as built up by the linkage of polyhedral cages as described elsewhere (Krivovichev 2013a,b). The two minerals represent good examples illustrating the variety of contributions to the total structural complexity, including the difference between structural and *topological* complexity, when the latter is estimated as a Shannon information content of the ideal structure with the maximal possible symmetry (Krivovichev, 2018). For instance, the topological complexity parameters for the paulingite framework (PAU) are 1008 atoms per cell, 4.726 bit/atom and 4763.456 bit/cell with the maximal symmetry space group $Im\bar{3}m$ identical to that of the mineral (Table 1). The addition of interstitial species (Ca^{2+} cations and H_2O molecules) results in the approximately doubling increase of the number of atoms (from 1008 to 1988) and the total information per cell (from 4763 to 11591 bits). In the case of fantappieite, the situation is different. The topological symmetry of the framework is $R\bar{3}$, which is higher than the space group of the mineral, $P\bar{3}$. The topological complexity of the tetrahedral framework per cell is 878.790 bits, but the perfect Al/Si ordering over tetrahedral sites results in the decrease of the symmetry from $R\bar{3}$ to $P\bar{3}$ (which is the *topochemical* symmetry group for the framework) and the increase of the structural information per cell from ~879 to ~2636 bits (Krivovichev 2013b). The filling of

675 the framework cavities by cations and H_2O molecules more than doubles the complexity to
676 ~6112 bits per cell.
677 The five most complex mineral structures reflect the basic mechanisms of the
678 generation of crystal-structure complexity of minerals: the formation of nanoscale large
679 polyatomic clusters (usually polyoxometalates (Krivovichev 2020)) and the modular
680 architecture, when the structure is based upon a combination of one or several large modules
681 (Krivovichev 2013a). The high hydration states also favor the high Shannon information
682 content, due to the high number of H atoms.
683
684 **3.5. Information-density analysis**
685 The structural information densities for ewingite, morrisonite and ilmajokite are in the
686 range of 0.488-0.793 bits $Å^{-3}$, which is equivalent to 4.88-7.93·10^{23} bits cm^{-3}. However, it
687 should be taken into account that the information density is the function of the size of the
688 atoms, and the high hydration states of the three minerals contribute essentially to the ρ_{inf} high
689 values. For anhydrous minerals, the information density is much lower. The variations of
690 information density versus the ionic size can be illustrated by the example of suanite,
691 $Mg_2B_2O_5$, and natrosilite, $Na_2Si_2O_5$, which have the same total structural information content,
692 114.117 bits/cell (Krivovichev 2013a). However, their information densities are drastically
693 different (0.333 and 0.242 bits $Å^{-3}$, respectively), which is an obvious consequence of the
694 different ionic radii of the Mg^{2+} and Na^{+} ions, on one hand, and of the B^{3+} and Si^{4+} ions, on the
695 other.
696 It is notable that the structural information density of minerals (~n·10^{23} bit cm^{-3}) is many
697 orders higher than the volumetric densities of information of hard disks and flash memory
698 (~10^{13} and 10^{16} bit cm^{-3}, respectively), and even exceeds those of DNA memory in both liquid
699 and crystalline states (~10^{19} and 10^{21} bit cm^{-3}, respectively) (Zhirnov et al. 2016). However, it
700 should be kept in mind that the Shannon information in crystals is redundant due to their
701 periodic structure, and the original information is restricted to one reduced unit cell only. On
702 the other hand, the estimate of ~n·10^{23} bit cm^{-3} can be seen as a possible maximum for
703 information storage attainable by the manipulation of matter on the atomic scale, if future
704 technologies would allow to build an aperiodic structure with each atom having a precise
705 position relative to its environment. It should also be mentioned that the information density
706 discussed herein and in the section 3.2 relates to the ideal crystalline state and does not take
707 into account other information contained in each mineral crystal such as defects, trace and
708 minor elements, isotopes and other chemical inhomogeneties, etc., which bears on the unique
709 geological and geochemical history of minerals. In order to quantify this information, one has
710 to develop other approaches, perhaps exceeding the limits of the Shannon theory.
711
712 **3.6. Chemical complexity**
713 The information-theoretic approach allows for the investigation of relations between
714 structural and chemical complexity. The latter can be defined by analogy with the structural
715 complexity (equations 1-4) as the amount of chemical Shannon information per atom and per
716 formula unit (f.u.). In order to do this, the crystal chemical formulae of minerals should be
717 written in a canonical way in order to determine the minimal set of species-defining
718 constituents (i.e., chemical elements that are dominant in particular sites in a crystal

structure). It should be noted that the assignment of an element as species-defining is determined by the rules of the definition of new mineral species given by the International Mineralogical Association (Mandarino et al. 1984; Nickel 1992, 1995). The 'canonical' formulae of minerals are stored in the official IMA list of mineral species continuously updated by Pasero (2020).

The information-based analysis of chemical complexity was first suggested in (Siidra et al. 2014). Following this approach, for the idealized chemical formula of a mineral or inorganic compound, $E^{(1)}_{c1}E^{(2)}_{c2}\ldots E^{(k)}_{ck}$, where $E^{(i)}$ is an *i*th chemical element in the formula and c_i is its integer coefficient, the chemical information can be calculated as follows:

$$ {}^{\text{chem}}I_G = -\sum_{i=1}^{k} p_i \log_2 p_i \quad \text{(bits/atom)} \quad (5), $$

$$ {}^{\text{chem}}I_{G,total} = e\,{}^{\text{chem}}I_G = -e\sum_{i=1}^{k} p_i \log_2 p_i \quad \text{(bits/f.u.)} \quad (6), $$

where k is the number of different elements in the formula and p_i is the random-choice probability for an atom of the *i*th element, that is:

$$ p_i = c_i / e \quad (7), $$

where e is the total number of atoms in the chemical formula:

$$ e = \sum_{i=1}^{k} c_i \quad (8). $$

The average chemical complexity values obtained from the analysis of chemical complexity of all mineral species known today are: $< {}^{\text{chem}}I_G > = 1.62(2)$ bits/atom and $< {}^{\text{chem}}I_{G,total} > = 62(6)$ bits/cell. Note that the chemical complexity parameters are smaller than the structural complexity ones. It was shown that the structural and chemical complexities of minerals correlate strongly, though the character of this correlation is different for different measures (Krivovichev et al. 2018).

Fedorov (1913, 1914) and Groth (1921) pointed out that, in general, symmetry of crystalline compounds correlates with their chemical complexity. Less complex compounds (e.g., elements) tend on average to have higher symmetries than compounds consisting from two elements, etc. Both Fedorov and Groth pointed out that this empirical observation, also known as a Fedorov-Groth law, has an 'approximate' character only, i.e. is of statistical nature that allows exceptions, but works on a global scale. Recently, it was demonstrated that the Fedorov-Groth law is valid and statistically meaningful, when chemical complexity is expressed according to the equation (5) as the amount of Shannon chemical information per atom and the degree of symmetry as the order of the point group of a mineral (Krivovichev, Krivovichev 2020).

4. Structural complexity, disorder phenomena and the rise of ionic properties

4.1 Introduction

One of the most fascinating aspects related to the complexity of mineral structures is related to the concept of disorder, and, to be more specific, to ionic conduction phenomena related to disorder. Although in an ideal periodic compound there is little space for an atom to diffuse, structural defects due to minor positional disorder (slight deviations from the ideal stacking) commonly exist. What seems an unimportant disorder may be responsible for the existence of different polytypes of the same compound and for the stabilization of different structures as a function of temperature and pressure. From a thermodynamic point of view, at 0 Kelvin the atoms of an ideal crystal are arranged in a way to get the lowest free energy. With increasing temperature, the entropic contribution (a measure to quantify the disorder) to the free energy becomes important. As a consequence, there is the occurrence of crystal defects, which can be simply considered the response of the system to reduce the free energy through an increase in the entropy. Crystal defects that play an active role in ion conduction are 'Schottky' and 'Frenkel' defect, the so-called 'point defects' in crystals. Thanks to them, ions can be either brought across the solid giving rise to conductivity (*vacancy migration*) or moving to an interstitial site and then subsequently jump to a neighbouring interstitial site and so on, resulting in long distance motion of the ion (*interstitial migration*).

From the discussion above it is evident that there is a close interplay between the ion motion and the crystal structure where the motion occurs. Indeed, the long-range motions of ions that lead to high conductivity in solids require high density of mobile-ion-sites along with a network of 'smooth' conduction channels connecting them (Padma Kumar and Yashonath 2006). For this reason, a detailed understanding of the structural features is of particular importance in the context of ionic conductors.

Superionic conductors or fast ion conductors have a massive use in diverse technological applications: as electrolytes in batteries used in pace-makers, mobile telephones, laptops, and in electrochemical devices as electrode materials. Interestingly, some of them have been discovered in nature and characterized before their use as synthetic compounds. In other cases, Nature has been of inspiration for new technologically-important materials.

Among the most important materials for solid electrolyte applications there are "NASICONs compounds", $NaSbO_3$, known in nature as the mineral brizziite (Olmi and Sabelli 1994), and Ag-Cu sulfosalts (e.g., Bindi and Biagioni 2018). Below, a brief description of the first two compounds together with a more exhaustive essay of Ag-Cu-sulfosalts is reported.

4.2 NASICON

The term "NASICON" is applied to the solid with chemical formula $Na_4Zr_2(SiO_4)_3$. Actually, it describes a series of compounds with the general formula $Na_{1+x}Zr_2Si_xP_{3-x}O_{12}$, where $0 < x < 3$. There are a number of chemically and structurally related compounds to NASICONs, including langbeinite, $K_2Mg_2(SO_4)_3$ (Mereiter 1979), a very well-known mineral for its technological importance (Krivovichev 2009). The structure of NASICON is based upon the octahedral-tetrahedral framework shown in Fig. 29. Each octahedron shares vertices with six adjacent tetrahedra and each tetrahedron shares vertices with four adjacent octahedra.

4.3 $NaSbO_3$, brizziite

The structure of brizziite is similar to those of the ilmenite group minerals and consists of gibbsite-type octahedral sheets, perpendicular to the *c* axis (Fig. 30). The bond distances of

the Na-polyhedron are in the range 2.25-2.78 Å, whereas the Sb-octahedron exhibits a mean bond distance of 1.989 Å. Each Na and Sb octahedron shares edges with three symmetry-related octahedra to form Na and Sb layers, respectively. Each octahedron also shares a face with another octahedron of an adjacent layer, but the opposite face is unshared. Thus, pairs of Na and Sb octahedra alternate with octahedral holes along the *c* axis. There are six alternating Na and Sb sheets in the unit cell, to form a hexagonal close-packed framework. Such a structure is responsible for the high ionic conductivity measured (Wang et al. 1994).

4.4 Ag- and Cu-bearing sulfosalts

Most of Ag- and Cu-bearing sulfosalts represent an outstanding example of complex structures associated with ionic conduction. Their structural complexity is mainly due to the difficulty in accurately describing the Ag^+ or Cu^+ electron density. Indeed, both Ag^+ or Cu^+ d^{10} elements easily adopt various complex asymmetric coordinations due to an *s*/*d* orbital mixing and/or polarization factors (Gaudin et al. 2001 and references therein). Therefore, both these ions can be found in different, but very close sites, which favour the presence of strong ionic conductivity. As described above, the ease to deform the electron density lowers the activation energy of the site-to-site jumps giving rise to some disorder in the crystal structure. In fast ionic conductors, an ionic species can move easily, giving a liquid-like structure in an open framework (tunnels, layers, etc.).

4.4.1 Pearceite, polybasite and fettelite

The pearceite-polybasite minerals have been known for a long time and were divided by Frondel (1963) into two series: the first one, formed by pearceite $(Ag,Cu)_{16}(As,Sb)_2S_{11}$ and antimonpearceite $(Ag,Cu)_{16}(Sb,As)_2S_{11}$, characterized by a "small" unit cell [labeled 111] and high Cu content, and the second one, formed by polybasite $(Ag,Cu)_{16}(Sb,As)_2S_{11}$ and arsenpolybasite $(Ag,Cu)_{16}(As,Sb)_2S_{11}$, with double unit-cell parameters [labeled 222] and low Cu content. Moreover, the existence of an intermediate type of unit cell labeled 221 was claimed for both polybasite (Harris *et al.* 1965; Edenharter *et al.* 1971) and arsenpolybasite (Minčeva-Stefanova *et al.* 1979). From the crystallographic point of view these minerals were initially reported as monoclinic *C*2/*m*, although dimensionally pseudo-hexagonal (Peacock and Berry 1947; Frondel 1963; Harris *et al.* 1965; Hall 1967; Sugaki *et al.* 1983). Bindi *et al.* (2006a) solved and refined the crystal structure of pearceite in a space group of type $P\bar{3}m1$ (Fig. 31). They showed that the pearceite structure can be described as a regular alternation of two module layers stacked along the *c* axis: a first module layer (labeled *A*), with general composition $[(Ag,Cu)_6(As,Sb)_2S_7]^{2-}$, and a second module layer (labeled *B*), with general composition $[Ag_9CuS_4]^{2+}$. The fast ion conductivity occurs in the latter module layer (Fig. 32). Although no long-range ordering at low temperature could be established for pearceite, this ordering was shown in different samples of polybasite by Evain *et al*. (2006), who evidenced complex polytypism phenomena (i.e., 221 and 222 unit-cell types).

These authors solved and refined the crystal structure of both polybasite-221 (space-group type $P\bar{3}21$; Fig. 33) and polybasite-222 (space-group type *C*2/*c*; Fig. 34) and proposed a possible mechanism regulating the ordering in these minerals.

The crystal structures of the remaining members of the group (i.e., antimonpearceite, arsenpolybasite-221 and -222) were studied at room temperature by Bindi *et al.* (2006b). These authors showed that antimonpearceite possesses the same structural arrangement observed for pearceite and that the polytypism phenomena occurring in different arsenpolybasites (i.e., 221 and 222 unit-cell types) show strong analogies with those observed

in polybasites. The complexity of these minerals can be evidenced by the number of unit-cell types used to describe all the members of the group (Fig. 35).

It was then clear that all the members of the pearceite-polybasite group present the same high-temperature structure and that it is observed at room temperature either in their high temperature (HT) fast ion conductivity form (pearceite) or in one of the low temperature (LT) fully ordered (222), partially ordered (221) or still disordered (111) forms, with transition temperatures slightly above or below room temperature. A detailed investigation of the phase transitions, by means of conductivity and calorimetric studies and *in situ* single-crystal X-ray diffraction experiments, was carried out by Bindi *et al.* (2006b).

Following the determination of the crystal structures for all the members of this group and the elucidation of the conducting mechanism, these minerals were considered as a family of polytypes. Indeed, the solution of the crystal structure allowed also the understanding of the doubling of the unit-cell parameters, that is related to the Ag ordering. In agreement with this deeper knowledge, a revision of the nomenclature was proposed by Bindi *et al*. (2007). The old names antimonpearceite and arsenpolybasite were discredited, whereas the names pearceite and polybasite, previously defined on structural basis (i.e., 111 and 222, respectively), were redefined on chemical basis, with As > Sb for the former and Sb > As for the latter.

If silver is the main driving force responsible for the fast ionic conductivity, copper seems to play an important role in the disorder of particular portions of the structure. Bindi *et al*. (2007) showed that not all the 111 aristotype structures give a long range ordered low-temperature structure. There are indeed Cu-poor pearceite-polybasite minerals that remain trigonal with the 111 cell and $P\bar{3}m1$ space-group type, and intermediate pearceite-polybasite minerals with the 221 cell and $P321$ space-group type. This particularity is to be related to the disorder occurring, whatever the temperature, within the $[(Ag,Cu)_6(As,Sb)_2S_7]^{2-}$ *A* module layer. Indeed, with the lowest (1.54, 1.29, 1.08) and the highest (4.5) Cu content, Bindi *et al*. (2006b) obtained two different fully ordered structures. As the Cu content increases (2.29, 1.69, and 1.55) from the lowest values, 221 compounds with only a partial ordering were observed. For a further increase of the Cu content (3.8) the structure remained disordered (111 cell), whatever the temperature.

In conclusions, the pearceite-polybasite group of minerals can be considered as a series with the same aristotype, fast ion conducting form at high temperature. Depending upon the Cu content, an ordering occurs with transition temperatures related to that content: the lower the Cu content, the higher the transition temperature from the fast ion conducting HT form to the non ion conducting form.

Another interesting mineral structure, which shows similarities with those of the pearceite-polybasite minerals, is that of fettelite, $[Ag_6As_2S_7][Ag_{10}HgAs_2S_8]$. The crystal structure of fettelite (Bindi *et al.* 2009a) consists of an alternation of two kinds of layers along the **c**-axis: layer *A* with general composition $[Ag_6As_2S_7]^{2-}$ and layer *B* with general composition $[Ag_{10}HgAs_2S_8]^{2+}$ (Fig. 36). In this structure, the Ag atoms adopt different coordinations, extending from quasi linear to quasi tetrahedral, the AsS_3 groups form trigonal pyramids as are typically observed in sulfosalts, and Hg links two sulfur atoms in a linear coordination. By means of an integrated high-temperature single-crystal X-ray diffraction (HT-SCXRD), differential scanning calorimetry (DSC), and complex impedance spectroscopy (CIS) study, Bindi and Menchetti (2011) showed that fettelite exhibits a ionic-transition at about 380K toward a disordered phase having a trigonal symmetry with the *a* and *b* unit-cell

parameters halved. In the HT-structure, what induces the disorder in the *B* layer are both Ag and Hg cations, which are found in various sites corresponding to the most pronounced probability density function locations of diffusion-like paths (Fig. 37). So, even if Hg is a minor element in fettelite, it does play a very important role in the stabilization of the disorder. The study by Bindi and Menchetti (2011) indicated that at least two polytypes could exist for fettelite, the ordered, monoclinic RT-structure (space-group type *C*2), and a fast ion conducting, trigonal, disordered HT-form (space-group type $P\bar{3}m1$) with *a* and *b* parameters halved.

4.4.2 Argyrodite-canfieldite series

The minerals of the argyrodite group mainly consist of three members: argyrodite Ag_8GeS_6, canfieldite Ag_8SnS_6, and putzite $(Cu_{4.7}Ag_{3.3})GeS_6$. According to Wang (1978), argyrodite and canfieldite are isostructural (space-group type $Pna2_1$ or *Pnam*), and a solid solution exists between these two minerals. The crystal structure of argyrodite was published by Eulenberger (1977) and that of a tellurian variant of canfieldite was reported by Bindi *et al*. (2012a). Several structural studies on synthetic argyrodite-type compounds have been reported, mainly because such phases are of interest for their manifold structural and physical properties, for example, as electrolytes (e.g., Evain *et al*. 1998; Gaudin *et al*. 2001; Rao and Adams 2011). These compounds undergo three phase transitions: the high-temperature, ionic-conducting phase crystallizes in the space-group type $F\bar{4}3m$ (Fig. 38). The medium-temperature phase has space-group type $P2_13$, and, finally, the low-temperature phase has an apparent space-group type $F\bar{4}3m$, but it actually adopts an orthorhombic symmetry (space-group type: $Pna2_1$, *Pnam* or $Pmn2_1$).

Recently Bindi *et al*. (2017a) reported a heretofore unobserved compound belonging to the argyrodite group, named spryite, exhibiting the ideal formula $Ag_8(As^{3+}_{0.5}As^{5+}_{0.5})S_6$, which represents the first As^{3+}-bearing member of the argyrodite group (Fig. 39). It was found in the Ag- and Mn-rich zone of the Uchucchacua polymetallic deposit, Oyon district, Catajambo, Lima Department, Peru, a complex vein-type deposit related to a dacitic intrusion cutting through Cretaceous and Tertiary formations on the West side of the Occidental Cordillera of Central Andes (Oudin *et al*. 1982). From a structural point of view, spryite is intimately twinned with six twin domains. The most peculiar feature is that arsenic is present in both trivalent and pentavalent state. As^{3+} forms AsS_3 pyramids typical of sulfosalts, (Ge^{4+}, As^{5+}) links four S atoms in a tetrahedral coordination, and Ag occupies sites with coordination ranging from quasi linear to almost tetrahedral connected into a framework (Fig. 40).

Noteworthy, a network of non-interacting Ag cations is established for spryite. This behavior is different with respect to that usually reported for argyrodite-like compounds (Belin *et al*. 2001), which show a strong disorder in the sub-lattice of the moving cations at room temperature. In this light, spryite represents the first argyrodite-type compound which does not behave as a fast ionic conductor. Likely, the presence of As^{3+} inhibits the typical ionic conductivity observed in these compounds. The presence of partially occupied $As^{3+}S_3$ pyramids could indeed hinder the formation of the 'quasi-liquid like' structure of the mobile ions which usually are highly delocalized over the sites available to them. The free energy

associated with the regular sites in spryite is likely higher than that of the interstitial sites, thus making the conduction mechanism highly unfavorable.

5. Structural complexity in sulfosalts and the role of minor constituents

5.1 Introduction

Sulfosalts are an informal group of chalcogenides (Moëlo *et al*. 2008), often characterized by very complex crystal structures. Dittrich *et al*. (2009) reviewed some interesting properties and applications of these minerals. For instance, due to the strong anisotropy of the crystal structures of several sulfosalts, the crystal growth velocities can be severely anisotropic, giving rise to individuals characterized by aspect ratios of more than 1000, with potential application in nanotechnology (Fig. 41). Other interesting applications are in photovoltaics, thermoelectrics, phase change memory, X-ray detectors, and so on.

Sulfosalt crystal structures are sometimes very complex, with large numbers of independent atomic positions and large unit-cell volumes. Actually, these crystal structures can be broken up into relatively simpler fragments ("modules"; see Section 2.2) that are recombined through the action of structure-building operators. Among sulfosalts, a large group is represented by the so-called rod-based sulfosalts. They are represented by Pb/Sb and Pb/Bi sulfosalts whose building principles were worked out by Makovicky (1993, 1997). Their crystal structures can be described as formed by cut outs of basic structures like PbS(NaCl) or SnS; these building units (rods) have generally a lozenge cross-section, are several PbS/SnS subcells wide and two or more atomic layers thick. These building units are then connected and stacked to give rise to three-dimensional structures. Usually, these phases show a distinct partitioning of Sb and Bi within rod interiors, where lone-electron-pair micelles are formed, and of Pb on the rod surfaces. Mixed Pb/(Sb,Bi) positions in the rod interiors can occur, in order to maintain charge balance and minimizing structural distortion. Makovicky (1993) proposed three fundamental categories of rod-based structures, i.e., (i) the layer-, (ii) the chess-board, and (iii) the cyclic category (Fig. 42). The next step in structural complexity was represented by the so-called boxwork structures.

5.2 Boxwork structures

Boxwork structures are the currently known most complex modular category of sulfosalts. This term was first introduced by Makovicky *et al*. (2001) during the description of neyite, a silver-copper sulfobismuthite with formula $Ag_2Cu_6Pb_{25}Bi_{26}S_{68}$. Meanwhile, a series of Pb/Sb oxy-sulfosalts and oxy-chloro-sulfosalts were described by a French-Italian research group of the Nantes and Pisa Universities, showing the same kind of very complex crystal structures (Table 2). These latter authors defined the occurrence of three different kinds of rods, namely rods A, B, and C_1-C_2 (Moëlo *et al*. 2000; Palvadeau *et al*. 2004).Makovicky and Topa (2009) gave a formal definition and a description of the architecture of these complex sulfosalts. A boxwork structure (Fig. 43) can be described as formed by three structural elements:

i) *walls* (= rods C_1-C_2), based on double layers of SnS or more rarely PbS archetype (see Section 2.1). Walls are sinuous and start on one side of the wall and end on the other side. It is worth noting that such a sinuosity can be obtained through the insertion of peculiar structural features, e.g., kermesite-like fragments like in scainiite (Moëlo *et al*. 2000) or an Hg-centered octahedron as in marrucciite (Orlandi *et al*. 2007).

ii) *partitions* (= rods A), usually represented by four-atomic-layers-thick lozenge-shaped rods based on the SnS archetype. Only in marrucciite, partitions based on PbS archetype have been observed. In neyite, the partitions are only two-atomic-layer-thick. The width varies between two and four polyhedra.

iii) *fill elements* (= rods B) are rods of SnS archetype and, less frequently, Pb archetype. The fill element composition varies between MS_4 (where M is a cation) (e.g, in vurroite – Pinto *et al*. 2008) and $M_{18}S_{26}$ for chovanite (Makovicky and Topa 2009; Biagioni and Moëlo 2017).

It is worth noting that such a structural complexity seems to be closely related to the occurrence of minor constituents. In particular, Makovicky and Topa (2009) highlighted the role played by oxygen in generating the so-called "kermesite-like configuration", as first defined by Moëlo *et al*. (2000). Indeed, Makovicky (1993) showed that only a limited number of rod shapes and sizes can be combined forming rod-layer sulfosalts and chessboard-type sulfosalts. The existence of additional new sulfosalts, containing in particular antimony, can be related to the occurrence of this structural feature, similar to that described in the oxy-sulfide kermesite, Sb_2S_2O (e.g., Bonazzi *et al*. 1987), and acting as a structure modifier, favouring the fitting of the structural modules. Kermesite-like configurations observed in scainiite and other lead-antimony oxy-sulfosalts are shown in Figure 44. The most common configuration is represented by the alternation, along the rod extension, of an oxygen atom and a vacancy. Usually, taking into account the strongest bonds for Sb^{3+} and As^{3+} (i.e., those having *Me*–S distance shorter than 2.70 Å), a trigonal pyramidal coordination is typically observed, satisfying the bond-valence requirements. In the kermesite-like configurations, only two short *Me*–S distances are present, and the third bond is represented by *Me*–O bond, with the oxygen atom above or below Sb/As. Clearly, the crystallization of such complex structures is strictly related to peculiar $f(O_2)/f(S_2)$ conditions (e.g., Orlandi *et al*. 1999).

Vurroite and its isotype tazieffite are two other sulfosalts showing a boxwork structure, stabilized by Sn and Cl and Cd and Cl as minor chemical constituents, respectively (Fig. 45). Actually, these minerals can be really considered a masterpiece of structural complexity, showing a very complex crystal structure, an order-disorder[4] (OD) character, and the occurrence of a widespread polysynthetic twinning. The two latter features (OD nature and twinning) are intimately related. On the basis of the characteristic shown by X-ray diffraction patterns, Pinto *et al*. (2008) derived the possible polytypes of vurroite and demonstrated their occurrence in the studied material. The extensive polysynthetic twinning shown by vurroite is related to the OD nature of this mineral. Following the solution of the crystal structure of vurroite, Zelenski *et al*. (2009) reported the structural features of isotypic tazieffite.

The role of minor elements (both cations and anions) in stabilizing complex compounds is exemplified by several sulfosalts having a boxwork structure. For instance, Sn and Cl favours the crystallization of vurroite (Garavelli *et al*. 2005), whereas Cu, Hg, and O are pivotal for the crystallization of rouxelite (Orlandi *et al*. 2005). In this latter mineral, distorted HgS_{2+4} octahedra occur in the walls; this distortion, related to the tendency of Hg^{2+} to form two linear short bonds, favours the insertion of CuS_4 tetrahedra in the crystal structure, adjacent to the walls. In this way, Hg acts as a structure modifier. In addition, in the crystal structure of rouxelite, portions with Sb atoms showing the kermesite-like configuration occur.

5.3 Other zinkenite-related complex sulfosalts

The description of these complex crystal structures using the modular approach developed by Makovicky (1993, 1997) can neglect some strong bonds. Since the first description of lead-antimony sulfosalts by the Nantes-Pisa research group (e.g., Moëlo *et al*. 2000), another type of layer definition was proposed, taking into account the distribution of strong and weak bonds. In this alternative (and in some ways complementary) approach,

[4] Order-disorder structures are formed by one or more kind of layers (not necessarily structural layers) stacked according to two or more geometrically equivalent ways (Ferraris *et al*. 2008 and references therein). An infinite number of different layer sequences are possible, both ordered and disordered. Ordered sequences are known as polytypes, corresponding to Maximum Degree of Order (MDO) sequences.

complex rod layers are defined, their boundaries passing through lone-electron-pair micelles and through interfaces between archetype rods. This description highlights the organization of crystal structures around pseudotrigonal columns (see for instance the crystal structure of chovanite in Figure 43) usually organized around a Pb_6S_{12} triangular core.

This latter structural motif, typical of zinkenite, $Pb_9Sb_{22}S_{42}$ (Biagioni et al. 2018), occurs also in other related phases having crystal structures not belonging to the boxwork group but to the chess-board type. However, their structural complexity is still very relevant. Moëlo *et al*. (2012) reported the crystal structure of two complex Ag-Pb sulfosalts, sterryite and parasterryite, $Cu(Ag,Cu)_3Pb_{19}(Sb,As)_{22}(As_2)S_{56}$ and $Ag_4Pb_{20}(Sb,As)_{24}S_{58}$, respectively. These two minerals, along with ciriottiite, $Cu(Cu,Ag)_3Pb_{19}(Sb,As)_{22}(As_2)S_{56}$ (Bindi *et al*. 2016a), are expanded derivative of owyheeite, $Ag_3Pb_{10}Sb_{11}S_{28}$ (Moëlo *et al*. 1984; Laufek *et al*. 2007), a rare Ag-Pb sulfosalt showing an OD nature (Makovicky and Olsen 2015). Figure 46 shows some structural features of sterryite and parasterryite. Moëlo *et al*. (2012) defined complex columns representing the fundamental building blocks of these compounds, principally considering the surfaces of weakest bonding. In this way, a triangular prismatic core can be distinguished; around this core, two arms of unequal length, indicated as "long" and "short", are organized. It is worth noting that sterryite and parasterryite have the same triangular prismatic core, a very similar long arm, and a $(Sb,As)_2S_4$ group at the basis of the short arm. The similarity index between these two structures, defined as the ratio between the common positions and the total atoms in the formula unit, is close to 90%, being 94/103 in sterryite (94 being the common positions and 103 the total number of atoms) and 94/106 in parasterryite. The difference between these two complex minerals occurs at the end of the short arm (Fig. 46). In particular, sterryite (Fig. 46a) shows a partially occupied Cu site and an As–As pair (Fig. 46b and c), with As–As distance of 2.63 Å, comparable with those observed in realgar As_4S_4 (2.566 Å – Mullen and Nowacki 1972) and in wakabayashilite (2.656 Å – Bonazzi *et al*. 2005). In parasterryite, the short arm is Ag-rich, with four Ag sites (Fig. 46d and e). It is interesting to observe that this chemical difference of two small structural fragments connected to topologically identical complex columns has a relevant consequence on the general organization of the crystal structures of sterryite and parasterryite, resulting in two different choices corresponding to the $P2_1/n$ and $P2_1/c$ settings of the space group, respectively.

Still more complex is the crystal structure of meerschautite, $Ag_{5.5}Pb_{42.4}Sb_{45.1}S_{112}O_{0.8}$, based on two different complex columns (Biagioni *et al*. 2016). This mineral differs from sterryite and parasterryite for the space group symmetry, $P2_1$, and for the configuration of the short arms connecting successive pseudotrigonal columns (Fig. 47). One of these arms is Ag-rich (Fig. 47a and b), whereas the other displays localized Sb–O–Sb bonds, in a kermesite-like configuration (Fig. 47c and d). Meerschautite is the lead-antimony sulfosalt with the largest unit-cell content (more than 200 atom positions) showing only one O specific position (Biagioni *et al*. 2016). A mineral that is likely structurally related to sterryite, parasterryite, and meerschautite is tubulite, $Ag_2Pb_{22}Sb_{20}S_{53}$ (Moëlo *et al*. 2013). What is interesting is the tubular morphology characterizing several samples of this mineral, like those shown in Fig. 41 for robinsonite. The origin of this unusual morphology is probably due to extrinsic factors, related to the crystallization environment and likely acting on extremely thin lath-like individuals at the early stages of crystal growth.

5.4 Information-based complexity in sulfosalts

A quantitative estimation of the structural complexity of these sulfosalts can be achieved using the method recently proposed by Krivovichev (2013a) and based on the information contents of their crystal structures. Table 3 gives the information-based complexity parameters for the sulfosalts here discussed.

Sulfosalts having a boxwork structure have usually structural information complexities ${}^{str}I_{G,total}$ in the range 500 – 1000 bits/cell, thus being classifiable as "complex", according to Krivovichev (2013a). Two of them, marrucciite and pillaite, could seem to be not so complex, having ${}^{str}I_{G,total}$ of ~450 and 480 bits/cell, respectively, corresponding to an intermediate complexity. Actually, this apparently relatively low complexity is due to the fact that the calculations given in Table 3 have been usually performed on the 4 Å sub-structure of boxwork structures. The superstructure reflections doubling the 4 Å periodicity are usually very weak and in several cases it was not possible to refine the actual 8 Å structure. This point is particularly important, as exemplified by chovanite, the mineral showing the largest infill elements currently known (Makovicky and Topa 2009; Biagioni and Moëlo 2017). Indeed, the ${}^{str}I_{G,total}$ of the 4 Å sub-structure is ~ 800 bits/cell, and consequently this mineral could be considered as "complex". However, when the real 8 Å structure is taken into account, a definitely higher ${}^{str}I_{G,total}$ value is obtained, 3753 bits/cell, agreeing with the very complex nature of this compound. Similarly, the chess-board structures of sterryite, parasterryite, and meerschautite, with ${}^{str}I_{G,total}$ in the range 2800 – 3200 bits/cell, can be considered "very complex". It is interesting to observe that the pair vurroite/tazieffite, whose studies faced up to a series of complicated crystallographic issues, has a ${}^{str}I_{G,total}$ value lower than those shown by other phases. Indeed, the structural information complexity index ${}^{str}I_{G,total}$ takes into account only the amount of information contained in a mineral species, whereas it neglects other factors like OD phenomena, twinning, and modulation, which represent a different kind of complexity that, in some cases, may preclude the full understanding of the actual structural information hosted within a crystal structure.

5.5 Role of minor constituents

Sulfosalts characterized by boxwork structures and other very complex Ag-Pb sulfosalts (e.g., sterryite, parasterryite, and meerschautite) reveal that in the crystallization of such very complicated phases a key role is played by minor components, both cations and anions. The crystal structure solution and refinement of these minerals increase our understanding of the role of minor constituents, with potential implications in the synthesis of peculiar technological compounds.

Minor constituents could also give rise to incommensurate structures. In the sulfosalt realm, a simple example is represented by meneghinite, $CuPb_{13}Sb_7S_{24}$ (Fig. 48). Euler and Hellner (1960) and Hicks and Nuffield (1978) interpreted additional weak reflections in the single-crystal X-ray diffraction patterns as due to a commensurate superstructure. Recently, Bindi *et al*. (2017b), using a sample from the Bottino mine (Tuscany, Italy), where this mineral was originally described in the XIX Century, clearly observed a small (but detectable) departure of the position of the additional reflections, apparently doubling a 4 Å periodicity, from the commensurate value 0.5. The crystal structure of meneghinite has been consequently solved and refined as an incommensurate structure in a four-dimensional superspace (see Section 6.2), describing the modulation of occupancy of Cu, Pb, and Sb atoms, related to the substitution mechanism $Cu^{+} + Pb^{2+} = \square + Sb^{3+}$. The small departure from the commensurate structure suggests that other commensurate superstructures observed in complex sulfosalts could be due, in some cases, to some kinds of incommensurate chemical modulation.

Indeed, until now, classical examples of incommensurability in sulfosalts are represented by members of the cylindrite homologous series (e.g., Makovicky and Hyde 1992). This is a peculiar kind of incommensurability related to the occurrence of a pseudotetragonal *Q* layer, two to four atoms thick and with a PbS archetype, and a pseudohexagonal *H* layer of CdI_2-type or NbS_2/TaS_2-type. The misfit between these two kinds of layers is at the origin of the incommensurate nature of this group of minerals. A recent and spectacular example is merelaniite, $Mo_4Pb_4VSbS_{15}$ (Jaszczak *et al*. 2016 – Fig. 49). The

tubular morphology of these minerals is due to intrinsic factors. Indeed, the nucleation of crystals of cylindrite homologues starting from a pair of *Q* and *H* layers can induce a curvature of the constitutive layers, resulting in a macroscopic cylindrical crystal.

Incommensurate modulated and composite structures are a peculiar kind of aperiodic structures, as will be discussed in the next chapter.

6. Aperiodic minerals

6.1 Introduction

Aperiodicity in minerals refer to the aperiodic nature of their crystal structures. Since the 1970s, we have learned that crystal structures do not necessarily obey the classical concept of three-dimensional periodicity of their atomic arrangements. First, *incommensurately modulated* structures were observed, followed by another family of structures called *composites* and finally, *quasicrystals* were discovered. These three types of complex structures are currently referred by the generic term of *aperiodic structures*. They all share in common the property that their diffraction patterns are essentially discrete but cannot be fully indexed with the usual triplets of *hkl* integers as is the case for the classical model of crystals. The discrete nature of diffraction pattern is a consequence of the long-range order of the corresponding crystal structures but the fact that three integers do not suffice any more is a consequence of a new type of order which will be presented in this section.

It is interesting to note here the important role played by the study of mineral structures to the historical development of the concept of aperiodicity in crystals. Mineral structures of *calaverites*, *natrites* or *labradorites* for example were fundamental for the theoretical development of aperiodicity (see below).

Before describing a few interesting aperiodic mineral structures, a brief description of the basic concepts used to characterize them will be presented. For a deeper understanding of the subject, the interested reader may refer to the dedicated literature (e.g., van Smaalen 2012, Janssen et al. 2018).

Due to space limitations, examples of the third category of aperiodic minerals, namely composites, will not be presented here. Their structures have been shortly presented in Section 5.5 and appear essentially in two different families, layered and columnar. In the first case, two or more layers with their own periodicities are stacked periodically in the third dimension. In the second case, different columns with their own periodicities form two dimensional periodic arrays. The world of natural minerals is also very rich in incommensurate examples of composites. The interested users may consult the pioneering works of Makovicky and Hyde (1981, 1992) to discover additional interesting examples of aperiodic minerals.

6.2 Short theoretical presentation

Any conventional crystal structure can be described by the individual positions of each atom contained in its unit cell characterised by the three lattice vectors $\mathbf{a}_1$, $\mathbf{a}_2$, $\mathbf{a}_3$ and the three angles α_1, α_2, α_3. The determination of the lattice constants is usually performed by diffraction methods (X-rays, neutron, electron) and therefore it is convenient to introduce the reciprocal lattice vectors $\mathbf{a}_i^*$ where the scalar product satisfies the conditions

$$\mathbf{a}_i \cdot \mathbf{a}_j^* = \delta_{ij} \qquad (1)$$

Here δ_{ij} is the Kronecker symbol, which is 1 if $i=j$ and 0 if $i \neq j$.

Diffraction patterns of classical crystals are usually analysed in terms of the reciprocal lattice vectors with basis $\mathbf{a}_1^*$, $\mathbf{a}_2^*$and $\mathbf{a}_3^*$ by assigning each discrete diffracted intensity to a

reciprocal lattice node which is uniquely characterised by the three integers *hkl* mentioned before. Once the full set of diffracted intensities is measured, it is in principle straightforward to obtain the positions of each atom contained in the unit cell.

Let us analyse the following reciprocal lattice layer of diffracted intensities of the mineral natrite (Dušek et al. 2003; Arakcheeva and Chapuis 2005; Arakcheeva et al. 2010) illustrated in Figure 50.

It is obvious in this layer that the full set of reflections cannot be characterized in terms of only two indices *h* and *l*. The additional reflections lay on parallel lines and are equidistantly distributed on both side of each node *h2l*. It is convenient to define an additional vector **q** expressed in terms of the reciprocal vectors $\mathbf{a}_i$:

$$\mathbf{q} = \alpha_1 \mathbf{a}_1^* + \alpha_2 \mathbf{a}_2^* + \alpha_3 \mathbf{a}_3^* \qquad (2)$$

In the specific case, two coefficients α_1 and α_3, are irrational and $\alpha_2 = 0$. In the general case, we can define a set **H** of lattice vectors to describe the full set of diffraction reflections:

$$\mathbf{H} = h_1 \mathbf{a}_1^* + h_2 \mathbf{a}_2^* + h_3 \mathbf{a}_3^* + m\mathbf{q} \qquad (3)$$

Here the integer coefficients h_i instead of the equivalent triplet *hkl* are used. If the integer $m = 0$, **H** describes a *main* reflection whereas if $m \neq 0$, **H** describes a *satellite* reflection.

We are thus faced with the necessity to increase the number of vectors in reciprocal space and consequently its dimensionality in order to characterize the full set of reflections. This can be done according to the following embedding given in Figure 51.

The new space embedding to describe the full set of reciprocal vectors is called superspace and in our particular case, we introduce the four new basis vectors $\mathbf{a}_{S1}^*, \ldots, \mathbf{a}_{S4}^*$ expressed in terms of their external and internal components. Once the reciprocal vectors are defined, we can use the orthogonality relation to obtain the corresponding direct space basis vectors given in the next relation.

$$\left.\begin{array}{rcl} \mathbf{a}_{S1}^* &=& (\mathbf{a}_1^*, 0) \\ \mathbf{a}_{S2}^* &=& (\mathbf{a}_2^*, 0) \\ \mathbf{a}_{S3}^* &=& (\mathbf{a}_3^*, 0) \\ \mathbf{a}_{S4}^* &=& (\mathbf{q}, 1) \end{array}\right\} \rightarrow \mathbf{a}_{Si} \cdot \mathbf{a}_{Sj}^* = \delta_{ij} \rightarrow \left\{\begin{array}{rcl} \mathbf{a}_{S1} &=& (\mathbf{a}_1, -\mathbf{q} \cdot \mathbf{a}_1) \\ \mathbf{a}_{S2} &=& (\mathbf{a}_2, -\mathbf{q} \cdot \mathbf{a}_2) \\ \mathbf{a}_{S3} &=& (\mathbf{a}_3, -\mathbf{q} \cdot \mathbf{a}_3) \\ \mathbf{a}_{S4} &=& (\mathbf{0}, 1) \end{array}\right. \qquad (4)$$

The next challenge is to find a suitable embedding of the three-dimensional structure into superspace and a way to reinterpret crystal structures in this new reference frame.

The origin of the satellite reflections observed on diffraction patterns was already known long before the 1970s. However, Korekawa (1967) was the first to present some theoretical backgrounds explaining the origin of the satellite reflections in “labradorite” and other minerals. Their structures were interpreted as periodic displacement of atoms with an additional periodicity, different from the three unit-cell lattice constants. Any periodic perturbation can be represented by a series of Fourier terms and this is specifically what is used to represent the displacements we are referring to.

Let us reinterpret a structure in superspace with the simplest possible displacement or *modulation* function, i.e., a sinusoidal displacement as represented in Figure 52a. The description of the structure in superspace can be thus analysed in terms of two-dimensional sections just like architect’s plans of a complex building are analysed in terms of 2-d sections. Practically, a limited amount of sections is sufficient to fully characterize the structure. From Figure 52b we can see that the real crystal structure is not analysed in terms of the natural

variable x_4 but rather by the variable t which is related to x_4 by the relation $t = x_4$-**q**·**r.** For the specific case of natrite, it turns out that only four reciprocal basis vectors are necessary to fully characterize the diffraction pattern with integer coefficients. In general, this is not always the case and examples of structures with up to six reciprocal basis vectors have been found. This is for example the case for icosahedral quasicrystals. The number of reciprocal basis vectors necessary to fully characterize the structure is called the *rank*. Therefore, if the rank is equal to the dimension of the periodic object, the structure is *periodic.* Otherwise, if the rank is larger than the dimension, the structure is *aperiodic*.

As in periodic structures, the resolution of aperiodic crystal structures consists of determining the electron density (if X-ray are used) from the structure factors by Fourier transform. For a structure with rank 4, described in (3+1)D superspace, the structure factor $F(\mathbf{H})$ is given by the relation:

$$\begin{aligned} F(\mathbf{H}) &= \sum_j f_j(\mathbf{H}) \exp(2\pi \mathrm{i} \mathbf{H} \cdot \mathbf{r}_j) \\ &\quad \times \int_0^1 \mathrm{d}t \; p_j(t) \exp\{2\pi \mathrm{i}(\mathbf{H} \cdot \mathbf{u}_j(t) + h_4 t)\} \end{aligned} \tag{5}$$

On the first line we recognise the classical part of the structure factor with the atomic scattering factors f_j whereas the second line is dedicated to the modulated part of the structure which is characterize by the functions $\mathbf{u}_j(t)$, for each atom in the unit cell. As mentioned before, the variable t is more convenient for the analysis of the geometrical characteristics between atoms and is favoured instead of x_4. The probability factor $p_j(t)$ allows to characterise structures with *substitution modulations* or defects.

More complex modulation functions $\mathbf{u}_j(t)$ can obviously be obtained by adding a series of harmonic terms to optimize the best fitting function. Other possibilities however have been proposed like crenel or step-like, sawtooth and zigzag functions (Petříček *et al*. 2014). An important ingredient for the description of crystal structures concern the space group symmetry used to characterize periodic structures. For aperiodic structures, however a generalization of the symmetry concept has been introduced in order to fully describe them, the so-called superspace groups. This is not our intention to deal here with the theoretical basis of superspace symmetry. Bibliographic references may be found in Janssen et al. (2008) and van Smaalen et al. (2013).

One may wonder what kind of structure solutions methods can be applied to solve aperiodic structures. Fortunately, some efficient and recently developed algorithms have been designed (see for instance Oszlányi and Sütő 2004; Palatinus and Chapuis, 2007) to solve any type of structures in any dimension perhaps with some caveat on macromolecular structures. These methods are based on *dual space phase retrieval algorithms*. They are iterative methods which attempt to estimate the phases of the structure factors (reciprocal space) by forcing them to satisfy the conditions that the atomic density of the structure (direct space) cannot be negative. The program package JANA2006 (Petříček et al. 2014) is a very efficient tool to solve and refine both periodic and aperiodic structures in any dimension.

Finally, we can conclude this paragraph by giving some specific characteristics about possible aperiodic structures. In our introduction, we have enumerated the three main families of aperiodic structures which have been identified, namely the incommensurately modulated structures, the composites and the quasicrystals. According to Yamamoto (1996), the best way to distinguish the categories is to look at their diffraction patterns which are schematically represented in Figure 53. In modulated structures, we can always distinguish a series of main reflections along the external space dimension R_e and in addition a series of satellites with embedding along the internal space dimension R_i. In composites, we can always distinguish two or more series of main reflections and in addition satellites may also occur. In

quasicrystals however, the distinction between main and satellite reflections can no longer be made and the important reflections have no periodicities. Quasicrystals can always be clearly distinguished whereas we can find limiting cases where the distinction between modulated and composite crystal is not clear cut.

In the next paragraphs, we shall present a few characteristic aperiodic mineral structures and illustrate their specific properties.

6.3 Natrite, Na_2CO_3

As mentioned earlier, natrite was at the origin of a new revolution of the concept of crystals. The first hints aroused when de Wolff and his group (Brouns et al. 1964) realised that they could not fully index its powder diffraction pattern. The solution of the problem was found a decade later when van Aalst et al. (1976) proposed for the first time the embedding of the diffraction pattern in higher dimensional space. In addition, they introduced the concept of high-dimensional symmetry of modulated structures and proposed a structural model of Na_2CO_3 in the harmonic approximation. Shortly following this paper, the concept of superspace symmetry was introduced by de Wolff et al. (1981).

We have to mention at this point that many publications prior to de Wolff's work were published pointing to the existence of modulated structures in various systems. Unfortunately, these studies proposed *ad hoc* structural solutions but failed to develop a valid concept to generalize the symmetry properties which is a prerequisite for any structural studies. The work initiated by the Dutch groups was the trigger which started the rapid development of the new structural paradigm.

Coming back to the structure of natrite, we should mention here that most of the structural studies performed have been done on synthetic samples (Dušek et al., 2003; Arakcheeva and Chapuis 2005). A study by Arakcheeva et al. (2010) comparing natural natrites and synthetic Na_2CO_3 shows very similar structures with some minor discrepancies in the phase transition temperatures which can easily be explained by various impurities always present in natural samples.

Na_2CO_3 exhibits numerous phases depending on the temperatures (Dušek et al. 2003; Arakcheeva and Chapuis 2005) which are schematically indicated below.

α	$754K$	β	$605K$	γ'	$530K$	γ	$170K$	δ
$hexagonal$		$monoclinic$		$monoclinic$ $incom.$		$monoclinic$ $incom.$		$monoclinic$ $lockin$

The structure of γ-Na_2CO_3 is best described in terms of graphite-like layers formed by $Na3^+$ and CO_3^{2-} ions as illustrated in Figure 54. Na1 and Na2 are located between the layers. Both are coordinated by 6 oxygens forming octahedra. For Na3 however, the octahedra are strongly distorted. The Na1,2–O distances vary between 2.3 and 2.4Å whereas for Na3–O the distances vary between 2.5 and 2.9 Å. In all the phases, the distinction between the two Na1,2 and Na3 can always be observed and although they are the same atomic species they behave like two stereo-chemically distinct groups of atoms.

In order to understand the nature of the incommensurate character of γ-Na_2CO_3, let us analyse this structure in terms of Na and C containing planes illustrated in Figure 55 and neglect the oxygen atoms. In the inset, we can distinguish two types of planes, namely m_M and m_v. The m_M plane is the monoclinic (*a*, *c*) plane which can be also seen in Figure 54. The other m_V planes are rotated by ±60° along the direction of the hexagonal channels.

The atomic arrangement of both m_M and m_V planes are identical in the high-temperature hexagonal phase α. At T ≤ 754 K, the m_M plane and the corresponding configuration remains stable and unchanged in all the lower-temperature phases including the incommensurate ones.

The atomic arrangement observed in the m_V planes attempts to remain identical to the m_M plane but the monoclinic distortion does not allow it. By decreasing temperature from 754 K down to 605 K, the distortion of the m_V plane increases in the β phase until it transforms into the incommensurate γ phase. In the γ phase, the atomic arrangement of the m_V plane is a compromise of a sequence of different configurations observed in the β phase at different temperatures (Fig. 55). This is at the origin of the incommensurability of the γ phase.

It is important to note here the origin of the driving force in the sequence of phases observed in this compound which is also valid for the incommensurate phase. It is not the interactions of sodium with its first coordination sphere, i.e., O atoms, but it is the interactions with sodium with its second coordination sphere consisting of Na and C atoms as shown in the study by Arakcheeva and Chapuis (2005).

We can follow the evolution of the sequence of phases by focusing on the Na atoms in the vicinity of the C atoms, which gives the following coordination scheme while limiting the C···Na contacts to 3.1Å

$Phase$	α	β	γ'	γ	δ
CN	3	4	5	$6-7$	7

The intra layers contact distances between of C and Na3 atoms remain practically unchanged over the temperature range. Thus, the increase of coordination number is essentially due to the Na1,2 channel atoms. None of them participate in the coordination sphere in phase α whereas all of them are bonded in the lock-in phase δ.

It should be mentioned that a detailed study of structure modulations in natural natrites from different origins (Arakcheeva et al. 2010) gives valuable information on the history of the mineral transformation as a function of their occurrences.

6.4 Calaverite $Au_{1-x}Ag_xTe_2$

Calaverite, a mineral with the composition of $Au_{1-x}Ag_xTe_2$, where $0 \leq x \leq 0.15$ is an important gold-bearing ore and another interesting case of a modulated structure which has first challenged mineralogists and later structural scientists until its secret could be uncovered. Already in the beginning of the 20th century, before the diffraction method was discovered, the attempts by mineralogists to index the faces of calaverite according to Haüy's law of rational indices failed. After many attempts to solve this puzzle, an important study was published by Goldschmidt et al. (1931) presenting an extended analysis of 105 different calaverite samples originated from all over the world and identified 92 different crystal forms. The conclusion of their work was that the law of rational indices was not of general validity. They were obviously right but the tools to solve the problem were not ready yet.

The resolution of the incommensurate structures of calaverite by Schutte and de Boer (1988) based on the full set of diffracted intensities including satellite reflections was fundamental to understand the origin of its incommensurability.

The average structure of calaverite solved by neglecting the satellite reflection is illustrated in Figure 56a. It consists of a series of parallel layers of edge sharing Te octahedra centred by (Au,Ag) atoms. The geometrical properties of the incommensurate structure can best be explained in terms of a *t*-plot as introduced in Figure 52. The distance *t*-plot illustrated in Figure 56b gives all the (Au,Ag)-Te < 3.3 Å distances. Note that *t*-plots conveniently summarize all the possible configurations which exist in the crystal but do not include information about orientation and position of the other atoms located in the extended neighborhood.

The analysis of the *t*-plot indicates that for $t \approx ¼$ and ¾ (Au,Ag) is surrounded by only four close Te atoms with (Au,Ag)-Te distances of about 2.7 Å (numbers 1,2,3,4 and 1,2,5,6,

respectively, Fig. 56b). Two other distances of 3.2 Å are too long to take part in the coordination sphere. Knowing that the corresponding *t*-plot of the angles are close to 90°, we can conclude that somewhere in the crystal space, we shall find square planar $(Au,Ag)Te_4$ configurations with the coordination number CN = 4 for (Au,Ag). Other *t*-intervals can be characterized with CN = 4 + 2. For a deeper analysis of the properties of the structure, we need to represent a portion of the modulated structure with many basic unit cells.

Figure 57 shows a portion of the $Au_{0.9}Ag_{0.1}Te_2$ structure with ordered distribution of Ag (Bindi et al. 2009b). The blue circles indicate sites where Ag replaces some of the Au atoms in the octahedra with CN = 4+2. The remaining octahedra contain only Au. Schutte and de Boer (1988) proposed that the origin of the modulation in calaverite was due to the presence of Au^{1+} and Au^{3+} with the electronic configuration $5d^{10}$ respectively $5d^8$, since Au^{3+} prefers a square planar coordination with Te. However, X-ray absorption spectroscopy experiments reported by Ettema et al. (1994) unequivocally shows only Au^{1+} in calaverites. This conclusion is confirmed by a comprehensive structural study by Bindi et al. (2009b) with examples from a series of calaverites with different Ag compositions $0 \leq x \leq 0.33$. The modulation of the oxidation state of Au has also been estimated between 0.9 and 1. This study has demonstrated that the Ag distribution on the Au position plays a key role in the structure formation. The ordered distribution of silver reinforces the valence fluctuation of Au and the structure modulation. A random distribution of Ag suppresses the valence fluctuation of Au and, therefore, their structural modulations. Apparently, natural samples can be found with the same composition but with both types of Ag ordering, which is not surprising considering the various growth conditions of the minerals.

Calaverite is a member of a more general family of pseudo-binary system $Au_{1-x}Ag_xTe_2$ with a silver content up to x=0.5. In the mineral krennerite, the silver content varies between $0.2 \leq x \leq 0.28$. The mineral sylvanite exists in two forms: one with $x = 0.5$ and the second with x slightly smaller than 0.5. It is interesting to note that the superspace model applied to calaverite is able to reproduce the complete set of structures of the pseudo-binary system by adapting the modulation vector **q** with commensurate or incommensurate components and adjusting the *t*-plot of the variable x.

Finally, we would like to conclude this paragraph by returning back to the famous conclusion of Goldschmidt et al. (1931) about the impossibility of indexing the faces and the rejection of the law of rational indices. Shortly after the resolution of the incommensurate structure of calaverite, Janner and Dam (1989) managed to unambiguously index all the possible faces identified in the 1931 paper. The solution was to use four indices for each face, i.e, a number equal to the rank of the structure as previously defined. Figure 58 illustrates the indexation of the faces. Janner and Dam (1989) could identify two twin samples and moreover, from the measurements of Goldschmidt et al. (1931), they could deduce the exact components of the modulation vector **q** up to a precision comparable to that obtained by the X-ray diffraction measurements!

The example of calaverite is by no means an exception and other examples have been found in metal-organic materials where the temperature dependence of the modulation vectors could be deduced from the observations of the crystal forms (Dam and Janner 1986).

Haüy's law is thus still valid provided that we extend the number of indices to the rank of the structure.

6.5 Melilite $(Ca,Na)_2(Mg,Fe^{2+},Al)[(Al,Si)SiO_7]$

The group of melilite minerals include generally solid solution of åkermanite and gehlenite with chemical composition $Ca_2MgSi_2O_7$ and $Ca_2Al(AlSiO_7)$, respectively. The overall formula can be expressed as $X_2T1T2_2O_7$ with T1 and T2 atom species tetrahedrally coordinated by oxygens. The basic structural features of the mineral family have been known

since the 1930s but the incommensurability was discovered much later by Hemingway et al. (1986).

The structure of melilite consists essentially of corner sharing tetrahedra layers alternating with X containing layers as represented in Figure 59. The T2 tetrahedra always appear in pairs forming bow-tie whereas the T1 tetrahedra are linked to four T2 tetrahedra. Each layer consists of irregular pentagonal rings surrounded by two T1 and three T2 tetrahedra. The X atoms are located between the tetrahedra layers and are linked to the oxygens of the nearest layers.

It is clear that this structure allows a large degree of freedom to accommodate many different chemical substitutions for the T1, T2 and X cations. The tetrahedral layers can easily accommodate different T cations with variable size by permitting rotational and translational displacements.

Since the discovery of the incommensurate nature of some melilite structures, many structural studies appeared with various compositions and temperatures. A selection of references can be found in Bindi et al. (2001). The incommensurate structures have been solved in (3+2)D superspace group with tetragonal symmetry. The origin of the incommensurability is essentially due to positional rather than substitutional changes. The coordination of the X cations by O atoms within a single incommensurate structure may vary between 6 and 8 and a flattening of the T1 tetrahedra may also occur. Occupational modulation wave has also been observed in some cases pointing to ordered distribution of some cations. Superstructures which can also be interpreted as *commensurately* modulated structures have also been observed.

The resolution of a natural incommensurately modulated melilite sample from Umbria (Italy) presented here was published by Bindi et al. (2001). Only first order satellites were observed. A portion of the incommensurate layer structure is presented in Figure 60a. A close analysis of the pentagonal rings mentioned above shows a large variation of deformation extending in the layer plane. The most important feature of the deformation can best be understood in terms of the T1-X coordination sphere as represented in the *t*-plot of Figure 60b. Here we concentrate on the X neighbourhood of T1. We can essentially distinguish two zones, one in the vicinity of $t = ½$ and one in the vicinity of $t = 0$ or 1. Close to $t = ½$ T1 has 8 X neighbours with distances up to 4 Å located approximately on the vertices of a cube (see inset). Close to $t = 0$ or 1, T1 has only four X neighbours forming a tetrahedron. Figure 60a illustrates another feature of the structure based on the X-O coordination polyhedra. In the average structure of melilite they are slightly distorted trigonal prism with 6 oxygens. In the incommensurate structure, we observe that the 6-coordinated X atoms form clusters with four long T1–X distances surrounding the T1 tetrahedra indicated on Figure 60a by black tetrahedra. The clusters are regularly located on various circles with 8 members which recalls to some extent similar distributions in quasicrystals! The small 8-membered ring has also been observed in a synthetic $Ca_2CoSi_2O_7$ (Riester et al. 2000) by X-ray diffraction and in $Ca_2ZnGe_2O_7$ (van Heurck et al. 1992) by electron microscopy.

The X-O polyhedra deformation is certainly not the only distortion observed in melilite. The T1–O distances and O–T1–O angles are also affected according to various *t*-plot calculations. The departure from the ideal angle of 109° may vary between 103 and 123°.

Here again as in the other mineral structures presented above, we can find a common justification for the origin of the incommensurability. In melilite, the presence of impurities and the relative size of the X and T cations create disparities in the coordination polyhedra. The ideal 6 coordinated X-O polyhedra can only be accommodated locally, however not stochastically but in a very ordered way in the form of various circular distributions as indicated on Figure 60a.

6.6 Natural Quasicrystals

The discovery of synthetic quasicrystals by Shechtman et al. (1984) extended further the concept of aperiodicity in crystals beyond incommensurately modulated and composites structures. Following this discovery, a large number of Al ternary alloys with quasicrystalline structures could be produced and analyzed by diffraction methods. Two families of quasicrystals essentially emerged in these studies, namely icosahedral and decagonal quasicrystals. During that period, it appeared however that the world of mineralogy would remain exempt of *natural* quasicrystalline materials. The situation changed a quarter of a century later when Bindi et al. (2009c) discovered the first naturally occurring sample of a quasicrystal. The discovery did not occur by serendipity but following not only a systematic analysis of all metallic alloys which could be found in structural databases but also by analyzing various notable mineral collections (Bindi 2020). Finally, the search focused around the mineral kathyrkite $(Cu,Zn)Al_2$ originating from the Koryak Mountains in the northeast of the Kamchatka Peninsula in Russia. From a sample size of sub-μm, the authors could locate an area which did produce the characteristic diffraction pattern with ten-fold symmetry illustrated in Figure 61a obtained by HRTEM. The chemical analysis of the sample yielded the composition $Al_{63}Cu_{24}Fe_{13}$, which is very close to the already known synthetic face-centered icosahedral phase (FCI). In addition to the ten-fold symmetry pattern, the authors could also locate the six- and two-fold patterns at angles corresponding to the FCI pattern. Another convincing argument of the icosahedral symmetry of the sample is given in Figure 61b. The plot lists the intensity weighted $|\Delta|$ where Δ is the absolute deviation of each scattering vector **H** from the nearest matching FCI peak versus the intensity-weighted average of **H**. The center grey zone corresponds to a large number of classical structures extracted from the ICDD database whereas the symbols ❾ and ○ represent well identified QC structures. The vertical and horizontal dotted lines represent 1σ confidence intervals. It is thus clear that the mineral (▲) confirms the nature of its QC structure.

The natural QC mineral was subsequently given the official name *icosahedrite* (Bindi et al. 2011) and a further analysis (Bindi et al. 2012b) gave evidence of the extraterrestrial origin of the sample. The formation of the sample was estimated to be approximately 4.5 Gya under extreme conditions, i.e., shock pressures ≥ 10 GPa and temperatures ≥ 1500 K. The meteoritic origin of stable QC forms is thus clearly demonstrated.

The analysis of the famous kathyrkite sample reserved another surprise, namely the discovery of a decagonal quasicrystalline phase (Bindi et al. 2015) with composition $Al_{71}Ni_{24}Fe_5$. This chemical composition has also been observed in synthetic samples. Decagonal quasicrystals with rank = 5 can be described by a periodic stacking of quasicrystalline layers. Thus, contrary to the icosahedral QC, only ten-and two-fold symmetry diffraction pattern can be observed but no six-fold symmetry.

Yet, the kathyrkite sample delivered a third quasicrystalline phase with the chemical composition $Al_{62}Cu_{21}Fe_7$ (Bindi et al. 2016b). Contrary to the previously discovered natural QC, this new icosahedral phase did not have any synthetic equivalent and its composition seemed to be outside the previously expected equilibrium stability field under standard pressure. Noteworthy, the synthetic analogue of natural $Al_{62}Cu_{21}Fe_7$ was recently obtained by a collision experiment simulating the impact between asteroids in outer space (Hu et al. 2020).

Synthetic QC often exhibits so-called *phason strains*. Phason strains are elastic modes which diffuse in the structure and often relax. They cause systematic shift of the Bragg reflections and the shifts from the ideal positions are inversely related to the intensity of the peak. They are usually observed on samples subject to rapid quenching during the synthesis. It appears that the two natural QC crystalline samples described here are exempt of phason strains and thus depart significantly from synthetic samples formed under strictly controlled

laboratory conditions (Bindi and Stanley 2020). This feature gives also an important indicator about the long-term stability of natural QC phases.

6.7 The puzzle of "labradorite"

The variety of anorthite known as "labradorite" is notable for the iridescent effect observed on some specimens as illustrated in Figure 62a. It belongs to the family of the plagioclase feldspars with composition $Ca_xNa_{1-x}Al_{1+x}Si_{3-x}O_8$ which form solid solution with the two end members *albite* ($NaAlSi_3O_8$) and *anorthite* ($CaAl_2Si_2O_8$).

Plagioclase feldspars can be considered as an important diagnostic tool for petrological studies. The nearly continuous composition variable x is at the origin of structural complexities which have filled many volumes of studies dedicated to a better understanding of their structures. The observation of superstructures, diffuse scattering and the presence of satellite reflections in the diffraction patterns have been the subject of many interesting model proposals since more than 60-70 years. Korekawa and Jagodzinski (1967) were the first to report the observation of two types of satellite reflections relating to two scale lengths in the diffraction patterns of labradorite with an anorthite content of 52%. One series of satellites (called e-satellites) is associated with a modulation periodicity of 50 Å and the other series (s-satellites) is associated with another type of modulation with a much larger periodicity and which is related to the iridescent (or schiller) effect (Fig. 62b). The periodicity of the violet color is approximately 1800±200 Å and 1400±200 Å for the ultraviolet.

A more recent publication by Boysen and Kek (2015) attempts to propose an improved model of labradorite on the basis of X-ray synchrotron radiation data. The tentative schematic model illustrated in Figure 63 gives an interpretation of the origin of the two scale lengths. The large domains D1 and D2 exhibit anorthite content differences of up to 10% and are related to the modulation given by the s-satellites. Within each domain D_i, we observe another modulation sequence related to the e-satellites. The origin of this modulation is also due to variations of the Na/Ca content but the role of the Si/Al distribution is not clarified.

It is surprising that a complete and satisfactory structure solution has not yet been proposed despite the numerous studies on the problem published up to these days (Jin and Xu 2017). The difficulty lies in finding a single structural model which is capable of handling simultaneously both types of modulations with two independent and very different length scales. This would solve the problem of existing correlations with the different Ca/Na and Si/Al contents in different domains and which are completely neglected if the structure solution neglects one or the other type of satellite. Another difficulty resides in the accurate measurements of very narrow and weak satellite reflections even on current synchrotron facilities. It is thus probable that a definitive solution of the structure of labradorite will possibly emerge from a new refinement in a (3+2)D structure model, i.e., with rank 5 instead of rank 4.

6.8 When "disorder" turns out in aperiodicity

The analysis of aperiodic crystal structures often reveals very subtle atomic interactions which are difficult to detect with classical structures. This is not only valid for minerals but for any aperiodic structure. Another interesting aspect is that a single atomic species may occur in the same structure with different crystal-chemical environments and different valence states giving clues on its electronic state. This is the case for instance of Na in natrite and Au in calaverite.

It turns out that the usefulness of the tools which have been developed for the analysis and solution of aperiodic structures (Petříček et al. 2014) goes much beyond these goals. They also have been useful for the prediction and design of new structures. They are also helpful in discovering new relations between various structures as in the case of scheelite (Arakcheeva

and Chapuis 2008). The use of the superspace concept is by far not limited to aperiodic structures but represent a very powerful link between the periodic and aperiodic allowing to extend the notion of structure type.

The discovery of aperiodic structure has had an enormous impact on pushing back the frontier of so-called disordered structures. Before the concept was well established, many different structures have been published with some caveats on the existence of additional (usually weak) peaks which could not be explained. They were mostly attributed to "impurities" or "disorder". It turns out that these structures were very well ordered but with an aperiodic character.

7. Conclusion and perspectives

Researches and studies dealing with the complexity of mineral structures are continually moving forward. In recent years, the new generation of instruments (with new super-sensible CCD and imaging plate systems) considerably improved the sensitivity of data collection for complex mineral structures of very small samples, in particular incommensurately modulated and disordered structures. Several computer programs are nowadays able to deal with these structures. Beside X-ray diffraction, precession electron diffraction methods are increasing their power allowing the determination of structures from very small particles, down to a few nanometers (e.g., Mugnaioli and Gemmi 2018). Given this extraordinary range of techniques and instrumentations, we think that, beside the ongoing work to determine still-unknown mineral structures, a broader vision is called for in considering the future of mineralogical crystallography. Mineralogy can indeed continue to surprise us and have a strong impact on other disciplines, including chemistry, condensed matter physics, materials science and engineering.

Acknowledgements

The first author would like to express his gratitude to Paul Chaikin, who raised the idea of a review paper on the complexity of mineral structures for the Physics community. He fully understood the prominent role of mineralogical crystallography in the advancements of structural science. The manuscript took advantage from the review of two anonymous reviewers. The research was funded by MIUR-PRIN2017, project "TEOREM deciphering geological processes using Terrestrial and Extraterrestrial ORE Minerals", prot. 2017AK8C32 (P.I. Luca Bindi). SVK was supported in this work by the Russian Science Foundation (grant 19-17-00038). GC thanks Alla Arakcheeva for the critical reading of some portion of the text and for her help in the preparation of some drawings.

References

Angel RJ, Burnham CW 1991 Pyroxene-pyroxenoid polysomatism revisited: A clarification. Am. Mineral 76 900–903

Arakcheeva A, Chapuis G 2005 A reinterpretation of the phase transitions in Na_2CO_3. Acta Crystallogr. B61 601–607

Arakcheeva A, Chapuis G 2008 Capabilities and limitations of a (3+d)-dimensional incommensurately modulated structure as a model for the derivation of an extended family of compounds: example of the scheelite-like structures. Acta Crystallogr. B64 12–25

Arakcheeva A, Bindi L, Pattison P, Meisser N, Chapuis G, Pekov I 2010 The incommensurately modulated structures of natural natrite at 120 and 293 K from synchrotron X-ray data. Am. Mineral. 95 574–581

Belin R, Zerouale A, Pradel A, Ribes M 2001 Ion dynamics in the argyrodite compound Ag_7GeSe_5I: non-Arrhenius behavior and complete conductivity spectra. Solid State Ion. 143 445–455

Belokoneva, E.L. 2005 Borate crystal chemistry in terms of the extended OD theory: topology and symmetry analysis. Cryst. Rev. 11 151–198

Bennet CH 1990 How to define complexity in physics, and why. *Complexity, Entropy, and the Physics of Information. Santa Fe Institute Studies in the Sciences of Complexity* (W.H. Zurek, editor). Volume VIII. Addison-Wesley, Boston, USA pp. 137–48

Biagioni C, Moëlo Y 2017 Lead-antimony sulfosalts from Tuscany (Italy). XIX. Crystal chemistry of chovanite from two new occurrences in the Apuan Alps and its 8 Å crystal structure. Mineral. Mag. 81 811–831

Biagioni C, Moëlo Y, Orlandi P, Stanley CJ 2016 Lead-antimony sulfosalts from Tuscany (Italy). XVII. Meerschautite, $(Ag,Cu)_{5.5}Pb_{42.4}(Sb,As)_{45.1}S_{112}O_{0.8}$, a new expanded derivative of owyheeite from the Pollone mine, Valdicastello Carducci: occurrence and crystal structure. Mineral. Mag. 80 675–690

Biagioni C, Bindi L, Moëlo Y 2018 Another step toward the solution of the real structure of zinkenite. Z. Kristallogr. 233 269–277

Bindi L 2020 *Natural Quasicrystals, the Solar System's hidden secrets*. SpringerBriefs in Crystallography, Springer International Publishing, 89 pages

Bindi L, Biagioni C 2018 A crystallographic excursion in the extraordinary world of minerals: the case of Cu- and Ag-rich sulfosalts. Acta Crystallogr B74 527–538

Bindi L., Menchetti S 2011 Fast ion conduction character and ionic phase-transition in silver sulfosalts: The case of fettelite $[Ag_6As_2S_7][Ag_{10}HgAs_2S_8]$. Am. Mineral. 96 792–796

Bindi L, Bonazzi P, Dušek M, Petříček V, Chapuis G 2001 Five-dimensional structure refinement of natural melilite, $(Ca_{1.89}Sr_{0.01}Na_{0.08}K_{0.02})(Mg_{0.92}Al_{0.08})(Si_{1.98}Al_{0.02})O_7$. Acta Crystallogr. B57 739–746

Bindi L, Evain M, Menchetti S 2006a Temperature dependence of the silver distribution in the crystal structure of natural pearceite, $(Ag,Cu)_{16}(As,Sb)_2S_{11}$. Acta Crystallogr. B62 212–219

Bindi L, Evain M, Pradel A, Albert S, Ribes M, Menchetti S 2006b Fast ionic conduction character and ionic phase-transitions in disordered crystals: The complex case of the minerals of the pearceite-polybasite group. Phys. Chem. Miner. 33 677–690

Bindi L, Evain M, Spry PG, Menchetti S 2007 The pearceite-polybasite group of minerals: Crystal chemistry and new nomenclature rules. Am. Mineral. 92 918–925

Bindi L, Keutsch FN, Francis CA, Menchetti S 2009a Fettelite, $[Ag_6As_2S_7][Ag_{10}HgAs_2S_8]$ from Chañarcillo, Chile: Crystal structure, pseudosymmetry, twinning, and revised chemical formula. Am. Mineral. 94 609–615

Bindi L, Arakcheeva A, Chapuis G 2009b The role of silver on the stabilization of the incommensurately modulated structure in calaverite, $AuTe_2$. Am. Mineral. 94 728–736

Bindi L, Steinhardt PJ, Yao N, Lu PJ 2009c Natural quasicrystals. Science 324 1306–1309

Bindi L, Steinhardt PJ, Yao N, Lu PJ 2011 Icosahedrite, $Al_{63}Cu_{24}Fe_{13}$, the first natural quasicrystal. Am. Mineral. 96 928–931

Bindi L, Nestola F, Guastoni A, Zorzi A, Peruzzo L, Raber T 2012a Te-rich canfieldite, $Ag_8Sn(S,Te)_6$, from Lengenbach quarry, Binntal, Canton Valais, Switzerland: Occurrence, description and crystal structure. Can. Mineral. 50 111–118

Bindi L, Eiler JM, Guan Y, Hollister LS, Macpherson G, Steinhardt PJ, Yao N 2012b Evidence for the extraterrestrial origin of a natural quasicrystal. Proc. Natl. Acad. Sci. USA 109 1396–1401

Bindi L, Yao N, Lin C, Hollister LS, Andronicos CL, Distler VV, Eddy MP, Kostin A, Kryachko V, Macpherson GJ, Steinhardt WM, Yudovskaya M, Steinhardt PJ 2015 Natural quasicrystal with decagonal symmetry. Sci. Rep. 5 9111

Bindi L, Biagioni C, Martini B, Salvetti A 2016a Ciriottiite, $Cu(Cu,Ag)_3Pb_{19}(Sb,As)_{22}(As_2)S_{56}$, the Cu-analogue of sterryite from the Tavagnasco Mining District, Piedmont, Italy. Minerals 6 8

Bindi L, Lin C, Ma C, Steinhardt PJ 2016b Collisions in outer space produced an icosahedral phase in the Khatyrka meteorite never observed previously in the laboratory. Sci. Rep. 6 38117

Bindi L, Keutsch FN, Morana M, Zaccarini F 2017a Spryite, $Ag_8(As^{3+}_{0.5}As^{5+}_{0.5})S_6$: structure determination and inferred absence of superionic conduction of the first As^{3+}-bearing argyrodite. Phys. Chem. Miner. 44 75–82

Bindi L, Petříček V, Biagioni C, Plášil J, Moëlo Y 2017b Could incommensurability in sulfosalts be more common than thought? The case of meneghinite, $CuPb_{13}Sb_7S_{24}$. Acta Crystallogr. B73 369–376

Bindi L, Stanley C 2020 Natural versus synthetic quasicrystals: Analogies and differences in the optical behaviour of icosahedral and decagonal quasicrystals. Rend. Lincei (Scienze Fisiche e Naturali) 31 9–17

Blatov VA, Shevchenko AP, Proserpio DM 2014 Applied topological analysis of crystal structures with the program package ToposPro. Cryst. Growth Des. 14 3576–3586

Bonazzi P, Menchetti S, Sabelli C 1987 Structure refinement of kermesite: symmetry, twinning and comparison with stibnite. N. Jahrb. Min. Monat. 1987 557–567

Bonazzi P, Lampronti GI, Bindi L, Zandari S 2005 Wakabayashilite, $[(As,Sb)_6S_9][As_4S_5]$: crystal structure, pseudosymmetry, twinning, and revised chemical formula. Am. Mineral. 90 1108–1114

Boysen H, Kek S 2015 The modulated structure of labradorite. Z. Kristallogr. 230 23–35

Brouns E, Visser JW, De Wolff PM 1964 An anomaly in the crystal structure of Na_2CO_3. Acta Crystallogr. 17 614

Bussen IV, Gannibal LF, Goiko EA, Mer'kov AN, Nedorezova AP 1972 Ilmajokite, a new mineral from the Lovozero Tundra Zap. Vseross. Mineral. Obshch. (Proc. Russ. Mineral. Soc.) 101 75–79 (in Russian)

Cámara F, Bellatreccia F, Della Ventura G, Mottana A, Bindi L, Gunter ME, Sebastiani M 2010 Fantappièite, a new mineral of the cancrinite– sodalite group with a 33-layer stacking sequence: occurrence and crystal structure Am. Mineral. 95 472–480

Cameron M, Sueno S, Prewitt CT, Papike JJ 1973 High-temperature crystal chemistry of acmite, diopside, hedenbergite, jadeite, spodumene, and ureyite. Am. Mineral. 58 594–618

Dam B, Janner A 1986 A Superspace Approach to the Structure and Morphology of Tetramethylammonium Tetrachlorozincate, $C_4H_{12}N_2ZnCl_4$. Acta Crystallogr. B42 69–77

de Wolff PM, Janssen T, Janner A 1981 The Superspace Groups for Incommensurate Crystal-Structures with a One-Dimensional Modulation. Acta Crystallogr. A37 625–636

Depmeier W 2009 Minerals as advanced materials. Crystal Res. & Tech. 44 1122–1130

Dittrich H, Stadler A, Topa D, Schimper H-J and Basch A 2009 Progress in sulfosalt research. Phys. Status Solidi A 206 1034–1041

Dornberger-Schiff K 1964 Zur Strukturanalyse zweidimensional fehlgeordneter OD-strukturen: Die Strukturbestimmung des Natriumtetrametaphosphats $Na_2H_2P_4O_{12}$. Acta Crystallogr. 17 482–491

Dornberger-Schiff K, Grell-Niemann H 1961 On the theory of order–disorder (OD) structures. Acta Crystallogr. 14 167–177

Dušek M, Chapuis G, Meyer M and Petříček V 2003 Sodium carbonate revisited. Acta Crystallogr. B59 337–352

Edenharter A, Koto K, Nowacki W 1971 Uber Pearceit, Polybasit und Binnit. N. Jahr, Miner. Monat. 1971 337–341

Ettema ARHF, Stegink TA, Haas C 1994 The valence of Au in $AuTe_2$ and AuSe studied by x-ray absorption spectroscopy. Solid State Comm. 90 211–213

Eulenberger G 1977 Die kristallstrukture der tieftemperaturmodifikation von Ag_8GeS_6. Monat. Chem. 108 901–913

Euler R, Hellner E 1960 Über complex zusammengesetzte sulfidische erze. VI. Zur kristallstruktur des meneghinits, $CuPb_{13}Sb_7S_{24}$. Z. Kristallogr. 113 345–372

Evain M, Gaudin E, Boucher F, Petříček V, Taulelle F 1998 Structures and phase transitions of the A_7PSe_6 (A = Ag,Cu) argyrodite-type ionic conductors. I. Ag_7PSe_6. Acta Crystallogr. B54 376–383.

Evain M, Bindi L, Menchetti S 2006 Structural complexity in minerals: twinning, polytypism and disorder in the crystal structure of polybasite, $(Ag,Cu)_{16}(Sb,As)_2S_{11}$. Acta Crystallogr. B62 447–456

Fedorov ES 1913 Crystals of the cubic syngony *Zap. Gorn. Inst. (Proc. Mining Inst.)* 4 312–320 (in Russian)

Fedorov ES 1914 Weitere krystallochemische Behlerungen an der Hand der Tabellen zur krystallochemischen Analyse *Z. Kristallogr.* 53 337–388

Ferraris G, Ivaldi G 2002 Structural features of micas. Rev. Mineral. Geochem. 46 117–154

Ferraris G, Gula A, Ivaldi G, Nespolo M, Sokolova E, Uvarova Y, Khomyakov AP 2001 First structure determination of an MDO-2*O* mica polytype associated with a 1*M* polytype. Eur. J. Mineral. 13 1013–1023

Ferraris G, Makovicky E, Merlino S 2008 Crystallography of Modular Materials. Oxford University Press, Oxford, U.K., 384 p.

Ferraris G, Merlino S 2005 Micro- and Mesoporous Mineral Phases. Rev. Min. & Geoch 57, 1–448

Frondel C 1963 Isodimorphism of the polybasite and pearceite series. Am. Mineral. 48 565–572

Garavelli A, Mozgova NN, Orlandi P, Bonaccorsi E, Pinto D, Moëlo Y, Borodaev YS 2005 Rare sulfosalts from Vulcano, Aeolian Islands, Italy. VI. Vurroite, $Pb_{20}Sn_2(Bi,As)_{22}S_{54}Cl_6$, a new mineral species. Can Mineral 43 703–711

Gaudin E, Boucher F, Evain M 2001 Some factors governing Ag^+ and Cu^+ low coordination in chalcogenide environments. J. Solid State Chem. 160 212–221

Goldschmidt V, Palache C and Peacock M 1931 Über calaverit. N. Jahr. Min. 63 1–58

Gross JT, Yellen J 2006 *Graph Theory and Its Applications*. Boca Raton, FL, CRC Press

Groth P 1921 *Elemente der Physikalischen und Chemischen Krystallographie*, R. Oldenbourg München Berlin p. 274–278

Guggenheim S 1981 Cation ordering in lepidolite type $2M_2$ from Radkovice. Am. Mineral. 66 1221–1232

Guinier A, Bokij GB, Boll-Dornberger K, Cowley JM, Ďurovič S, Jagodzinski H, Khrisna P, DeWolff PM, Zvyagin BB, Cox DE, Goodman P, Hahn Th, Kuchitsu K, Abrahams SC 1984 Nomenclature of Polytype Structures. Report of the International Union of crystallography Ad-Hoc Committee on the Nomenclature of Disordered, Modulated and Polytype Structures. Acta Crystallogr. A40 399–404

Hall HT 1967 The pearceite and polybasite series. Am. Mineral. 52 1311–1321

Harris DC, Nuffield EW, Frohberg MH 1965 Studies of mineral sulphosalts: XIX-Selenian polybasite. Can. Mineral. 8 172–184

Hemingway BS, Evans HT, Nord GL, Haselton HT, Robie RA, Mcgee JJ 1986 Åkermanite; phase transitions in heat capacity and thermal expansion, and revised thermodynamic data. Can. Mineral. 24 425–434

Hicks WD, Nuffield EW 1978 Natural and synthetic meneghinite. Can. Mineral. 16 393–395

Hu J, Asimow PD, Ma C, Bindi L 2020 First synthesis of a unique icosahedral phase from the Khatyrka meteorite by shock recovery experiment. IUCrJ 7 434–444

Janner A, Dam B 1989 The Morphology of Calaverite ($AuTe_2$) from Data of 1931 - Solution of an Old Problem of Rational Indexes. Acta Crystallogr. 45 115–123

Janssen T, Chapuis G and Boissieu M 2018 *Aperiodic crystals: from modulated phases to quasicrystals: structure and properties,* Oxford, Oxford University Press.

Janssen T, Janner A, Looijenga-Vos A, Wolff PMD 2008 Incommensurate and Commensurate Modulated Structures. *International Table of Crystallography.* Kluwer Academic Publishers.

Jaszczak JA, Rumsey MA, Bindi L, Hackney SA, Wise MA, Stanley CJ, Spratt J 2016 Merelaniite, $Mo_4Pb_4VSbS_{15}$, a new molybdenum-essential member of the cylindrite group, from the Merelani tanzanite deposit, Lelatema Mountains, Manyara Region, Tanzania. Minerals 6 115

Jin SY, Xu HF 2017 Solved: The enigma of labradorite feldspar with incommensurately modulated structure. Am. Mineral. 102 21–32

Kampf AR, Hughes JM, Nash BP, Marty J 2016 Vanarsite, packratite, morrisonite, and gatewayite: four new minerals containing the $[As^{3+}V^{4+,5+}_{12}As^{5+}_{6}O_{51}]$ heteropolyanion, a novel polyoxometalate cluster Can. Mineral. 54 145–162

Kampf AR, Hughes JM, Nash BP, Marty J, Rose TP 2020 Lumsdenite, $NaCa_3Mg_2(As^{3+}V^{4+}_{2}V^{5+}_{10}As^{5+}_{6}O_{51})\cdot 45H_2O$, a new polyoxometalate mineral from the Packrat mine, Mesa County, Colorado, USA Can. Mineral. 58 137–151

Korekawa M. 1967 *Theorie der Satellitenreflexe.* Habilitationsschrift, Ludwig-Maximilians-Universität Munich.

Korekawa M, Jagodzinski H 1967 Die Satellitenreflexe des Labradorits. Schweiz. Mineral. Petrogr. Mitt. 47 269–278.

Krivovichev SV 2009 Structural Crystallography of Inorganic Oxysalts. IUCr Monographs on Crystallography. Oxford University Press, 2009. ISBN 978-0-19-921320-7.
Krivovichev SV 2012a Topological complexity of crystal structures: quantitative approach. Acta Crystallogr. A68 393–398
Krivovichev SV 2012b Information-based measures of structural complexity: Application to fluorite-related structures. Struct. Chem. 23 1045–1052
Krivovichev SV 2013a Structural complexity of minerals: information storage and processing in the mineral world. Mineral. Mag. 77 275–326
Krivovichev SV 2013b Structural and topological complexity of zeolites: An information-theoretic analysis. Micropor. Mesopor. Mater. 171 223–229
Krivovichev SV 2014 Which inorganic structures are the most complex? Angew. Chem. Int. Ed. 53 654–661
Krivovichev SV 2016a Structural complexity and configurational entropy of crystalline solids Acta Crystallogr. B72 274–276
Krivovichev SV 2016b Structural complexity of minerals and mineral parageneses: information and its evolution in the mineral world. *Highlights in Mineralogical Crystallography*; Danisi, R., Armbruster, T., Eds.; Walter de Gruyter GmbH: Berlin, Germany; Boston, MA, USA p. 31–73
Krivovichev SV 2017 Structure description, interpretation and classification in mineralogical crystallography. Crystallogr. Rev. 23 2–71
Krivovichev SV 2018 Ladders of information: What contributes to the structural complexity in inorganic crystals. Z. Kristallogr. 233 155–161
Krivovichev SV 2020 Polyoxometalate clusters in minerals: review and complexity analysis. Acta Crystallogr. B76 in press
Krivovichev SV, Krivovichev VG 2020 The Fedorov-Groth law revisited: complexity analysis using mineralogical data. Acta Crystallogr. A76 429–431
Krivovichev SV, Krivovichev VG, Hazen RM 2018 Structural and chemical complexity of minerals: correlations and time evolution. Eur. J. Mineral. 30 231–236
Kuhs W F and Heger G 1979 Fast ion transport in solids. In P Vashishta, J N Mundy and G K Shenoy, Eds, pp. 233–236. Elsevier, Amsterdam
Lima-de-Faria J 1990 *History Atlas of Crystallography*. Springer Publishing Group, 158 pages
Laufek F, Pažout R, Makovicky E 2007 Crystal structure of owyheeite, $Ag_{1.5}Pb_{4.43}Sb_{6.07}S_{14}$: refinement from powder synchrotron X-ray diffraction. Eur. J. Mineral. 19 557–566
Lengauer CL, Giester G, Tillmans E 1997 Mineralogical characterization of paulingite from Vinarická Hora, Czech Republic. Mineral. Mag. 61 591–606
Makovicky E 1993 Rod-based sulphosalt structures derived from the SnS and PbS archetypes. Eur. J. Mineral. 5 545–591
Makovicky E 1997 Modular crystal chemistry of sulphosalts and other complex sulphides. EMU Notes in Mineralogy 1 237–271
Makovicky E, Hyde BG 1981. *Non-commensurate (misfit) layer structures*. Inorganic Chemistry. Springer Berlin Heidelberg
Makovicky E, Hyde B G 1992 Incommensurate, two-layer structures with complex crystal chemistry: Minerals and related synthetics. Mat. Sci. Forum 100 and 101 1–100
Makovicky E, Olsen PN 2015 The order-disorder character of owyheeite. Can Mineral. 53 879–884

Makovicky E and Topa D 2009 The crystal structure of sulfosalts with the boxwork architecture and their new representative, $Pb_{15-2x}Sb_{14+2x}S_{36}O_x$. Can. Mineral. 47 3–24

Makovicky E, Balić-Žunić T and Topa D 2001 The crystal structure of neyite, $Ag_2Cu_6Pb_{25}Bi_{26}S_{68}$. Can. Mineral. 39 1365–1376

Mandarino JA, Nickel EH, Cesbron F 1984 Rules of procedure of the Commission on New Minerals and Mineral Names, International Mineralogical Association. Can. Mineral. 22 367–368

Meerschaut A., Palvadeau P., Moëlo Y., Orlandi P. 2001 Lead-antimony sulfosalts from Tuscany (Italy). IV. Crystal structure of pillaite, $Pb_9Sb_{10}S_{23}ClO_{0.5}$, an expanded monoclinic derivative of hexagonal $Bi(Bi_2S_3)_9I_3$, from the zinkenite group. Eur. J. Mineral. 13 779–790

Mereiter K. 1979 Refinement of the crystal structure of langbeinite, $K_2Mg_2(SO_4)_3$. N. Jahr. Min. Monat 1979 182–188

Minčeva-Stefanova I, Bonev I, Punev L 1979 Pearceite with an intermediate unit cell – first discovery in nature. Geokh. Mineral. Petrol. 11 13–34 (in Bulgarian).

Moëlo Y, Mozgova NN, Picot P, Bortnikov N, Vrubleskaya Z 1984 Cristallochimie de l'owyheeite: Nouvelles données. Tschermaks Mineral Petrog Mitt 32 271–284

Moëlo Y, Meerschaut A, Orlandi P, Palvadeau P 2000 Lead-antimony sulfosalts from Tuscany (Italy): II – Crystal structure of scainiite, $Pb_{14}Sb_{30}S_{54}O_5$, an expanded monoclinic derivative of $Ba_{12}Bi_{24}S_{48}$ hexagonal sub-type (zinkenite group). Eur. J. Mineral. 12 835–846

Moëlo Y, Makovicky E, Mozgova NN, Jambor JJ, Cook N, Pring A, Paar W, Nickel EH, Graeser S, Karup-Møller S, Balić-Žunić T, Mumme WG, Vurro F, Topa D, Bindi L, Bente K, Shimizu M 2008 Sulfosalt systematics: a review. Report of the sulfosalt sub-committee of the IMA Commission on Ore Mineralogy. Eur. J. Mineral. 20 7–46

Moëlo Y, Guillot-Deudon C, Evain M, Orlandi P, Biagioni C 2012 Comparative modular analysis of two complex sulfosalt structures: sterryite, $Cu(Ag,Cu)_3Pb_{19}(Sb,As)_{22}(As–As)S_{56}$, and parasterryite, $Ag_4Pb_{20}(Sb,As)_{24}S_{58}$. Acta Crystallogr. B68 480–492

Moëlo Y, Pecorini R, Ciriotti ME, Meisser N, Caldes MT, Orlandi P, Petit PE, Martini B, Salvetti A 2013 Tubulite, $\sim Ag_2Pb_{22}Sb_{20}S_{53}$, a new Pb-Ag-Sb sulfosalt from Le Rivet quarry, Peyrebrune ore field (Tarn, France) and Biò, Borgofranco mines, Borgofranco d'Ivrea (Piedmont, Italy). Eur. J. Mineral. 25 1017–1030

Momma K, Izumi F 2011 VESTA 3 for three-dimensional visualization of crystal, volumetric and morphology data. J. Appl. Crystallogr. 44 1272–1276

Mugnaioli E, Gemmi M 2018 Single-crystal analysis of nanodomains by electron diffraction tomography: mineralogy at the order-disorder borderline. Z. Kristallogr. 233 163–178

Mullen DJE, Nowacki W 1972 Refinement of the crystal structures of realgar, AsS, and orpiment, As_2S_3. Z. Kristallogr. 136 48–65

Nespolo M, Bouznari K 2017 Modularity of crystal structures: a unifying model for the biopyribole-palysepiole series. Eur. J. Mineral. 29 369–383

Nespolo M, Ďurovič S 2002 Crystallographic basis of polytypism and twinning in micas. Rev. Mineral. Geochem. 46 155–280

Nespolo M, Souvignier B, Stöger B 2020 Groupoid description of modular structures. Acta Crystallog. A76 334–344

Nespolo M, Takeda H, Kogure T, Ferraris G 1999 Periodic Intensity Distribution (PID) of mica polytypes: symbolism, structural model orientation and axial settings. Acta Crystallogr. A55 659–676

Nespolo M, Umayahara A, Eon J-G 2018 A groupoid and graph-theoretical analysis of the biopyribole-palysepiole series. Eur. J. Mineral. 30 413–428

Nickel EH 1992 Solid solutions in mineral nomenclature. Can. Mineral. 30 231–234

Nickel EH 1995 The definition of a mineral. Can. Mineral. 33 689–690

Olds TA, Plášil J, Kampf AR, Simonetti A, Sadergaski LR, Chen YS, Burns PC 2017 Ewingite: Earth's most complex mineral. Geology 45 1007–1010

Olmi F, Sabelli C 1994 Brizziite, $NaSbO_3$, a new mineral from the Cetine mine (Tuscany, Italy): description and crystal structure. Eur. J. Mineral. 6 667–672.

Orlandi P, Moëlo Y, Meerschaut A, Palvadeau P 1999 Lead-antimony sulfosalts from Tuscany (Italy). I. Scainiite, $Pb_{14}Sb_{30}S_{54}O_5$, the first Pb-Sb oxy-sulfosalt, from Buca della Vena mine. Eur. J. Mineral. 11 949–954

Orlandi P, Meerschaut A, Moëlo Y, Palvadeau P, Léone P 2005 Lead-antimony sulfosalts from Tuscany (Italy). VIII. Rouxelite, $Cu_2HgPb_{22}Sb_{28}S_{64}(O,S)_2$, a new sulfosalt from Buca della Vena mine, Apuan Alps: definition and crystal structure. Can. Mineral. 43 919–933

Orlandi P, Moëlo Y, Campostrini I, Meerschaut A 2007 Lead-antimony sulfosalts from Tuscany (Italy). IX. Marrucciite, $Hg_3Pb_{16}Sb_{18}S_{46}$, a new sulfosalt from Buca della Vena mine, Apuan Alps: Definition and crystal structure. Eur. J. Mineral. 19 267–279

Oszlányi G, Sütő A 2004 *Ab initio* structure solution by charge flipping. Acta Crystallogr. A60 134–141

Oudin E, Picot P, Pillard F, Moëlo Y, Burke E, Zakrzewski A 1982 La benavidesite, $Pb_4(Mn,Fe)Sb_6S_{14}$, un nouveau mineral de la serie de la jamesonite. Bull. Minéral. 105 166–169

Padma Kumar P, Yashonath S 2006 Ionic conduction in the solid state. J. Chem. Sci. 118 135–154

Palatinus L, Chapuis G 2007 SUPERFLIP - a computer program for the solution of crystal structures by charge flipping in arbitrary dimensions. J. Appl. Crystallogr. 40 786–790

Palvadeau P, Meerschaut A, Orlandi P, Moëlo Y 2004 Lead-antimony sulfosalts from Tuscany (Italy). VII. Crystal structure of pellouxite, ~ $(Cu,Ag)_2Pb_{21}Sb_{23}S_{55}ClO$, an expanded monoclinic derivative of $Ba_{12}Bi_{24}S_{48}$ hexagonal sub-type (zinkenite group). Eur. J. Mineral. 16 845–855

Pankova YA, Gorelova LA, Krivovichev SV, Pekov IV 2018 The crystal structure of ginorite, $Ca_2[B_{14}O_{20}(OH)_6]\cdot 5H_2O$, and the analysis of dimensional reduction and structural complexity in the CaO-B_2O_3-H_2O system. Eur. J. Mineral. 30 277–287

Pasero M 2020 The New IMA List of Minerals. http://pubsites.uws.edu.au/ima-cnmnc/

Pauling L 1929 The principles determining the structure of complex ionic crystals. J. Amer. Chem. Soc. 51 1010–1026

Peacock MA, Berry LG (1947) Studies of mineral sulphosalts: XII-Polybasite and pearceite. Mineral. Mag. 28 2–13

Peacor DR, Essene EJ, Brown PE, Winter GA 1978 The crystal chemistry and petrogenesis of a magnesian rhodonite. Am. Mineral. 63 1137–1142

Petříček V, Dušek M, Palatinus L 2014. Crystallographic Computing System JANA2006: General features. Z. Kristallogr. 229 345–352

Pinckney LR, Burnham CW 1988 High-temperature crystal structure of pyroxmangite. Am. Mineral. 73 809–817

Pinto D, Bonaccorsi E, Balić-Žunić T, Makovicky E 2008 The crystal structure of vurroite, $Pb_{20}Sn_2(Bi,As)_{22}S_{54}Cl_6$: OD-character, polytypism, twinning and modular description. Am. Mineral. 93 713–727

Rao RP, Adams S 2011 Studies of lithium argyrodite solid electrolytes for all-solid-state batteries. Phys. Status Solidi A208 1804–1807
Redhammer GJ, Roth G 2002 Single-crystal structure refinements and crystal chemistry of synthetic trioctahedral micas $KM_3(Al,Si)_4O_{10}(OH)_2$, where M = Ni, Mg, Co, Fe, Al. Am. Mineral. 87 1464–1476
Riester M, Böhm H, Petříček V. 2000 The commensurately modulated structure of the lock-in phase of synthetic Co-åkermanite, $Ca_2CoSi_2O_7$. Z. Kristallogr. 215 102–109
Schutte WJ, de Boer JL 1988 Valence fluctuations in the incommensurately modulated structure of Calaverite $AuTe_2$. Acta Crystallogr. B44 486–494
Shchipalkina NV, Pekov IV, Chukanov NV, Biagioni C, Pasero M 2019 Crystal chemistry and nomenclature of rhodonite-group minerals. Mineral. Mag. 83 829–835
Shechtman D, Blech I, Gratias D, Cahn JW 1984 Metallic Phase with Long-Range Orientational Order and No Translational Symmetry. Phys. Rev. Lett. 53 1951–1953
Siidra OI, Zenko DS, Krivovichev SV 2014 Structural complexity of lead silicates: Crystal structure of $Pb_{21}[Si_7O_{22}]_2[Si_4O_{13}]$ and its comparison to hyttsjöite. Am. Mineral. 99 817–823
Sugaki A, Kitakaze A, Yoshimoto T 1983 Synthesized minerals of polybasite and pearceite series - synthetic sulfide minerals (XII). Sci. Rep. Tohoku Univ. Series 3: Min. Petr. Ec. Geol. 15 461–469
Takéuchi Y 1997 *Tropochemical cell-twinning. A structure building mechanism in crystalline solids*. Tokyo: Terra Scientific Publishing Company
Thompson JB Jr 1978 Biopyriboles and polysomatic series. Am. Mineral. 63 239–249
Umayahara A, Nespolo M 2018 Derivative structures based on the sphere packing. Z. Kristallogr. 233 179–203
Van Aalst W, Den Holander J, Peterse WJAM, De Wolff PM 1976 The modulated structure of γ-Na_2CO_3 in a harmonic approximation. Acta Crystallogr. B32 47-58
Van Heurck C, Van Tendeloo G, Amelinckx S 1992 The modulated structure in the melilite $Ca_2ZnGe_2O_7$. Phys. Chem. Miner. 18 441–452
van Smaalen S 2012 *Incommensurate crystallography.* Oxford, New York, Oxford University Press.
van Smaalen S, Campbell BJ, Stokes HT 2013 Equivalence of superspace groups. Acta Crystallogr. A69 75–90
Wang N. 1978 New data for Ag_8SnS_6 (canfieldite) and Ag_8GeS_6 (argyrodite). N. Jahr. Miner. Monat. 1978 269–272
Wang B, Chen SC, Greenblatt M 1994 The crystal structure and ionic conductivity of the ilmenite polymorph of $NaSbO_3$. J. Solid St. Chem. 108 184–188
Weber HP 1983 Ferrosilite III, the high-temperature polymorph of $FeSiO_3$. Acta Crystallogr. C39 1–3
Wells AF 1975 *Structural Inorganic Chemistry*. 4th edition. Oxford: Oxford University Press, xxiii+1095 pp.
Yamamoto A 1996 Crystallography of quasiperiodic crystals. Acta Crystallogr. A52 509–560
Zanazzi PF, Montagnoli M, Nazzareni S, Comodi P 2007 Structural effects of pressure on monoclinic chlorite: a single-crystal study. Am. Mineral. 92 655–661
Zelenski M, Garavelli A, Pinto D, Vurro F, Moëlo Y, Bindi L, Makovicky E, Bonaccorsi E 2009 Tazieffite, $Pb_{20}Cd_2(As,Bi)_{22}S_{50}Cl_{10}$, a new chloro-sulfosalt from Mutnovsky volcano, Kamchatka Peninsula, Russian Federation. Am. Mineral. 94 1312–1324

Zhirnov V, Zadegan RM, Sandhu GS, Church GM, Hughes WL 2016 Nucleic acid memory Nat. Mater. 15 366–370

Zolotarev AA, Krivovichev SV, Cámara F, Bindi L, Zhitova ES, Hawthorne F, Sokolova E 2020 Extraordinary structural complexity of ilmajokite: A multilevel hierarchical framework structure of natural origin. IUCrJ 7 121–128

Figure captions

Figure 1. Hexagonal compact layer of equally sized spheres, with the two differently oriented triangular cavities indicated as B and C. The centres of the spheres are indicated as A.

Figure 2. The octahedral (O) and the two tetrahedral (T) cavities in the region between two compact layers of equally sized spheres in which the spheres in upper layer are positioned on one of the triangular cavities of the lower layer.

Figure 3. The two trigonal prismatic (P_1 and P_2) cavities in the region between two compact layers of equally sized spheres in which the spheres in upper layer are positioned above the spheres of the lower layer. This and the following figures, up to Fig. 23, drawn with VESTA (Momma and Izumi 2011).

Figure 4. The tetrahedral (T) and octahedral (O) sheets building the layer phyllosilicates (a) Perspective view of the T sheet. (b). The dioctahedral sheet seen along [001]*. Red spheres are oxygen atoms, smaller white spheres are hydrogen atoms. Dashed segments represent hydrogen bonds. (c). The trioctahedral sheet seen along [001]*. Same colour scheme as in (b).

Figure 5. The TOT layer seen (a) along [010] and (b) along [001]*. In (a), the two T sheets are staggered one with respect to the other by about -*a*/3. In (b), the ideal configuration of the T sheet (hexagonal) symmetry is shown, which is however seldom realized in phyllosilicates, a ditrigonal rotation of the tetrahedra being very common. Red and blue spheres are oxygen atoms and hydroxyl groups, respectively. The conventional (rectangular in projection) and primitive (rhomb-shaped in projection) unit cells are shown. The symmetry elements of the point group are also shown: a two-fold axis parallel to *b* (thin line ending with the oval symbol of a twofold rotation axis), a mirror plane normal to it (thick line) and an inversion centre (small white circle at the intersection of the rotation axis and the mirror plane).

Figure 6. The real configuration of the T sheet in a trioctahedral (a) and dioctahedral (b) TOT layer. The ditrigonal rotation, which depends on the actual chemistry of the mineral, is in general more important for the dioctahedral layer because of the size difference between the empty and the occupied octahedral sites.

Figure 7. The real structure of the T sheet in talc and pyrophyllite. Two adjacent T sheets belonging to two successive TOT layers, from which the O sheets have been removed. The ditrigonal cavities (ideally hexagonal) have parallel orientation but are shifted by about (a) *a*/3 for talc (0.2968*a*) and (b) about 1/10 along the [120] direction for pyrophyllite.

Figure 8. The real structure of the T sheet in micas. Two successive TOT layers from which the O sheets have been removed. Between the two T sheets, the interlayer cation (purple) is shown. Even ($2n\times60°$) orientations result in a staggered configuration of the basal oxygen atoms (Fig. 8a, phlogopite-1*M*), whereas odd [$(2n+1)\times60°$] orientation in an eclipsed orientation (Fig. 8b, phlogopite-2*O*, and Fig. 8c, lepidolite-$2M_2$).

Figure 9. In trioctahedral TOT layers the tetrahedra of the same T sheet have parallel or quasi-parallel orientation (a), whereas in dioctahedral TOT layers, because of the size difference between empty and occupied O sites, these tetrahedra are tilted about the basal bridging oxygen atoms.

Figure 10. The interlayer region of 1*M* polytype of chlorite, containing an isolated O sheet, with two T sheets belonging to successive TOT layers. These are equally oriented by shifted by 0.42*a*.

Figure 11. The O sheet seen along [001]*. In red, positions of the hydroxyl groups that are replaced by apical oxygen atoms of the T sheet when forming the TOT layer. In blue, hydroxyl groups the remain in the TOT sheet (the white small circles are hydrogen atoms). Octahedral sides with OH groups in *trans* configurations are shown in white, those with OH groups in *cis* configuration in yellow. replace two thirds of the hydroxyl groups of the O sheets. The remaining OH groups allow to differentiate the octahedral sites. The rhombic-shaped primitive unit cell, shown in the figure, contains one *trans* and two *cis* octahedral sites; the origin has been moved onto the *trans* site to enhance readability of the figure.

Figure 12. Selection of R_5 (a) and R_8 (b) rods from the TOT layer. Numbers identify the octahedra spanning the width of the rod.

Figure 13. The structure of amphiboles, seen along [001]. This structure can be interpreted as composed by R_5 rods, periodic along the *c* axis of the mineral, displaced one with respect to the other along the *a* axis, according to the OH-O_b bonding scheme. Depending on cations occupying the O chain and the nature of the X cation amphiboles are classified in a number of different minerals. In some of these, the empty space □ is sometimes occupied by a monovalent cation, mainly sodium.

Figure 14. The structure of jimthompsonite, seen along [001]. This structure can be interpreted as composed by R_8 rods, periodic along the *c* axis of the mineral, displaced one with respect to the other along the *a* axis, according to the OH-O_b bonding scheme.

Figure 15. The structure of chesterite, seen along [001]. This structure can be interpreted as composed by R_5 and R_8 rods alternating, according to the OH-O_b bonding scheme, i.e. by an alternation of amphibole-like modules and jimthompsonite-like modules.

Figure 16. The structure of palygorskite, seen along [001]. This structure can be interpreted as composed by R_5 rods, periodic along the *c* axis of the mineral, displaced one with respect to the other along the *a* axis, according to the O_b-O_b bonding scheme. Water molecules occur in the regions between the rods.

Figure 17. The structure of sepiolite, seen along [001]. This structure can be interpreted as composed by R_8 rods, periodic along the *c* axis of the mineral, displaced one with respect to the other along the *a* axis, according to the O_b-O_b bonding scheme. Water molecules occur in the regions between the rods.

Figure 18. The structure of kalifersite, seen perspectively along [001]. This structure can be interpreted as composed by an alternation of R_3 rods and R_6 rods, periodic along the *c* axis of the mineral, displaced one with respect to the other along the *a* axis, according to the O_b-O_b bonding scheme.

Figure. 19. The structure of wollastonite, $CaSiO_3$. (a) Projection along the *b* axis, showing that the O chain has a width of three octahedra. (b) projection along [101]*, with the cation sites in a ball-and-stick representation. The period of the tetrahedral chain, between two horizontal black lines, is three tetrahedra.

Figure 20. The structure of pyroxenes, $MSiO_3$ (M = Ca, Mg for diopside, shown in this figure) seen (a) along [001] and (b) along [101]. The larger site, white polyhedron in (a), usually indicated as M2 in the literature, is assimilated to an octahedron for the sake of

comparison with the other structure, although in pyroxenes it does have a octahedral geometry. The period of the tetrahedral chain, between two horizontal black lines, is two tetrahedra. Structural data from Cameron et al. (1973).

Figure 21. The structure of rhodonite, $(Mn^{2+},Fe^{2+},Mg,Ca)SiO_3$ seen along [100]*. The period of the tetrahedral chain, between two horizontal black lines, is five tetrahedra. This structure is composed by a regular alternation of wollastonite-like slabs and pyroxene-like slabs, shown between horizontal red lines. Structural data from Peacor et al. (1978).

Figure 22. The structure of pyroxmangite, $MnSiO_3$, seen along [100]*. The period of the tetrahedral chain, between two horizontal black lines, is seven tetrahedra. This structure is composed by a regular alternation of one wollastonite-like slabs and two pyroxene-like slabs, shown between horizontal red lines. Structural data from Pinckney and Burnham (1988).

Figure 23. The structure of ferrosilite-III, $FeSiO_3$, seen along [110]*. The period of the tetrahedral chain, between two horizontal black lines, is nine tetrahedra. This structure is composed by a regular alternation of one wollastonite-like slabs and three pyroxene-like slabs, shown between horizontal red lines. Structural data from Weber (1983).

Figure 24. The $[(UO_2)_{24}(CO_3)_{30}O_4(OH)_{12}(H_2O)_8]$ cluster in ewingite (a), its skeletal representation (b), the U core (c; the U–U contacts shorter than 4 Å are shown as thick black lines; those between 4 and 6.2 Å as thin black lines; red and blue points indicate centres of the U_3 trimers and midpoints of the shared U–U edges of the U_4 dihedra, respectively), and the arrangements of the red and blue circles that correspond to the intersection of tetrahedron and octahedron, respectively (d).

Figure 25. The $[As^{3+}V^{4+}{}_2V^{5+}{}_{10}As^{5+}{}_6O_{51}]$ cluster in morrisonite in polyhedral (a) and skeletal (b) representations.

Figure 26. The projection of the crystal structure of ilmajokite alog the *c* axis. Legend: Si tetrahedra = yellow, Ti octahedra = blue; H_2O molecules, Na, K, Ba, and Ce atoms are shown as red, light-blue, green, brown, and orange spheres, respectively (after Zolotarev et al. 2020).

Figure 27. Trigonal-prismatic titanosilicate (TPTS) clusters in the crystal structure of ilmajokite shown in polyhedral (a, c) and nodal (b, d) representations. The numbering scheme corresponds to the numbering of Si and Ti atoms from the experiment. The Ce-centered Ti_6 trigonal prism is highlighted in yellow. Legend as in Figure 26 (after Zolotarev et al. 2020).

Figure 28. The hierarchial organization of the crystal structure of ilmajokite separated into eight hierarchy levels (highlighted in grey).

Figure 29. The crystal structure of langbeinite, $K_2Mg_2(SO_4)_3$ (Mereiter 1979), projected down [001]. (SO_4)-tetrahedra are given in yellow and (MgO_6)-octahedra in green. Purple and red circles indicate K and O atoms, respectively. The unit cell and the orientation of the structure are outlined.

Figure 30. The crystal structure of brizziite, $NaSbO_3$ (Olmi and Sabelli 1994). (SbO_6)-octahedra are given in green. Yellow and red circles indicate Na and O atoms, respectively. The unit cell and the orientation of the structure are outlined.

Figure 31. Structure of $(Ag,Cu)_{16}(As,Sb)_2S_{11}$, showing the stacking of the $[(Ag,Cu)_6(As,Sb)_2S_7]$ and $[Ag_9CuS_4]$ layers (see text). The former layer is shown as ball-and-stick, with grey, violet, and yellow circles representing (Ag,Cu)1, (As,Sb), and S sites, respectively. In the latter layer, the positions of Ag atoms (grey circles), are those obtained at RT; Cu is shown as blue circles.

Figure 32. Non-harmonic joint probability density iso-surface for Ag at RT in the $[Ag_9CuS_4]$ layer extended with S2 atoms, exhibiting the Ag diffusion in the *ab* plane. Level of the map: 0.05 $Å^{-3}$. Sulfur and Cu atoms are shown at arbitrary sizes.

Figure 33. Projection of the crystal structure of polybasite-221 along the hexagonal *a* axis. Silver, Cu, Sb, and S atoms are shown as grey, blue, brownish, and yellow circles.

Figure 34. Projection of the crystal structure of polybasite-222 structure along the monoclinic *b* axis, emphasizing the succession of the $[(Ag,Cu)_6Sb_2S_7]^{2-}$ A (A_0) and $[Ag_9CuS_4]^{2+}$ B (B_0) module layers. Same symbols as in Figure 5.

Figure 35. Different unit-cell type in the pearceite-polybasite group of minerals.

Figure 36. Projection of the crystal structure of fettelite along the monoclinic *b* axis, emphasizing the succession of the $[Ag_6As_2S_7]^{2-}$ *A* and $[Ag_{10}HgAs_2S_8]^{2+}$ *B* module layers. Grey, dark violet, red and yellow circles indicate Ag, As, Hg and S atoms, respectively. The unit cell is outlined.

Figure 37. Non-harmonic joint probability density iso-surface for Ag/Hg in the HT-structure of fettelite exhibiting the Ag diffusion in the *ab* plane. Part of the *B* layer extended with S atoms. Level of the map: 0.05 $Å^{-3}$. Sulfur atoms in arbitrary size.

Figure 38. (a) Three-dimensional representation of a joint probability density iso-surface (at the 90 $Å^{-3}$ level) for the gamma form of Ag_7PSe_6 at 473 K, showing Ag diffusion paths within a cluster centered on Se3. Se atoms are represented as spheres of arbitrary size (Evain et al. 1998). (b) Three-dimensional representation of a joint probability density iso-surface (at the 20 $Å^{-3}$ level) showing the cluster connection around the Se2 atom. Se atoms are represented as spheres of arbitrary size and the Se2 splitting is not taken into account for the sake of clarity (Evain et al. 1998).

Figure 39. Spryite, $Ag_8(As^{3+}_{0.5}As^{5+}_{0.5})S_6$, equant crystals surrounding proustite (Ag_3AsS_3) crystals on Mn-bearing calcite. Field of view 1.6 cm.

Figure 40. Crystal structure of spryite as seen down [010] (a). White, light blue, red, and yellow circles correspond to Ag, (Ge, As^{5+}), As^{3+} and S, respectively. (b) Portion of the crystal structure of spryite highlighting the split *M*1-*M*2 positions (see text for explanation). In light blue the *M*1 tetrahedron and with a red circle the *M*2 atom.

Figure 41. Unusual cylindrical aggregates of thin robinsonite fibers from the Monte Arsiccio mine, Apuan Alps, Tuscany, Italy. The aspect ratio of these aggregates, where fibers can show thickness down to less than 500 nm, are larger than 100,000.

Figure 42. Sulfosalt structures showing the three main categories of rod-based structures, i.e., rod layers (boulangerite, $Pb_5Sb_4S_{11}$ – a), chess-board (izoklakeite, $(Cu,Fe,Ag)_2Pb_{27}(Sb,Bi)_{19}S_{57}$ – b), and cyclic (zinkenite, $Pb_9Sb_{22}S_{42}$ – c).

Figure 43. The crystal structure of chovanite, seen down *b*, shown as an example of boxwork structure. Different colors indicate walls (yellow), partitions (light blue), and fill elements (pink). Light blue ellipses indicate the lone-electron-pair micelles, whereas red triangles show the pseudotrigonal axes. Dotted lines indicate the surfaces of weakest bonding.

Figure 44. Two different kermesite-like configurations observed in scainiite. In (a), a Sb_2O_2 ladder can be recognized, whereas (b) shows Sb–O chains (i.e., half of the ladder). The configuration shown in (b) has been reported in several other lead-antimony oxy-sulfosalts. Oxygen, S, Sb, and Pb atoms are shown as red, yellow, brownish, and grey circles, respectively.

Figure 45. The crystal structure of vurroite, as seen down *a*. Circles represent Pb (grey), Bi (violet), As (dark violet), S (yellow), and Cl (green) sites. Sn sites are shown as brown polyhedra.

Figure 46. Structural details of the sterryite – parasterryite pair. (a) Crystal structure of sterryite as seen down *a*; (b) complex column of sterryite. The red ellipse indicates the short arm, whose arrangement is shown in (c). Parasterryite has a similar complex column (d), differing mainly for the short arm (red ellipse), shown in (e). Ag, Cu, Pb, Sb, As, and S atoms are shown as grey, blue, dark grey, brownish, dark violet, and yellow circles, respectively.

Figure 47. The two complex columns characterizing the crystal structure of meerschautite (a, c) and details of their short arms (b, d).

Figure 48. Meneghinite, as lead grey striated prismatic crystals, up to 1 cm long, associated with siderite and quartz, from the Bottino mine (Tuscany, Italy) (a) and its crystal structure as seen down the 4 Å axis. Copper, Pb, Sb, and S atoms are shown as blue, dark grey, brownish, and yellow circles, respectively.

Figure 49. Merelaniite, black whiskers up to ~ 3 mm in length associated with tabular colorless crystals of "stilbite", showing inclusions of black flattened crystals of graphite. The specimen is from Merelani, Lelatema Mountains, Tanzania.

Figure 50. Reconstructed reciprocal space layer of natrite with indices of diffraction reflections *h*2*l*. In addition to the main reflections at the lattice nodes *h*2*l* defined by the two vectors $\mathbf{a}_1$*and $\mathbf{a}_3$*, we observe a series of equidistant reflections aligned along the vector **q** called satellite reflections.

Figure 51. Embedding of the three-dimensional reciprocal space into a higher dimensional space called superspace. The additional reciprocal space vector $\mathbf{a}_{S4}^*$consists of two components, the *external* component **q** and the *internal* component $\mathbf{e}_4$*.

Figure 52. (a) A sinusoidal displacement modulation along $\mathbf{a}_2$. The period of the modulation λ is the inverse of ||**q**||. Corresponding 2-dimensional section in the $\mathbf{a}_{S2}$, $\mathbf{a}_{S4}$ plane. The displacements from the average positions along $\mathbf{a}_2$ is given by the intersections of the sinusoidal curve along the "real crystal" line.

Figure 53. Distinction between the three families of aperiodic structures based on their reciprocal space embeddings.

Figure 54. Portion of γ-Na_2CO_3, the room temperature phase of natrite. Oxygen forming triangular coordination around the C atoms (black) are omitted. The links between atoms are contact distances between Na and C atoms shorter than 3.4 Å. The structure can be interpreted as a series of parallel graphite-like C-Na3 layers stacked along the *c* axis. Na1 and Na2 are located between the layers.

Figure 55. Analysis of the incommensurate structure of γ-Na_2CO_3 in terms of the m_M and m_V planes containing the Na and C atoms. Links are only indicated for Na, C contact distances smaller than 3.1 Å.

Figure 56. (a) Average structure of calaverite consisting of parallel edge-sharing layers of Te octahedra with (Au,Ag) atoms at their centre. (b) *t*-plot representation of the (Au,Ag)-Te distances from the refinement in superspace in the incommensurate structure of $Au_{0.9}Ag_{0.1}Te_2$ with ordered Ag distribution. Numbers refer to the six independent (Au,Ag)-Te distances in each [(Au,Ag)Te_6]-octahedron.

Figure 57. Portion of the incommensurate structure of $Au_{0.9}Ag_{0.1}Te_2$ with ordered distribution of Ag on the Au position. The thick grey lines indicate the (Au,Ag)–Te distances shorter than 3.1 Å. The blue circles represent the (Au,Ag) positions, which incorporate Ag.

Figure 58. Indexation of the calaverite faces by Janner and Dam (1989) with four indices according to the crystal model of Goldschmidt et al. (1931). The colors indicate the two twin components.

Figure 59. The average melilite layer structure with general composition $X_2T1T2_2O_7$ viewed along the normal to the layers (a) and in the perpendicular direction (b). X atoms are violet. The blue T2 tetrahedra always form bow tie whereas the yellow T1 tetrahedra are always surrounded by four T2 tetrahedra.

Figure 60. (a) Representation of a layer portion of a natural melilite with an incommensurately modulated structure and composition $(Ca,Na)_2(Al,Mg,Fe^{2+})[(Al,Si)SiO_7]$. The black T1 tetrahedra are those surrounded with only six coordinated X–O distances and four T1–X distances. (b) *t*-plot of the T1–X (Mg-Ca) distances. Two zones can be distinguished, one with $t \cong ½$ where 8 X atoms (violet) can be found in the vicinity of T1

(yellow) with distances shorter than 4.0 Å and $t \cong 0$ or 1 where 4 X can be found within the same limit.

Figure 61. (a) HR TEM diffraction pattern of icosahedral QC $Al_{63}Cu_{24}Fe_{13}$ with ten-fold symmetry. (b) See text for the explanation of the plot.

Figure 62. (a) Iridescent "labradorite", a plagioclase feldspar with composition $Ca_xNa_{1-x}Al_{1+x}Si_{3-x}O_8$. (b) Schematic representation of the main and satellite reflections based on Boysen and Kek (2015) data.

Figure 63. Schematic model of the labradorite structure with two different types of domains as proposed by Boysen and Kek (2015). The large domains D_i are linked to the s-satellites and also to the iridescent property whereas the smaller domains are linked to the e-satellites.

Table captions

Table 1. Five most structurally complex minerals and information-based parameters of their complexity.

Table 2. Sulfosalt species characterized by boxwork structure.

Table 3. Information-based complexity parameters for selected sulfosalts.

2277 **Table 1**. Five most structurally complex minerals and information-based parameters of their complexity

Mineral name	Chemical composition	G	v [atoms]	$^{str}I_G$ [bits/atom]	$^{str}I_{G,total}$ [bits/cell]	ρ_{inf} [bits Å^{-3}]	Ref.
Ewingite	$Mg_8Ca_8[(UO_2)_{24}(CO_3)_{30}O_4(OH)_{12}(H_2O)_8]\cdot 130H_2$	$I4_1/$	3088	7.603	23477.507	0.793	1
Morrisonite	$Ca_{11}[As^{3+}V^{4+}{}_2V^{5+}{}_{10}As^{5+}{}_6O_{51}]_2\cdot 78H_2O$	$P2_1/$	1576	8.622	13588.354	0.791	2
Ilmajokite	$Na_{11}KBaCe_2Ti_{12}Si_{37.5}O_{94}(OH)_{31}\cdot 29H_2O$	$C2/c$	1416	8.468	11990.129	0.730	3
Paulingite-(Ca)	$Ca_5[Al_{10}Si_{32}O_{84}]\cdot 34H_2O$	$Im\bar{3}$	1988	5.730	11590.532	0.535	4
Fantappieite	$[Na_{99}Ca_{33}]_{\Sigma=132}[Si_{99}Al_{99}O_{396}](SO_4)_{33}\cdot 6H_2O$	$P\bar{3}$	839	7.285	6111.824	0.488	5

2278 References: (1) Olds et al. 2017; (2) Kampf et al. 2016; (3) Zolotarev et al. 2020; (4) Lengauer et al. 1997; (5) Cámara et al. 2010.

2279

Table 2 – Sulfosalt species characterized by boxwork structure.

Mineral	Chemical formula	*a* (Å)	*b* (Å)	*c* (Å)	β (°)	*V* (Å^3)	s.g.	Ref.
Chovanite	$Pb_{28}Sb_{30}S_{72}O$	34.05	8.20	48.08	106.3	12892	$P2_1/c$	[1]
Marrucciite	$Hg_3Pb_{16}Sb_{18}S_{46}$	48.32	4.12	24.06	118.8	4192	$C2/m$	[2]
Neyite	$Ag_2Cu_6Pb_{25}Bi_{26}S_{68}$	37.53	4.07	43.70	108.8	6319	$C2/m$	[3]
Pellouxite	$(Cu,Ag)_2Pb_{21}Sb_{23}S_{55}ClO$	55.82	4.09	24.13	113.1	5065	$C2/m$	[4]
Pillaite	$Pb_9Sb_{10}S_{23}ClO_{0.5}$	49.49	4.13	21.83	99.6	4394	$C2/m$	[5]
Rouxelite	$Cu_2HgPb_{22}Sb_{28}S_{64}(O,S)_2$	43.11	4.06	37.87	117.4	5887	$C2/m$	[6]
Scainiite	$Pb_{14}Sb_{30}S_{54}O_5$	52.00	8.15	24.31	104.1	9990	$C2/m$	[7]
Tazieffite	$Pb_{20}Cd_2(Bi,As)_{22}S_{50}Cl_{10}$	8.35	45.59	27.26	98.8	10257	$C2/c$	[8]
Vurroite	$Pb_{20}Sn_2(As,Bi)_{22}S_{54}Cl_6$	8.37	45.50	27.27	98.8	10265	$C2/c$	[9]

[1] Biagioni and Moëlo 2017; [2] Orlandi et al. 2007; [3] Makovicky et al. 2001; [4] Palvadeau et al. 2004; [5] Meerschaut et al. 2001; [6] Orlandi et al. 2005; [7] Moëlo et al. 2000; [8] Zelenski et al. 2009; [9] Pinto et al. 2008.

Table 3 – Information-based complexity parameters for selected sulfosalts.

Mineral	Chemical formula	v_1	v_2	${}^{chem}I_G$	${}^{str}I_G$	${}^{chem}I_{G,total}$	${}^{str}I_{G,total}$
Chovanite^{SS}	$Pb_{28}Sb_{30}S_{72}O$	66	132	1.526	6.044	100.709	797.860
Chovanite	$Pb_{28}Sb_{30}S_{72}O$	66	532	1.526	7.055	100.709	3753.410
Marrucciite^{SS}	$Hg_3Pb_{16}Sb_{18}S_{46}$	83	83	1.581	5.387	131.234	447.128
Meerschautite	$Ag_{5.5}Pb_{42.4}Sb_{45.1}S_{112}O_{0.8}$	411	414	1.595	7.693	655.636	3185.104
Neyite^{SS}	$Ag_2Cu_6Pb_{25}Bi_{26}S_{68}$	127	127	1.715	5.997	217.803	761.563
Parasterryite	$Ag_4Pb_{20}(Sb,As)_{24}S_{58}$	53	424	1.815	6.728	96.220	2852.638
Pellouxite^{SS}	$(Cu,Ag)_2Pb_{21}Sb_{23}S_{55}ClO$	103	104	1.712	5.700	167.772	592.846
Pillaite^{SS}	$Pb_9Sb_{10}S_{23}ClO_{0.5}$	87	88	1.643	5.459	142.958	480.430
Rouxelite^{SS}	$Cu_2HgPb_{22}Sb_{28}S_{64}(O,S)_2$	119	119	1.679	5.903	199.774	702.483
Scainiite	$Pb_{14}Sb_{30}S_{54}O_5$	76	206	1.242	6.182	94.416	1273.419
Sterryite	$CuAg_3Pb_{19}Sb_{22}(As)_2S_{56}$	103	424	1.692	6.728	172.561	2852.638
Tazieffite	$Pb_{20}Cd_2As_{22}S_{50}Cl_{10}$	52	208	1.874	5.739	97.446	1193.691
Vurroite	$Pb_{20}Sn_2Bi_{22}S_{54}Cl_6$	52	208	1.770	5.739	92.015	1193.691

v_1 – number of atoms in the chemical formula; v_2 – number of atoms within the reduced unit cell; ${}^{chem}I_G$ – the amount of chemical Shannon information per atom (bits/atom); ${}^{str}I_G$ – the amount of structural Shannon information per atom (bits/atom); ${}^{chem}I_{G,total}$ – the amount of chemical Shannon information per formula (bits/formula); ${}^{str}I_{G,total}$ – the amount of structural Shannon information per unit cell (bits/cell). ^{SS} = 4 Å sub-structure.

Figure 1

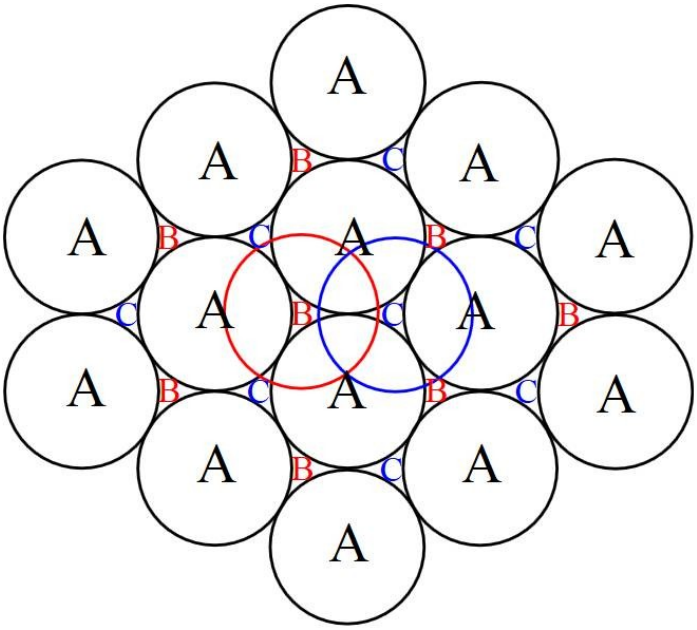

Figure 2

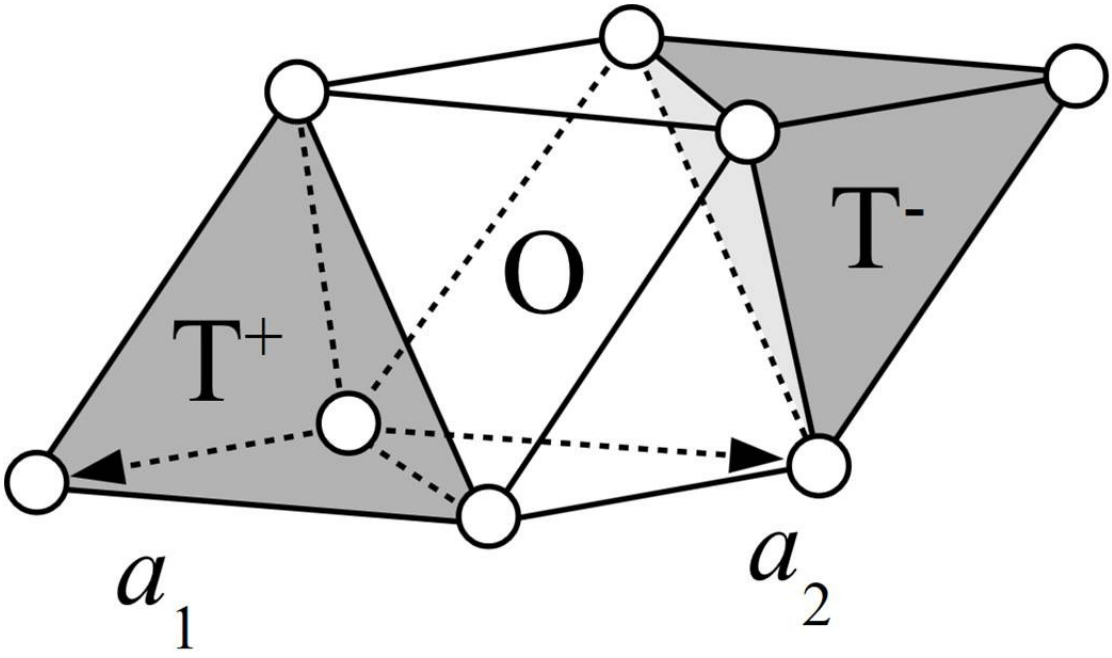

Figure 3

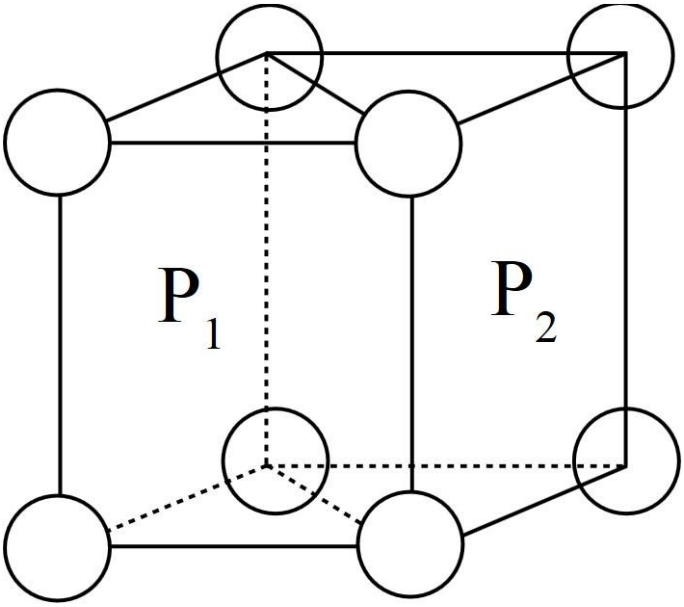

Figure 4

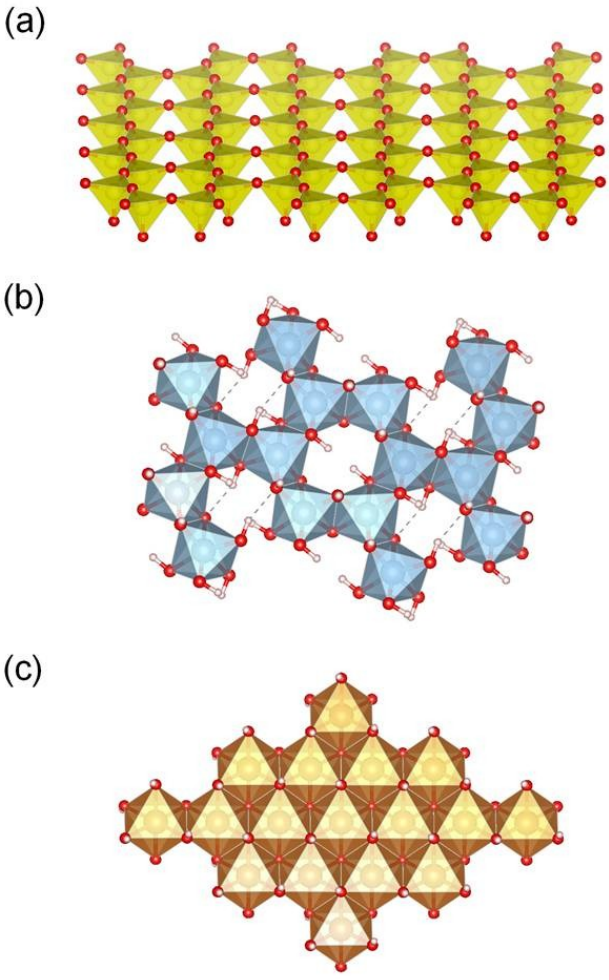

Figure 5

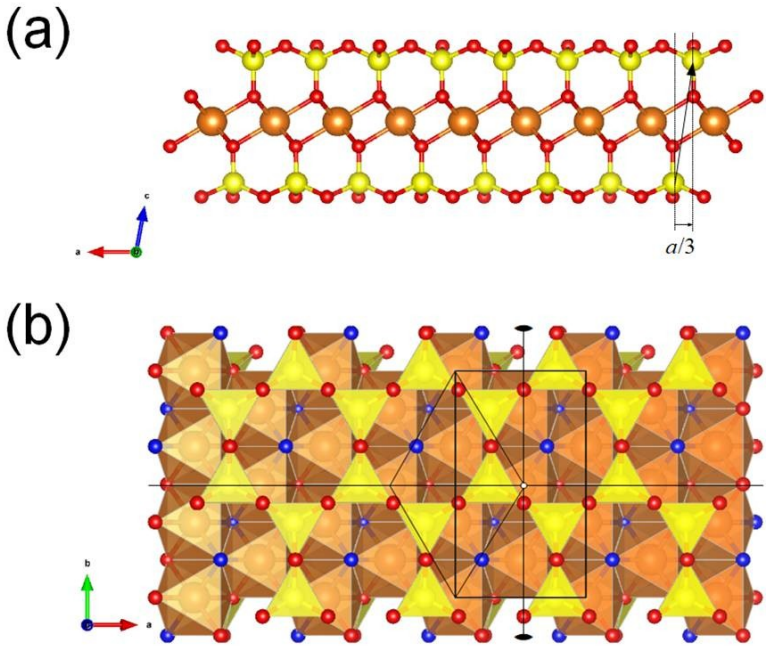

Figure 6

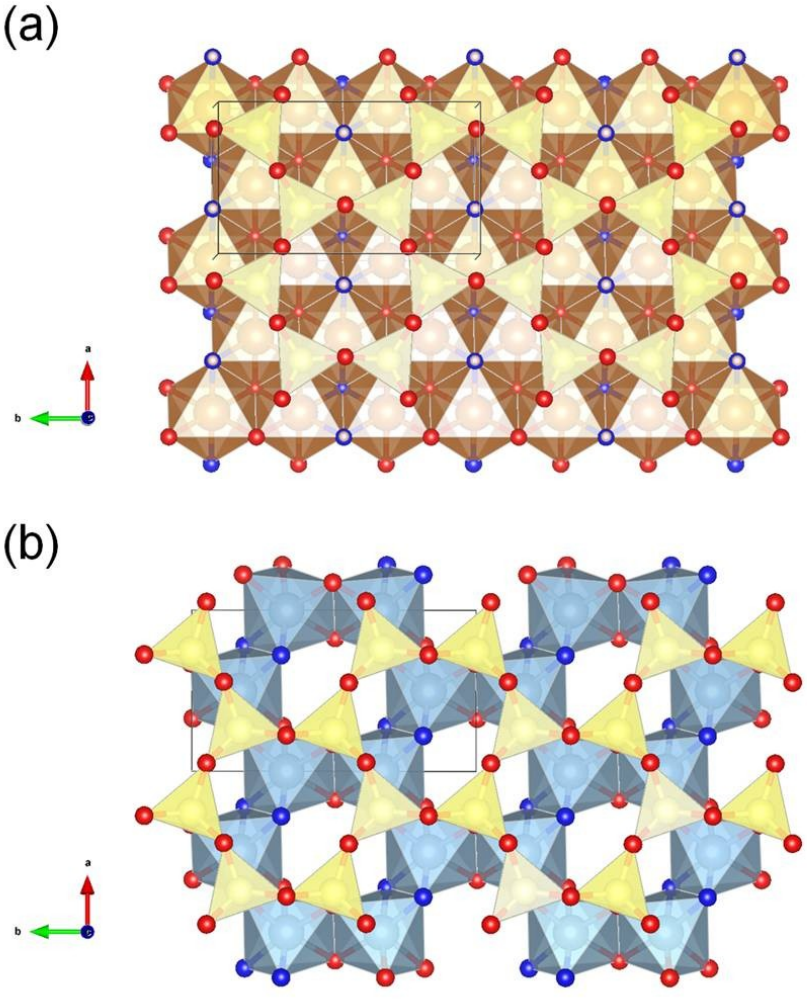

Figure 7

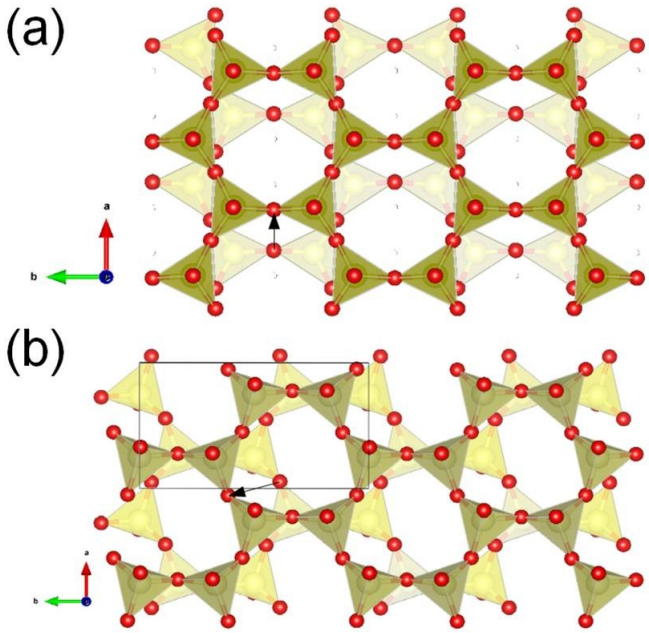

Figure 8

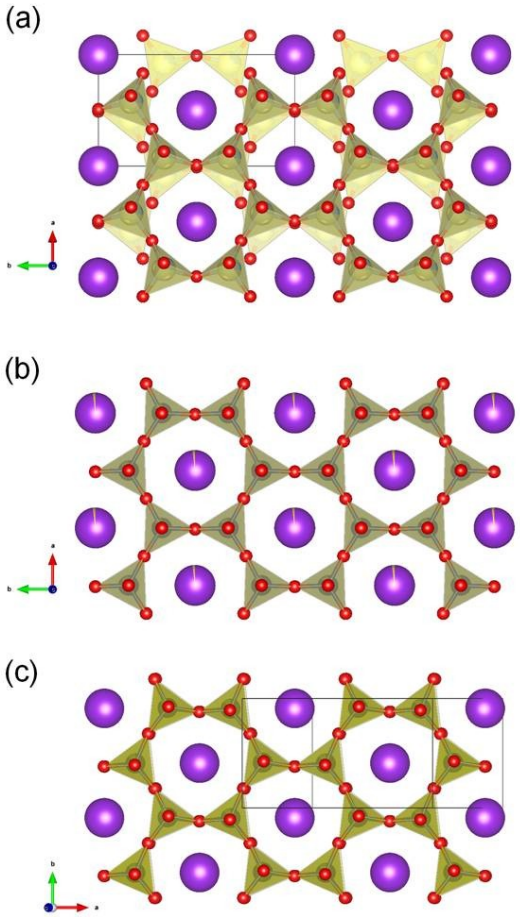

Figure 9

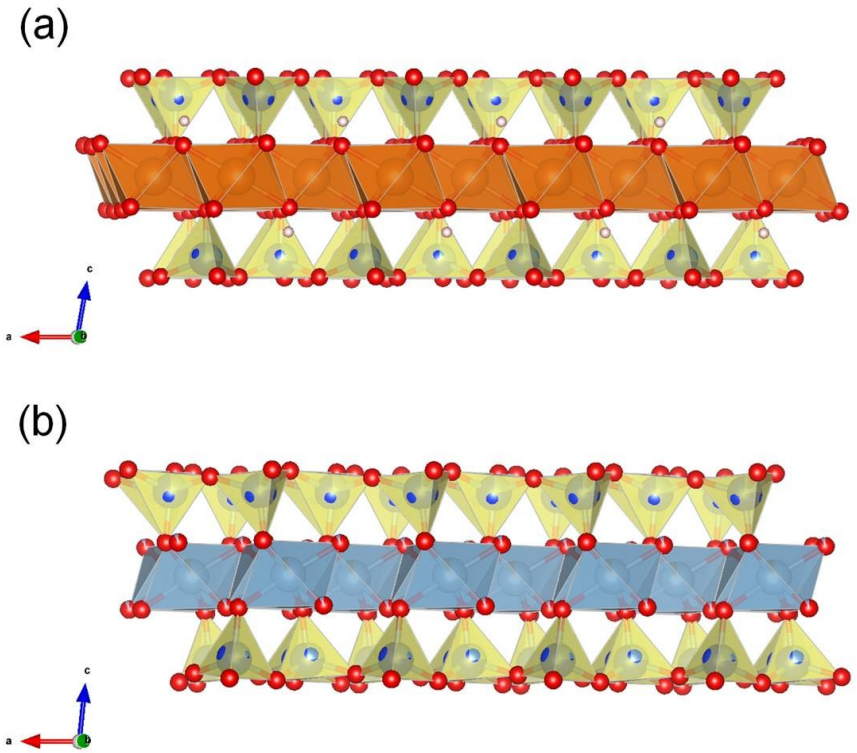

Figure 10

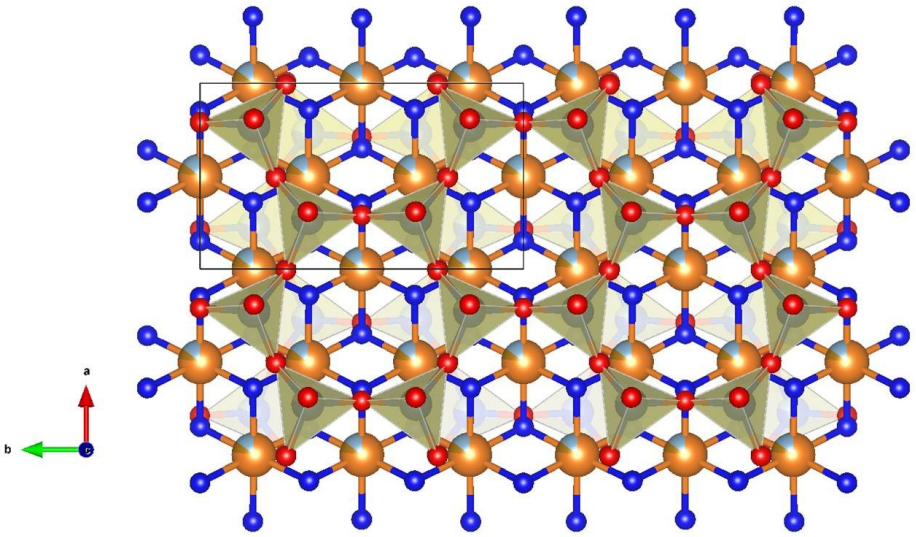

Figure 11

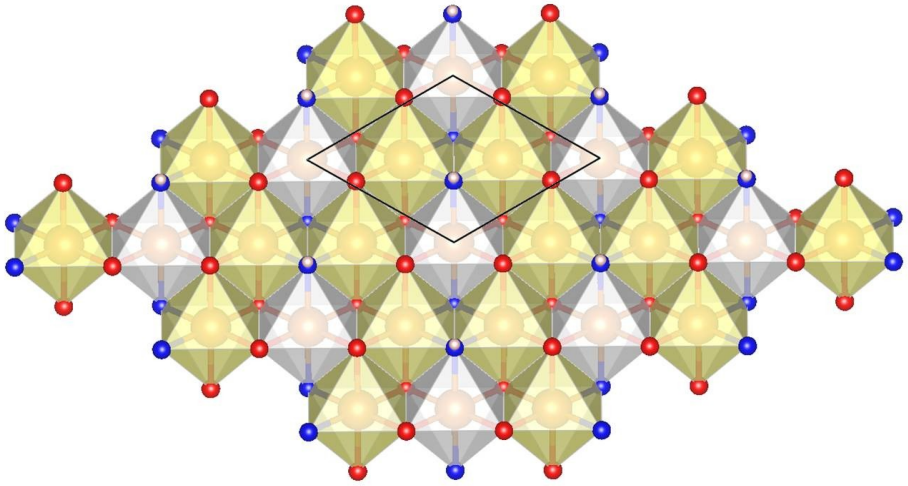

Figure 12

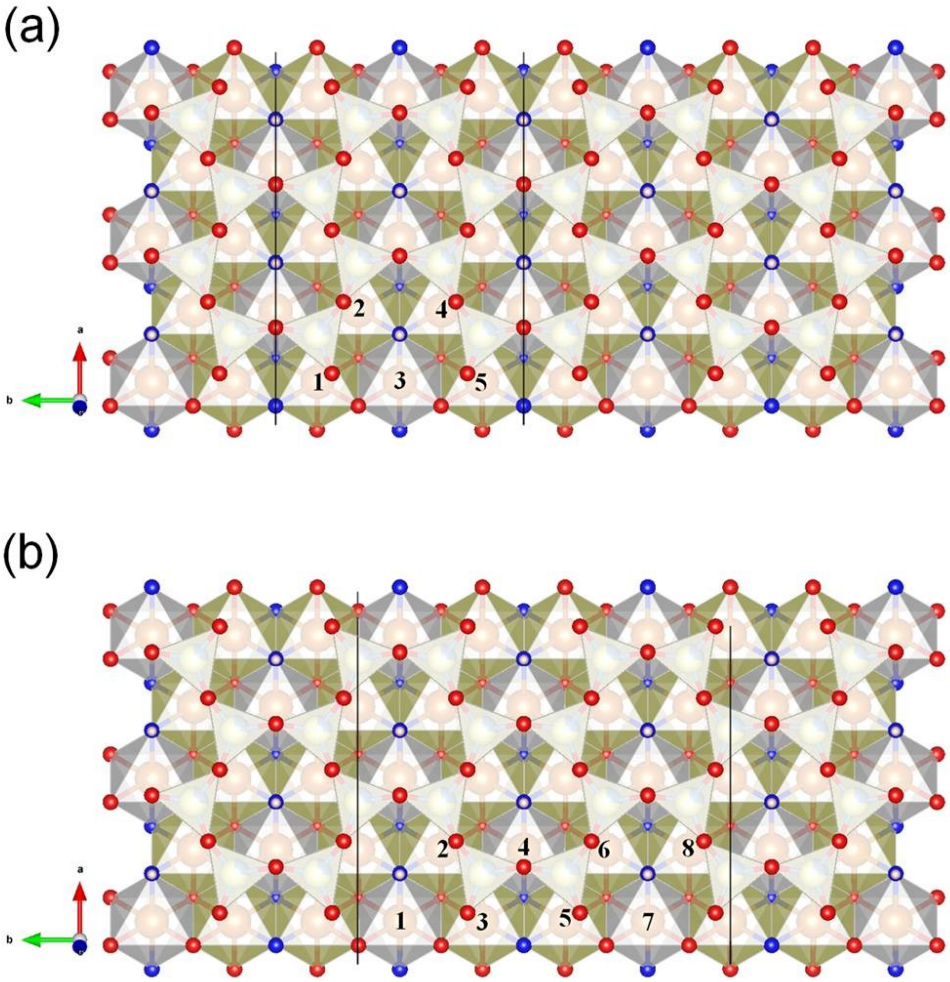

Figure 13

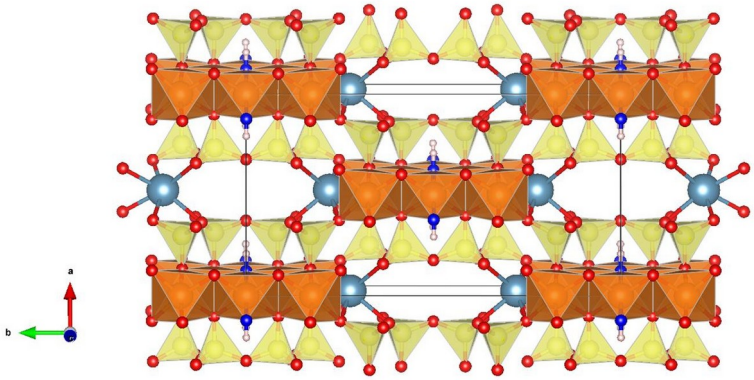

Figure 14

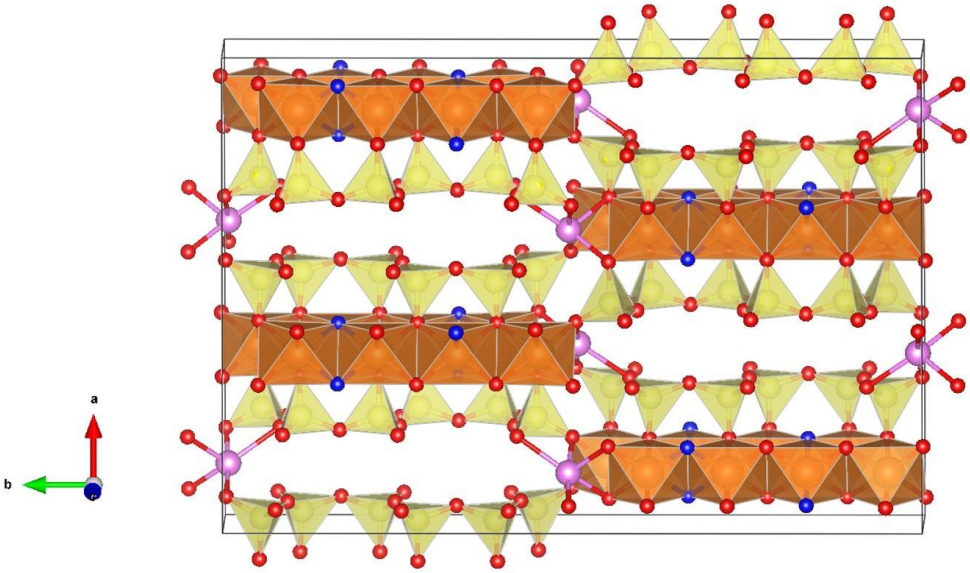

Figure 15

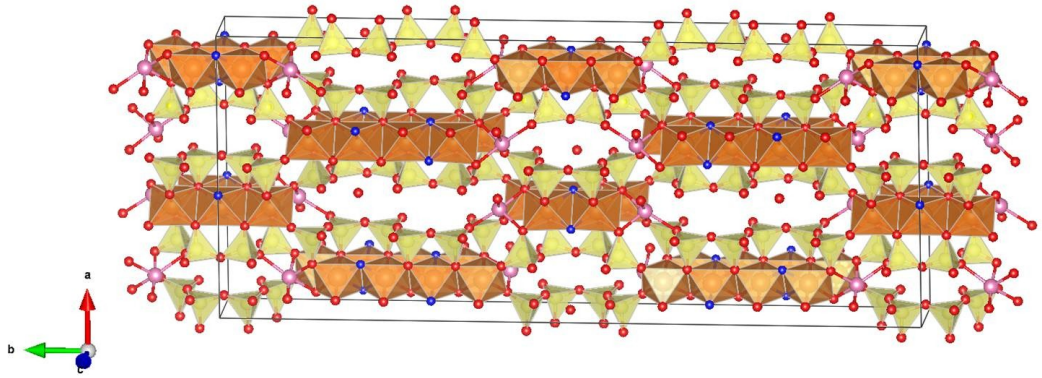

Figure 16

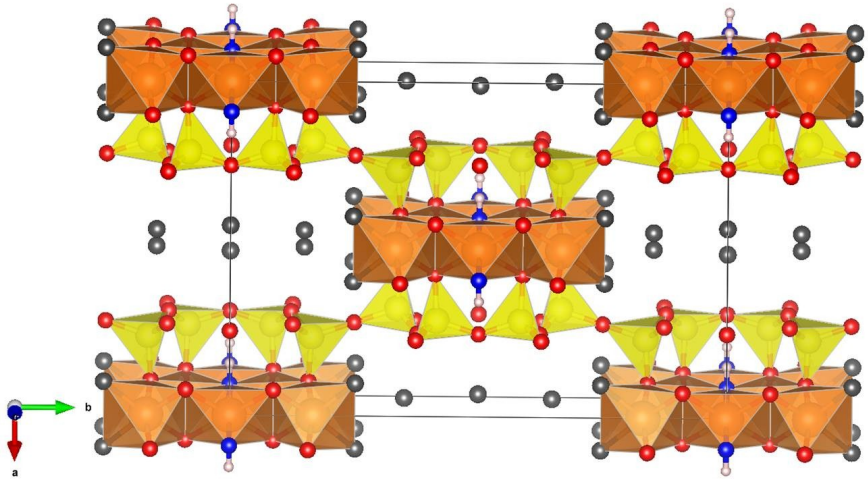

Figure 17

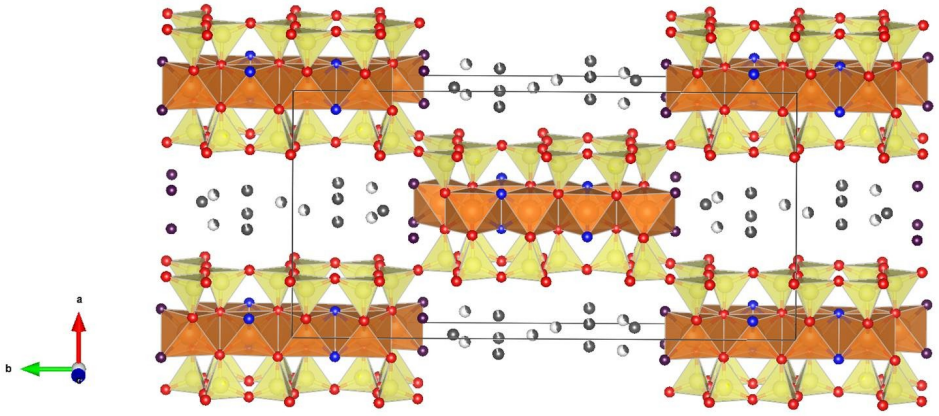

Figure 18

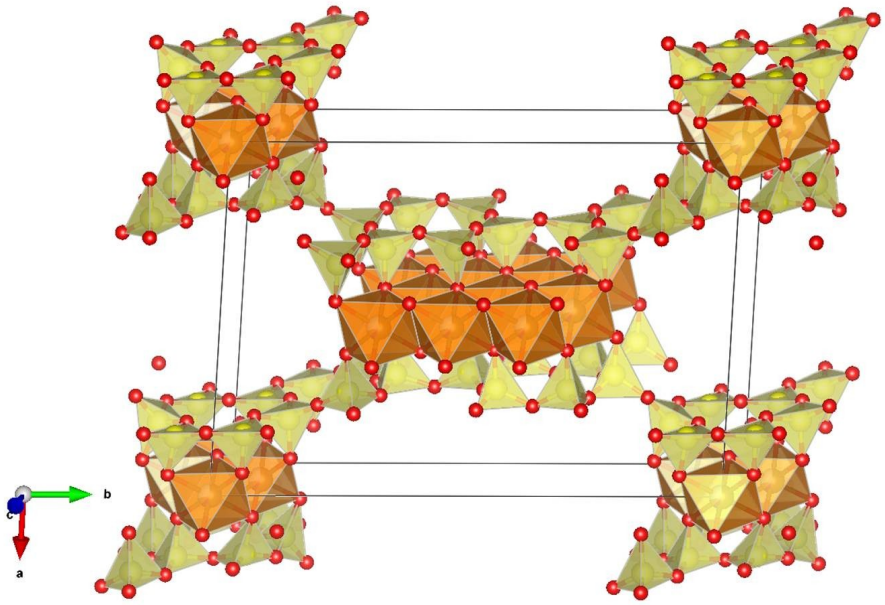

Figure 19

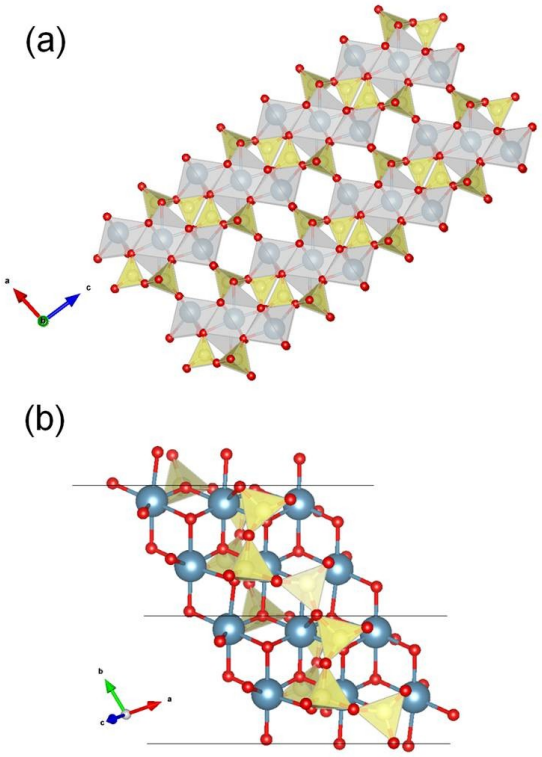

Figure 20

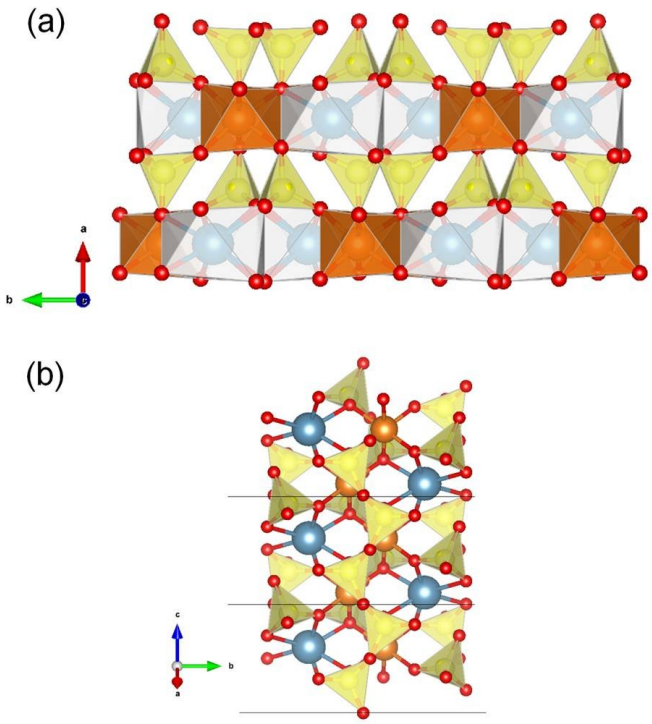

Figure 21

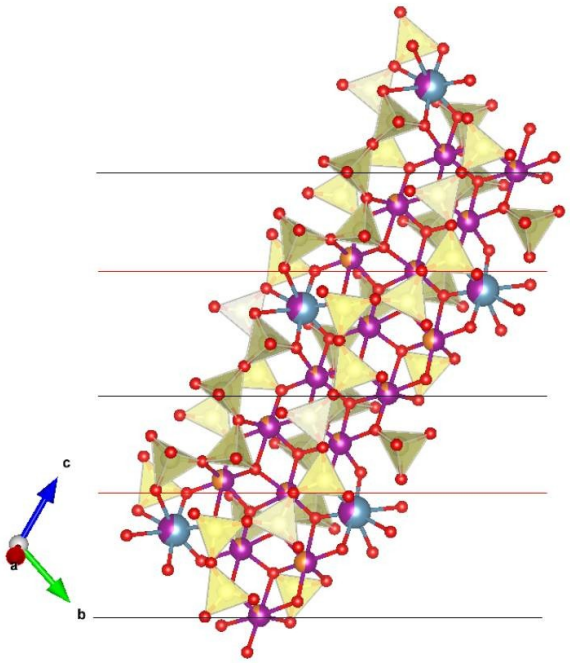

Figure 22

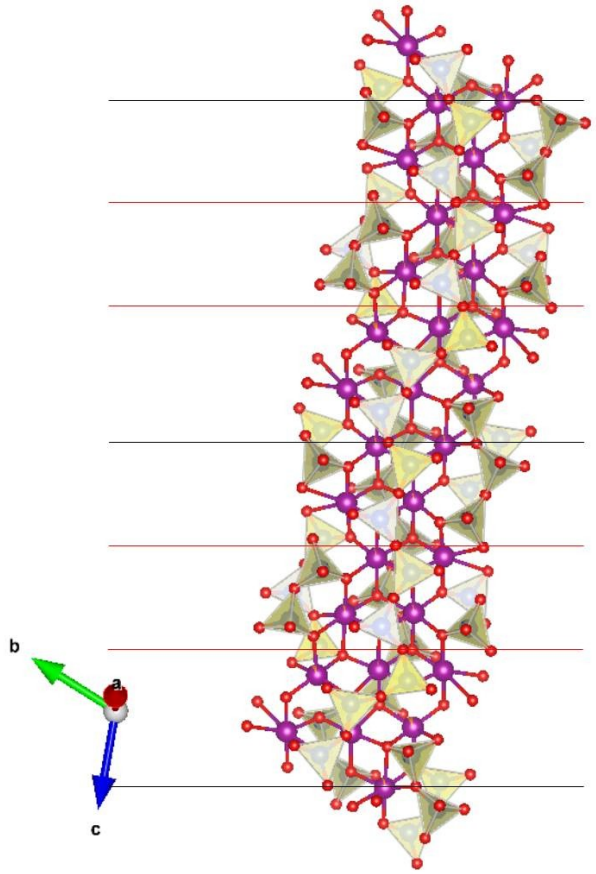

Figure 23

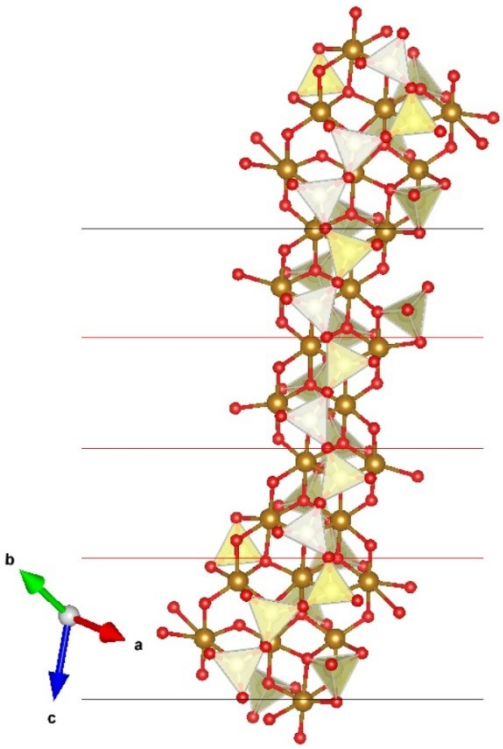

Figure 24

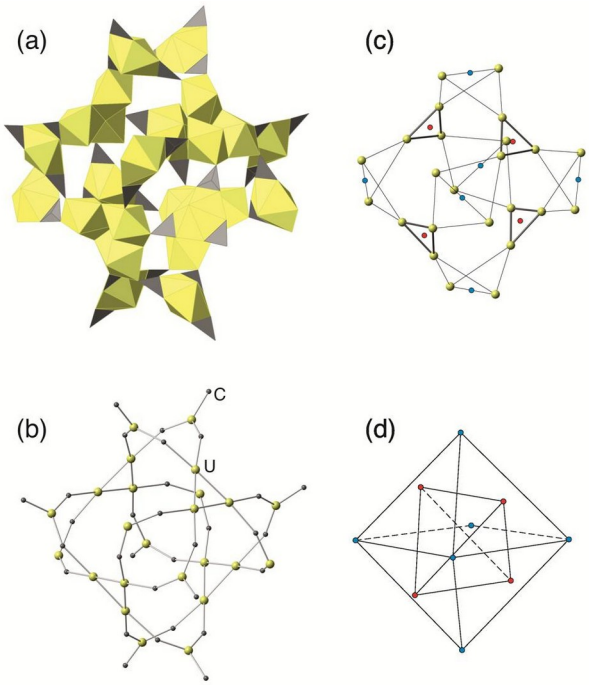

Figure 25

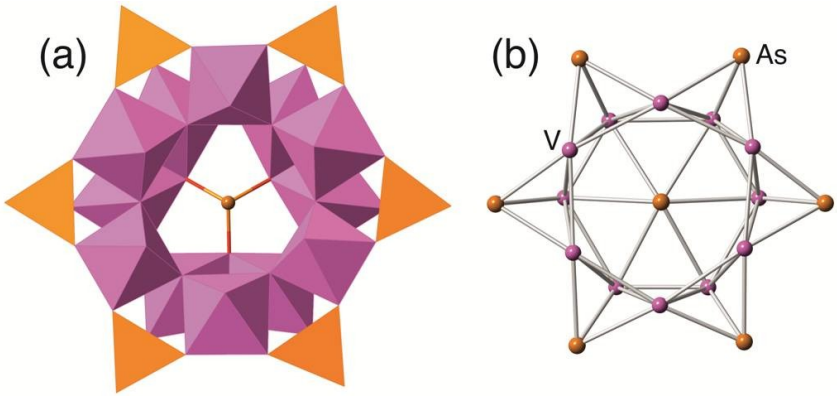

Figure 26

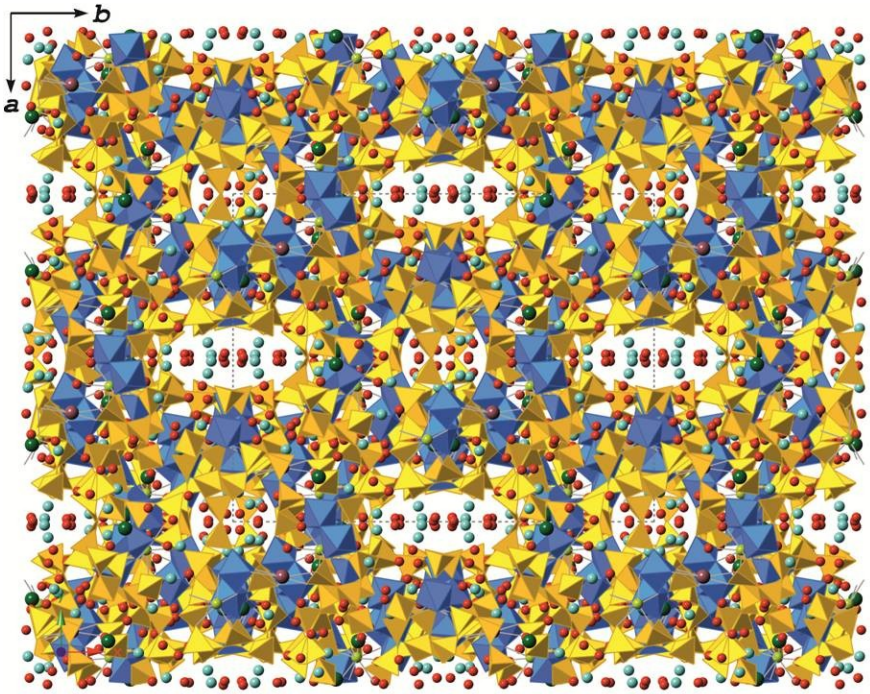

Figure 27

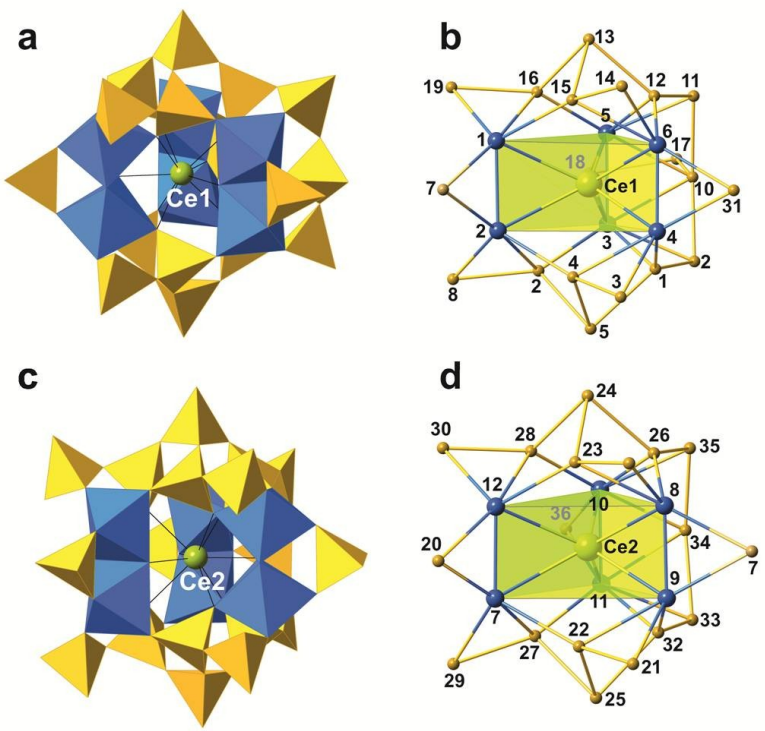

Figure 28

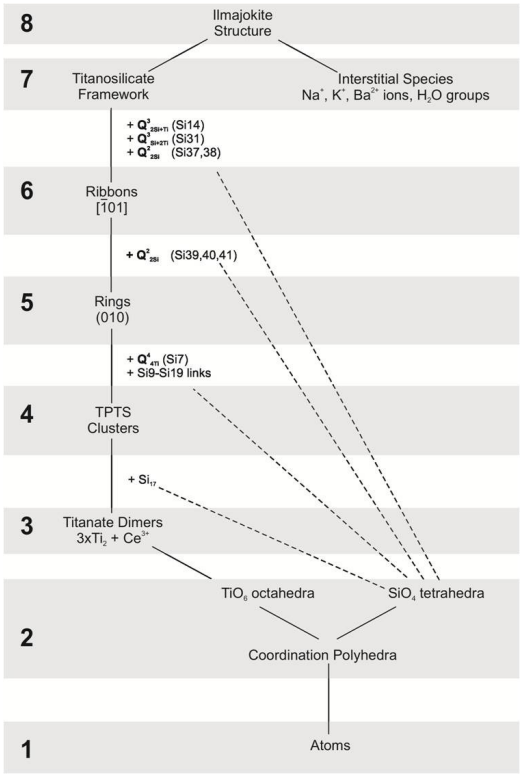

Figure 29

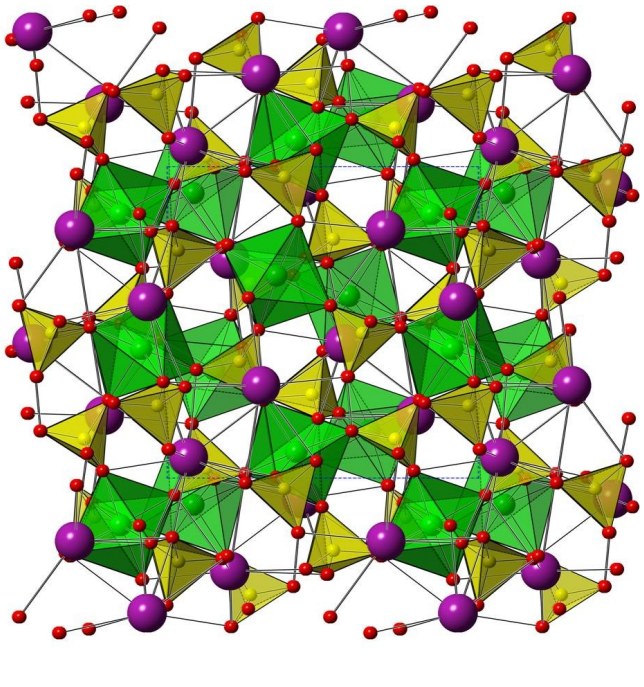

Figure 30

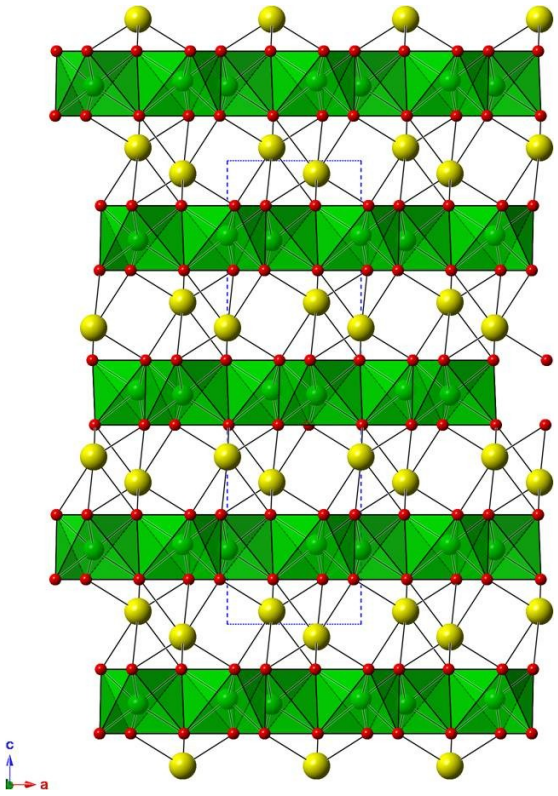

Figure 31

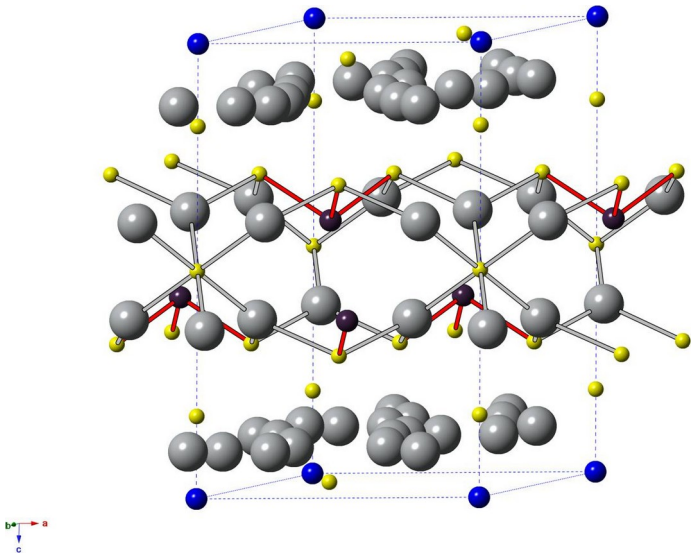

Figure 32

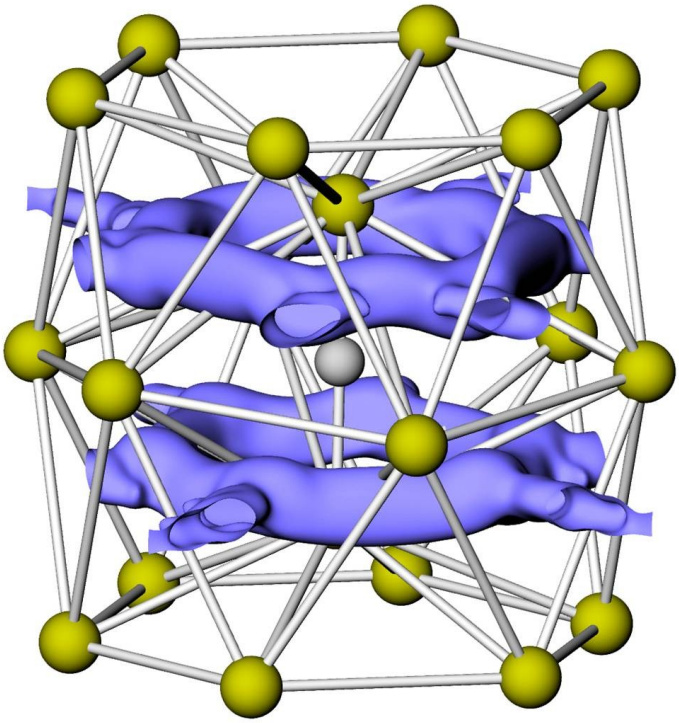

Figure 33

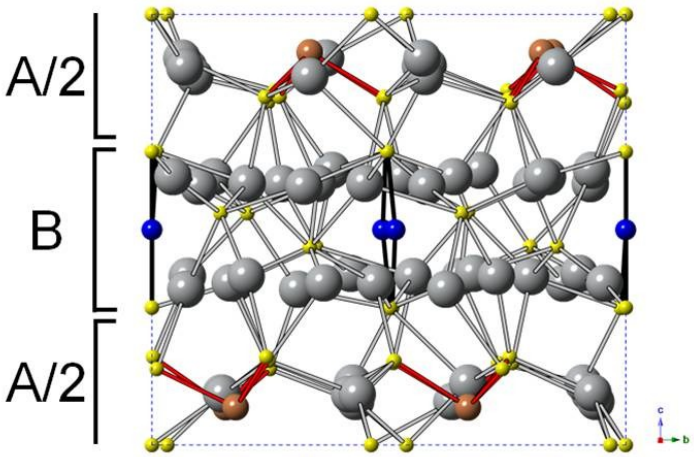

Figure 34

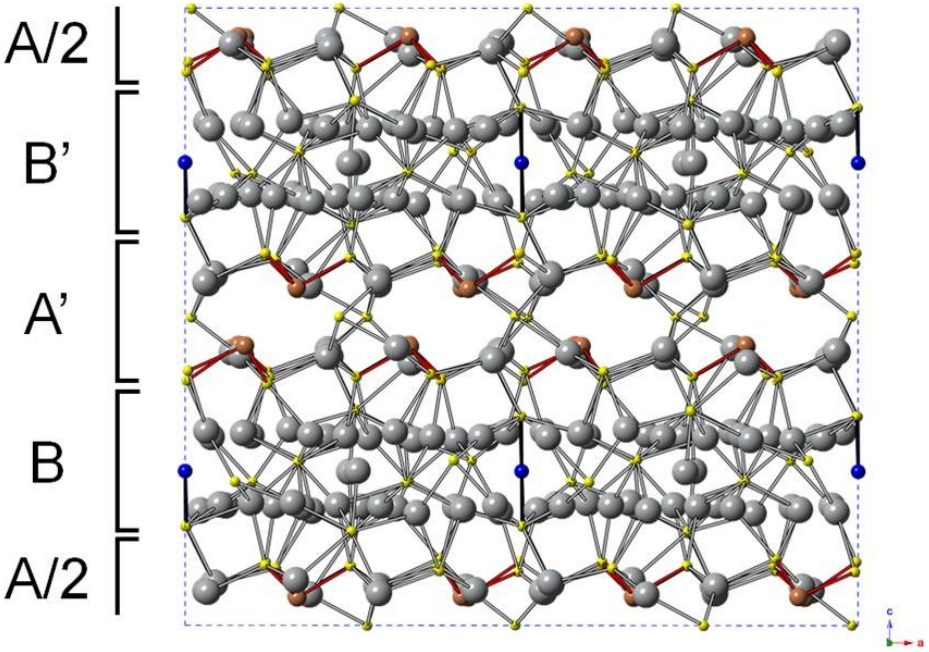

Figure 35

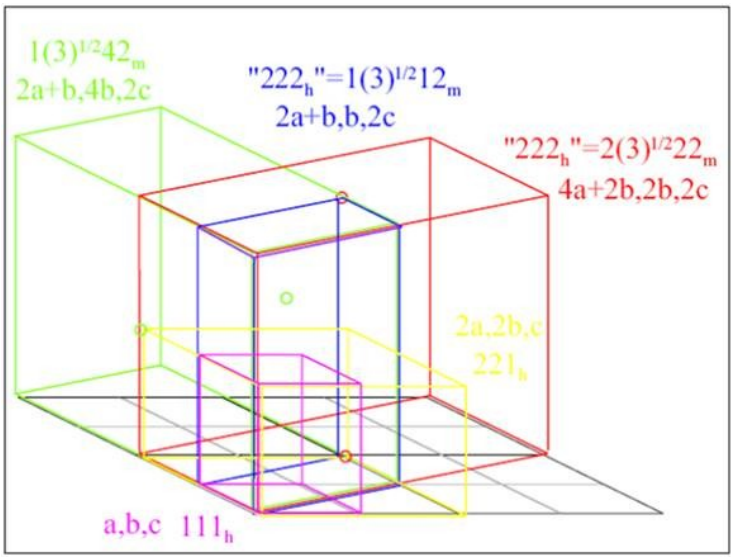

Figure 36

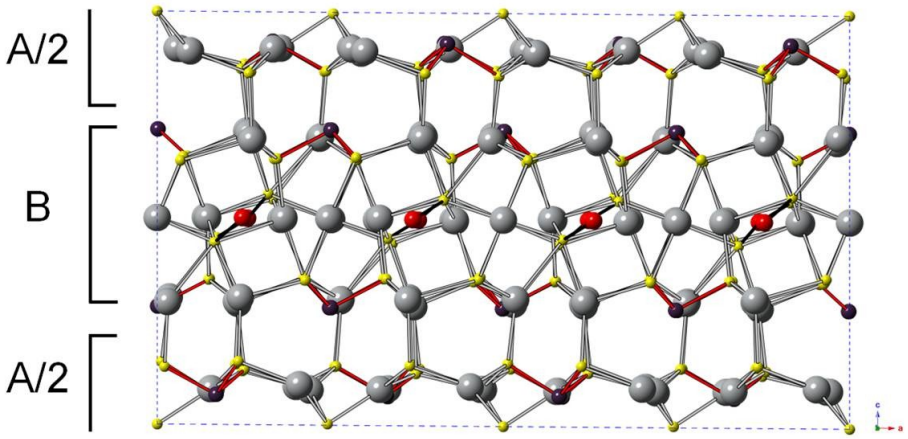

Figure 37

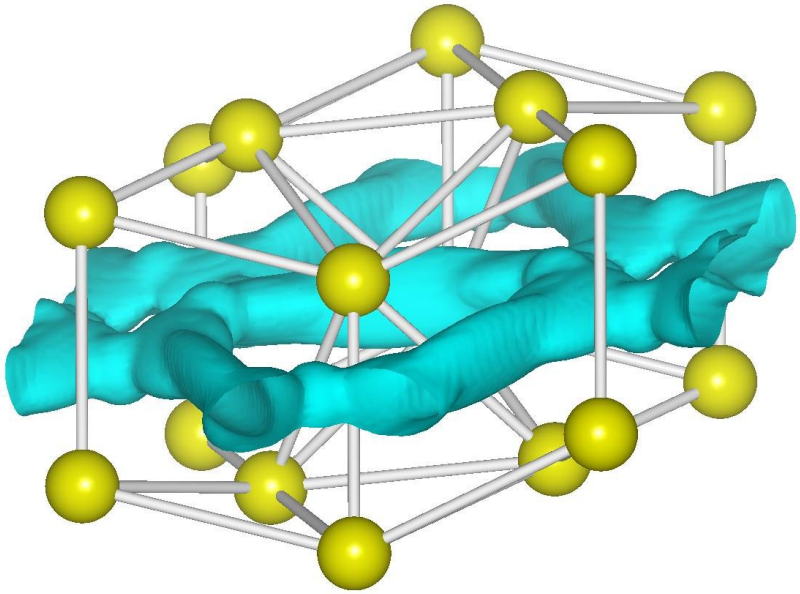

Figure 38

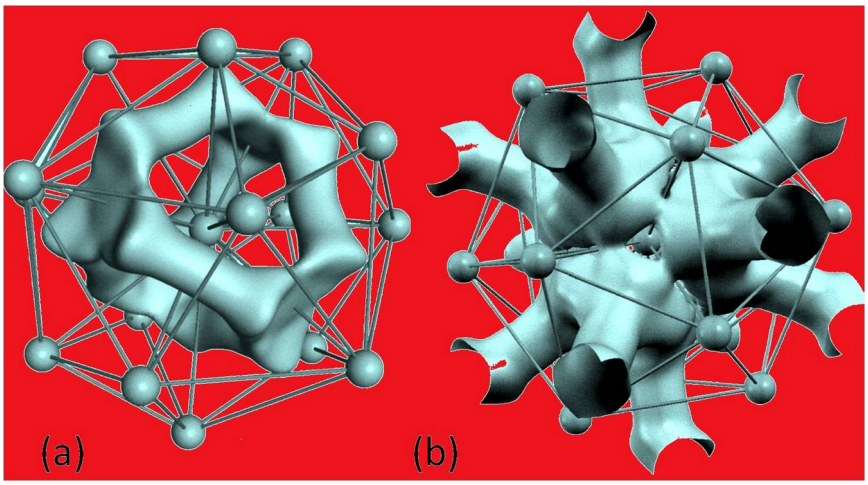

Figure 39

Figure 40

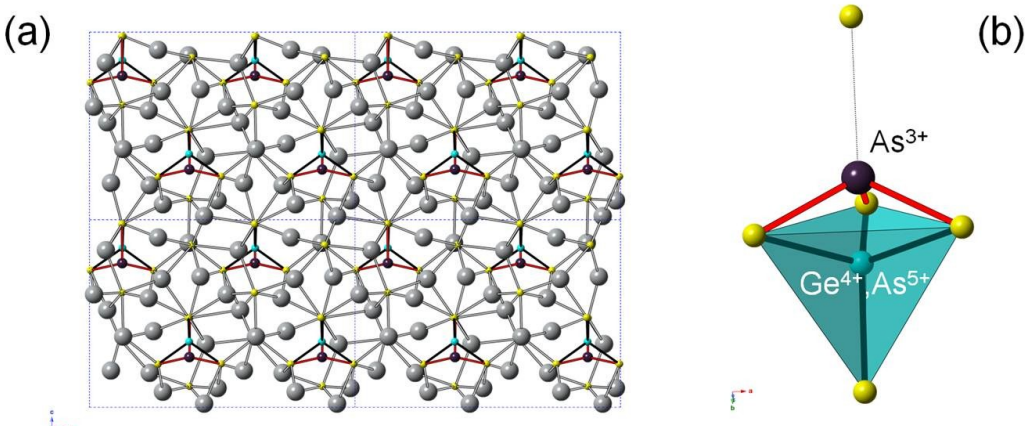

Figure 41

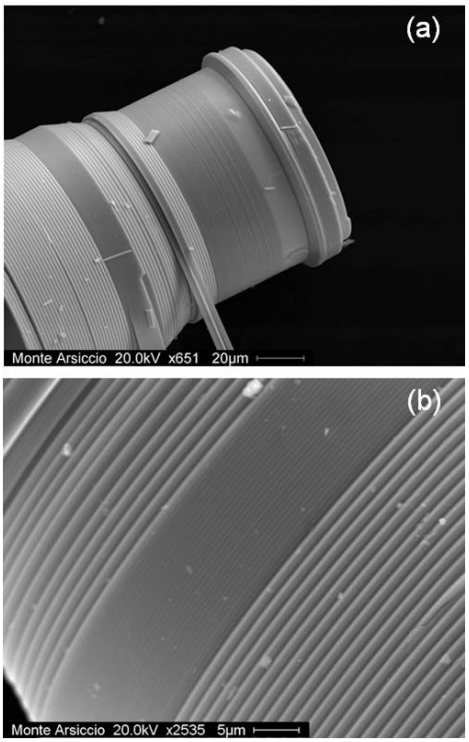

Figure 42

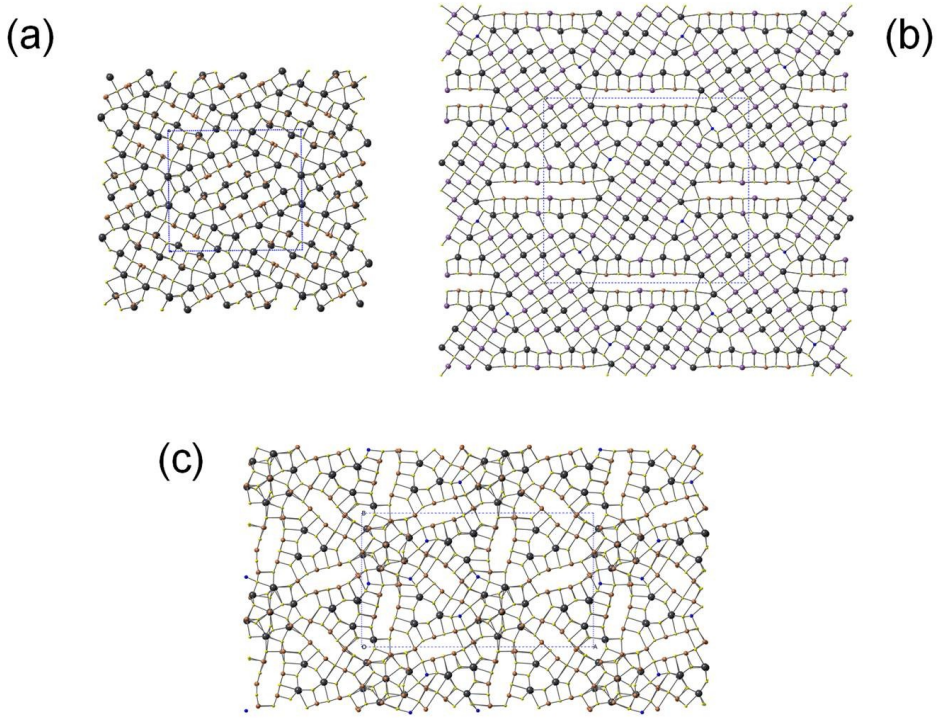

Figure 43

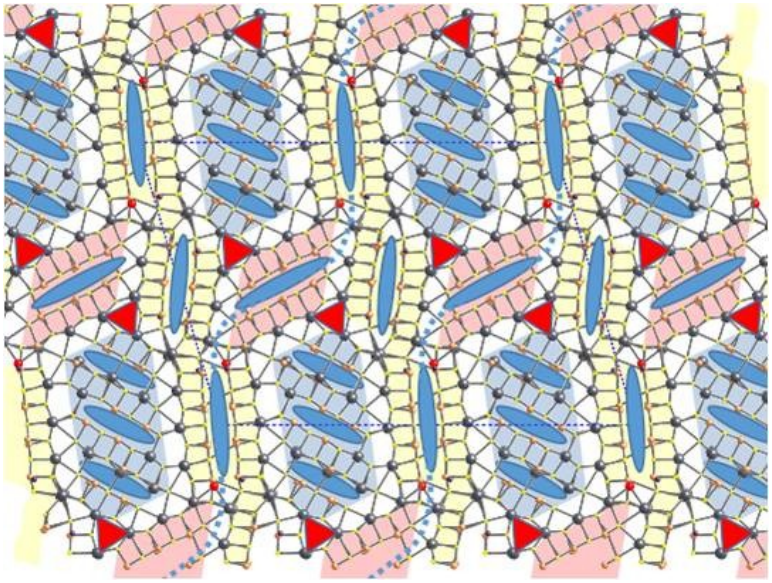

Figure 44

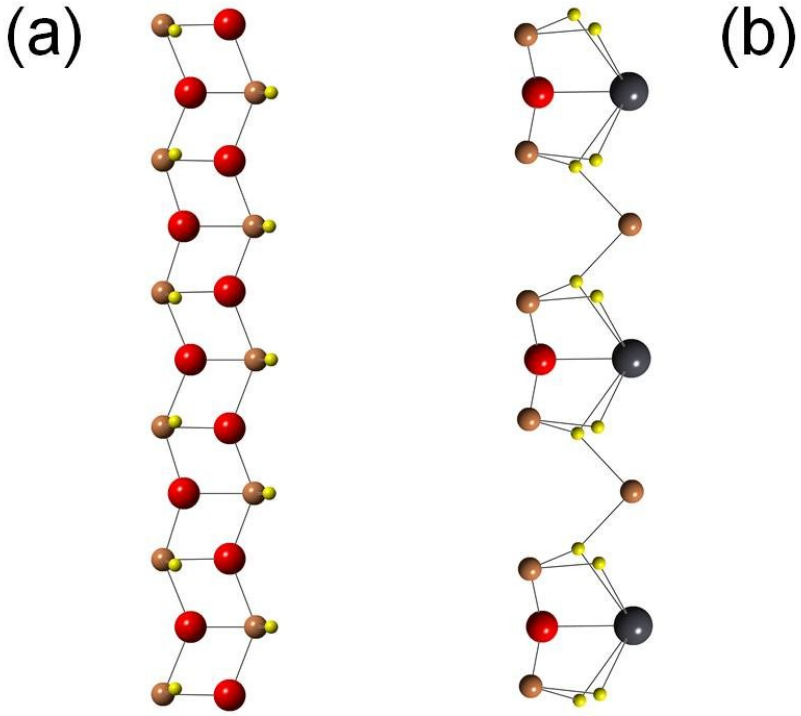

Figure 45

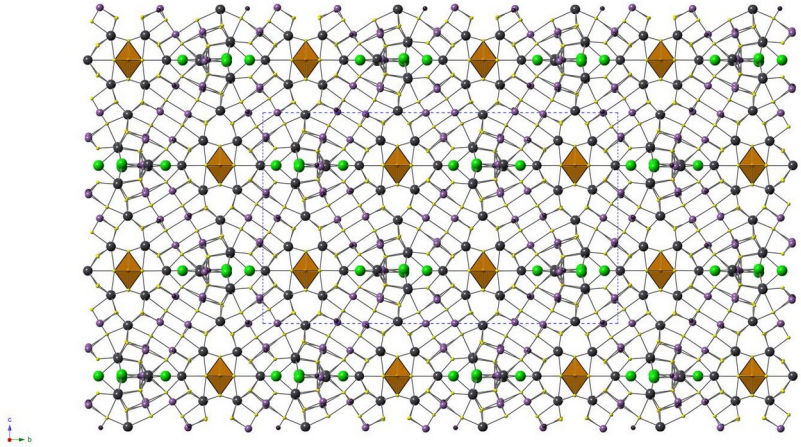

Figure 46

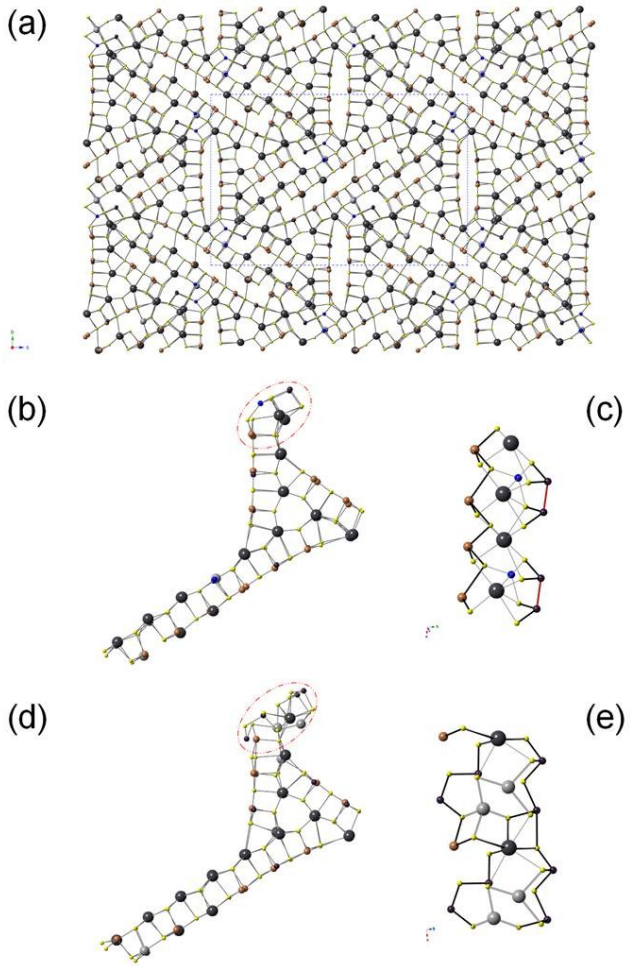

Figure 47

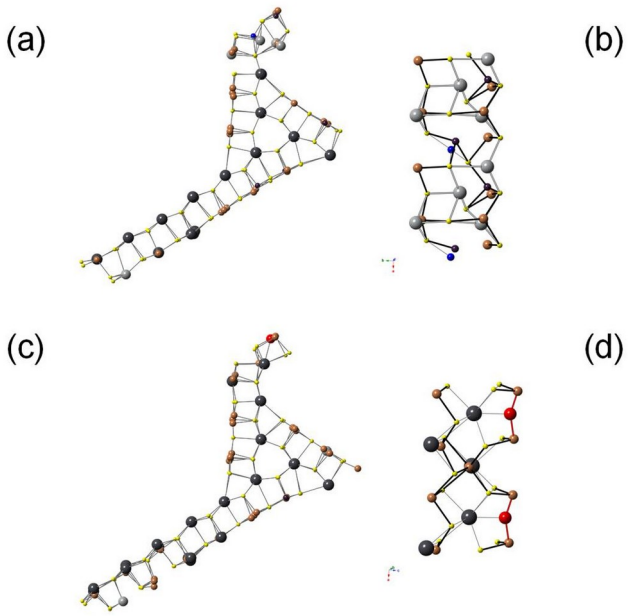

Figure 48

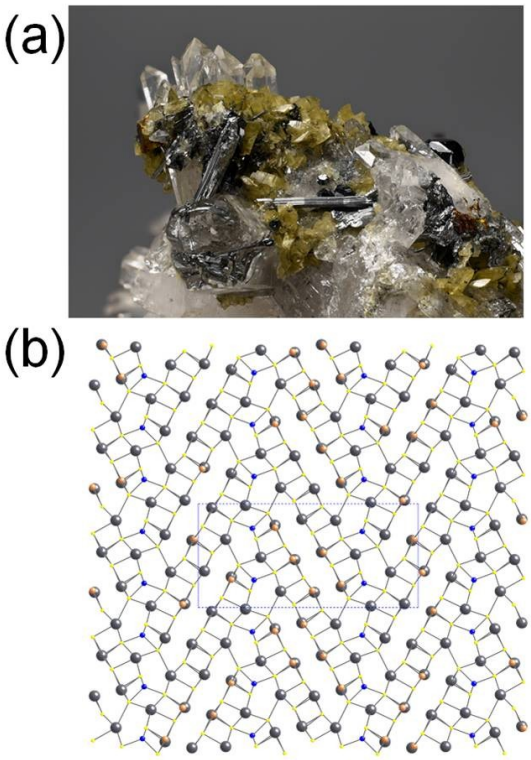

Figure 49

Figure 50

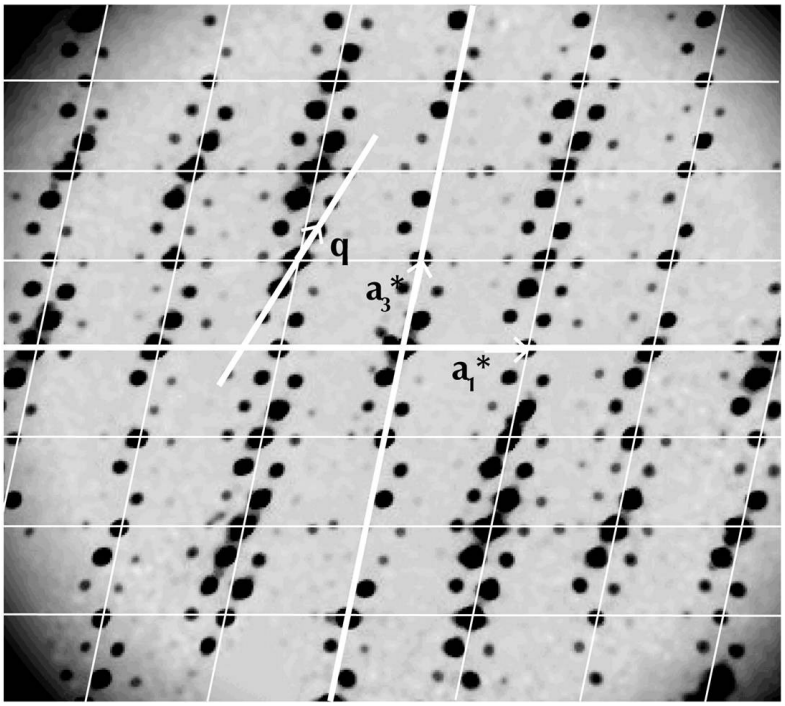

Figure 51

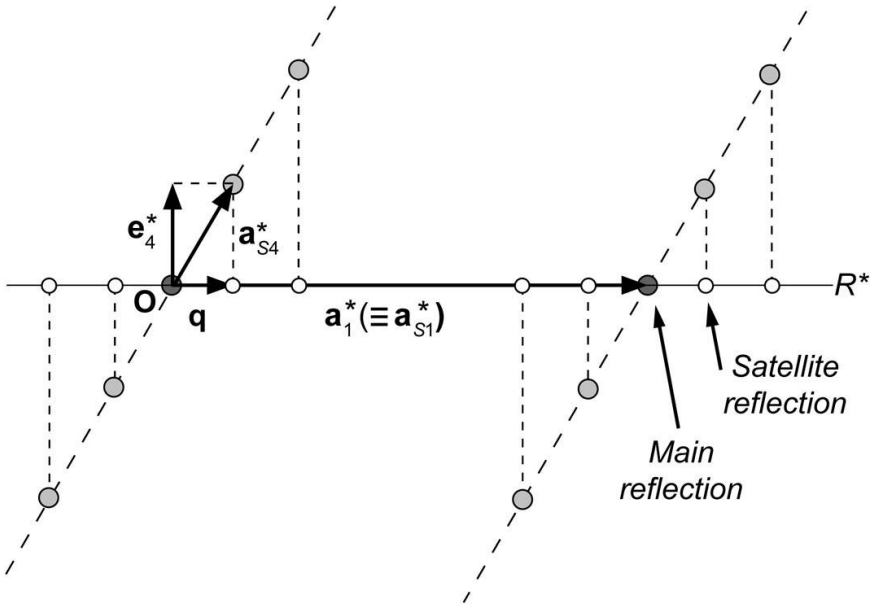

Figure 52

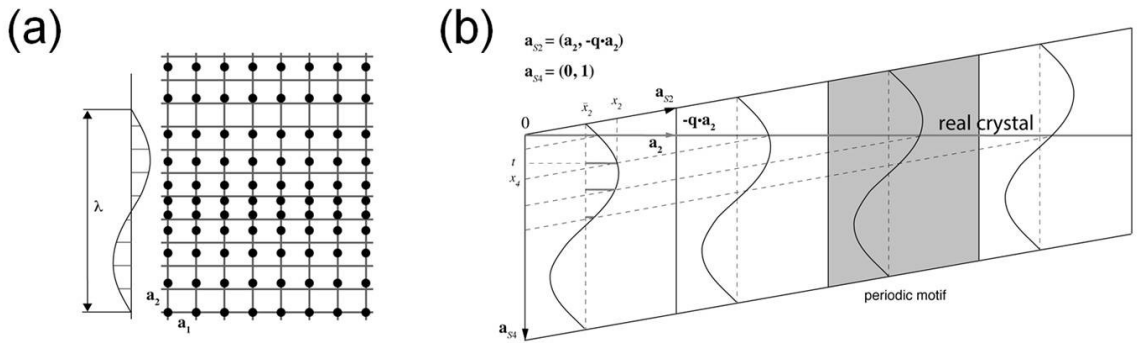

Figure 53

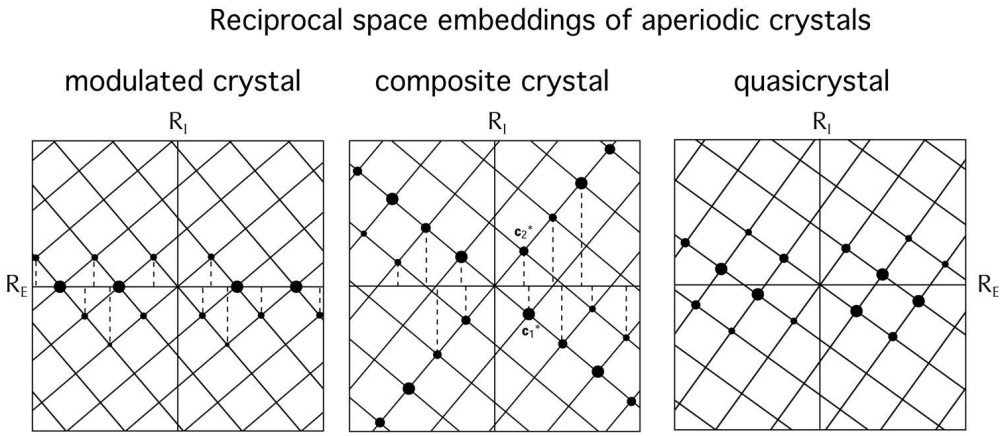

Figure 54

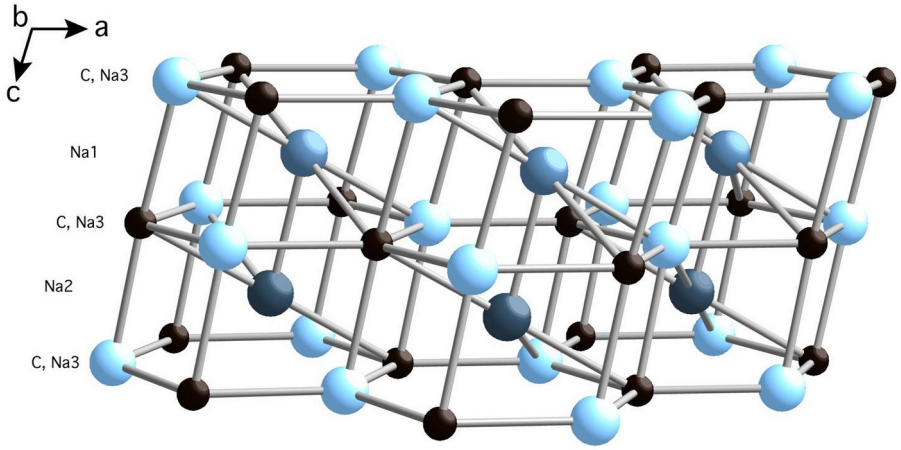

Figure 55

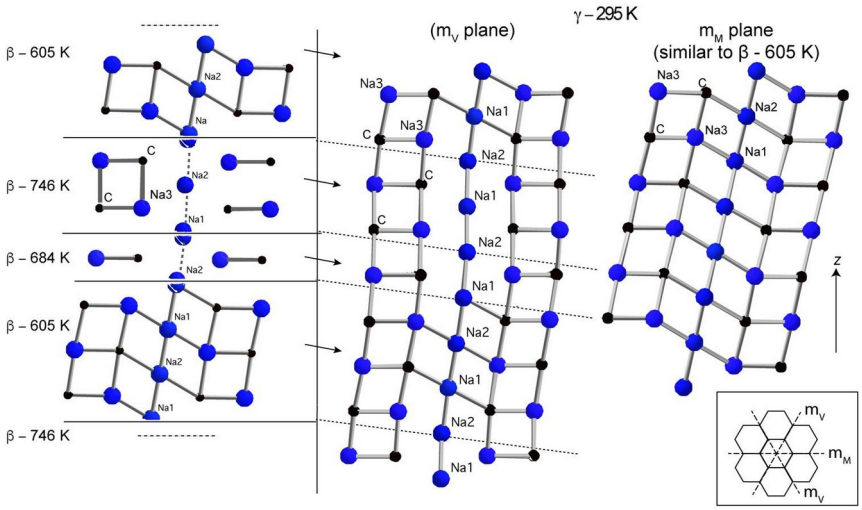

Figure 56

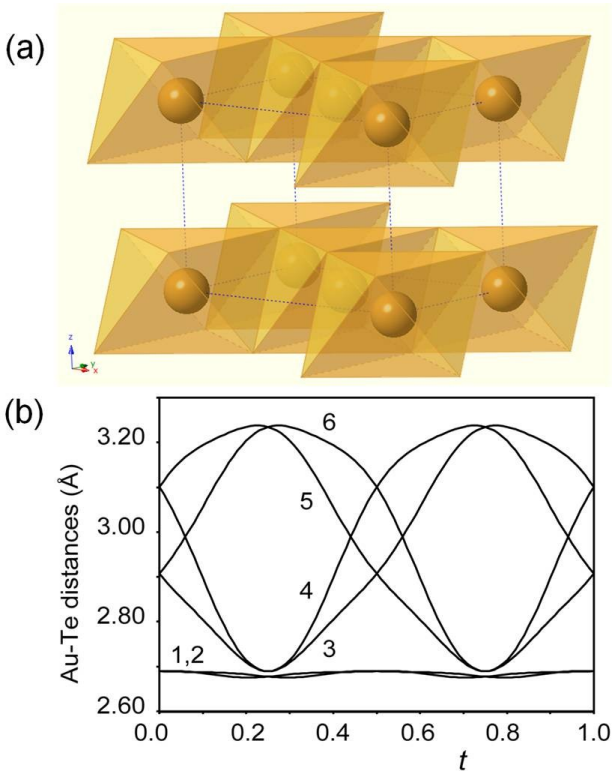

Figure 57

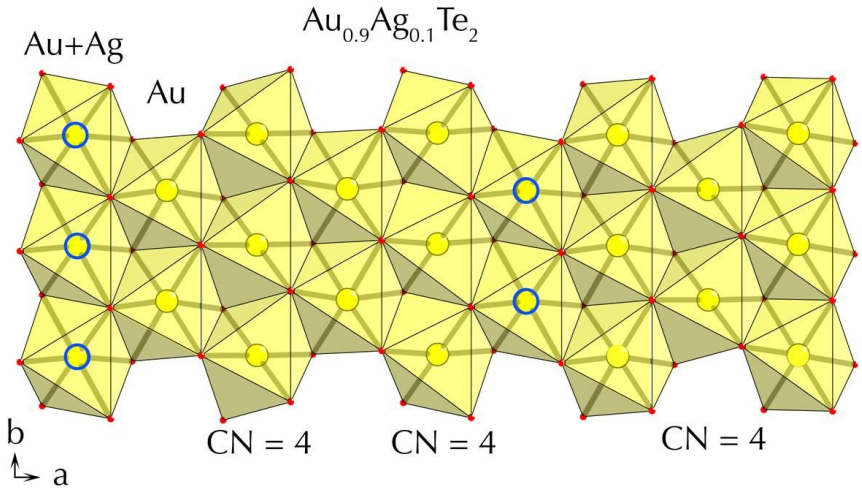

Figure 58

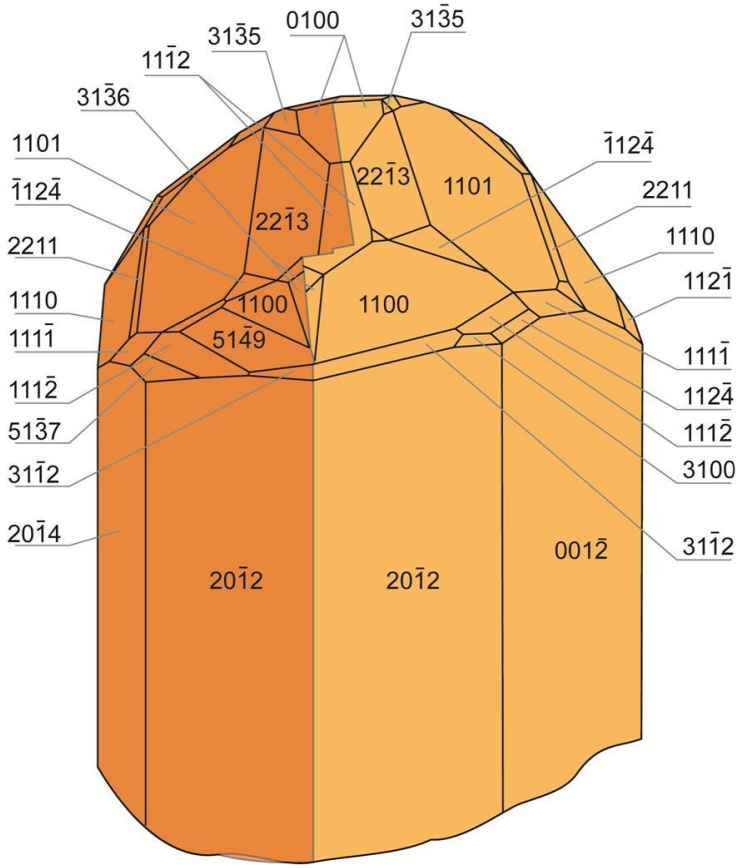

Figure 59

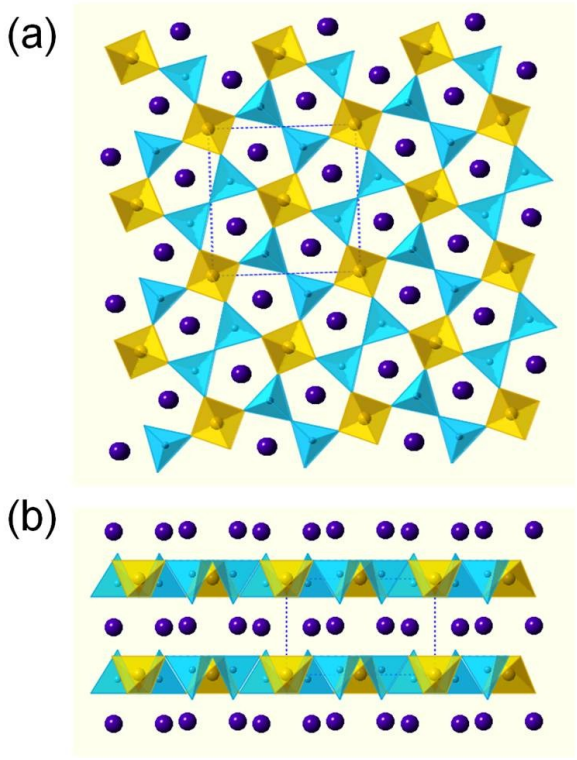
(a)
(b)

Figure 60

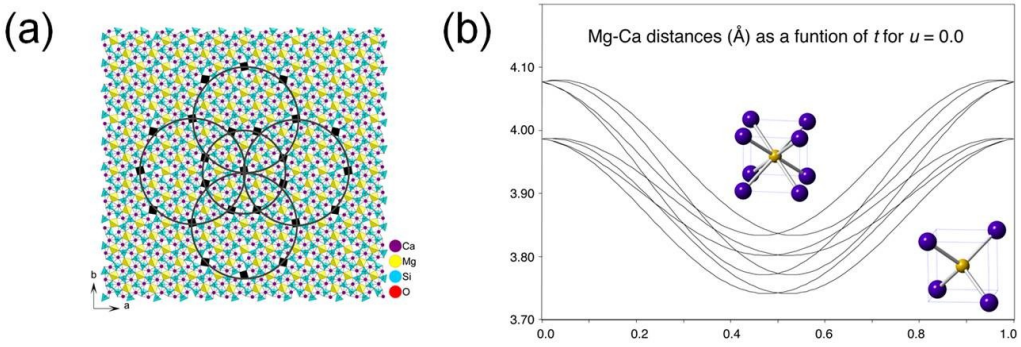
(a)
Ca
Mg
Si
O
b
a
(b)
Mg-Ca distances (Å) as a funtion of t for u = 0.0
4.10
4.00
3.90
3.80
3.70
0.0
0.2
0.4
0.6
0.8
1.0

Figure 61

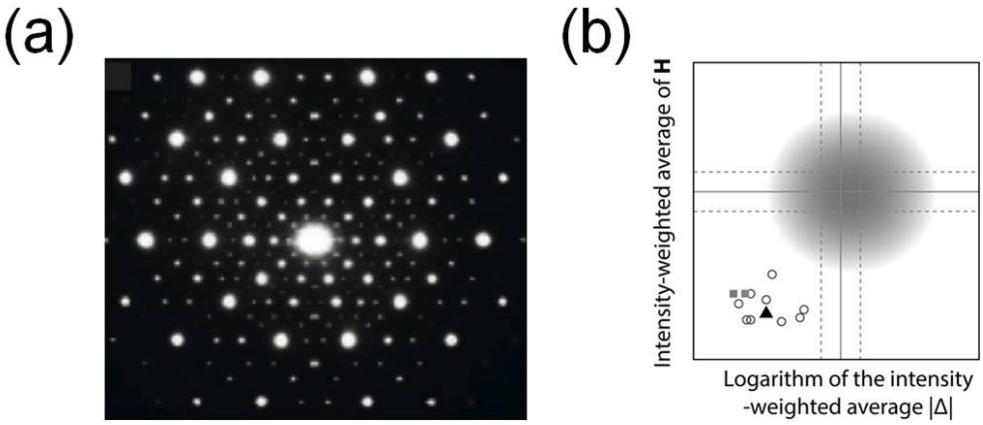

Figure 62

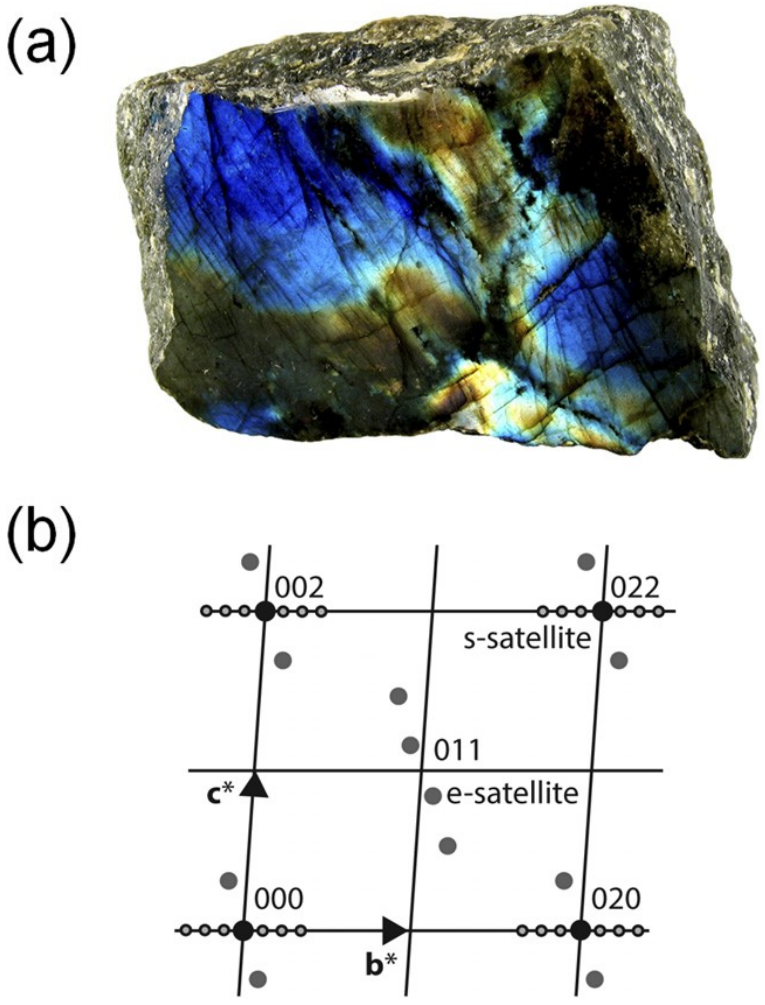

Figure 63